UNIVERSITY OF NAPLES “FEDERICO II”

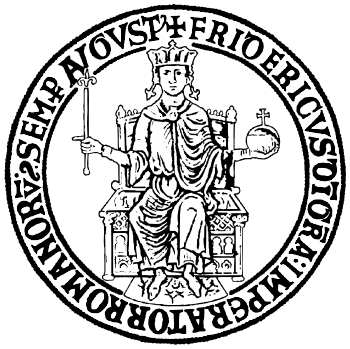

FACULTY OF ENGINEERING

AEROSPACE ENGINEERING DEPARTMENT

MASTER DEGREE THESIS IN

AEROSPACE AND ASTRONAUTIC ENGINEERING

(CLASS OF THE MASTER DEGREES IN INDUSTRIAL ENGINEERING N.25/S)

INVISCID WAKE INTERACTION WITH BODIES: A THEORETICAL INVESTIGATION

Supervisors:

Prof. Carlo de NICOLA

Ph. D. Eng. Paolo CACCAVALE

Candidate:

Pasquale DE CRESCENZO

335/175

ACADEMIC YEAR 2009-2010

a coloro che mi hanno aiutato

Contents

List of Figures

List of Tables

Symbols and Acronyms

The symbols and acronyms listed below are sorted in order of appearance through the main part of this work.

$RANS$	Reynolds Averaged Navier-Stokes
CFD	Computational Fluid Dynamics
BEM	Boundary Elements Methods
$PaMS$	Panel Method Solver
$2D$	Bidimensional
$3D$	Tridimensional
$DIAS$	Dipartimento di Ingegneria Aerospaziale (tr. Department of Aerospace Engineering)
BC	Boundary conditions
$Oxyz$	Cartesian reference frame, centered in O, called *Global Reference Frame System.*
$Gxyz$	Cartesian reference frame, centered in G, called *Local Reference Frame System.*
$\underline{i}$	Unit vector belonging to a mutually perpendicular triad aligned to the x axis.
$\underline{j}$	Unit vector belonging to a mutually perpendicular triad aligned to the y axis.
$\underline{k}$	Unit vector belonging to a mutually perpendicular triad aligned to the z axis.
$\underline{r}(x, y, z, t)$	Particle position vector in function of time,

	any subscript denotes a named point.
$\underline{U}(x, y, z, t)$	Velocity vector
$u(t)$	The scalar component of $\underline{U}$, at a given time, along the x direction, respectively.
$v(t)$	The scalar component of $\underline{U}$, at a given time, along the y direction, respectively.
$w(t)$	The scalar component of $\underline{U}$, at a given time, along the z direction, respectively.
NS	Navier-Stokes Equation Set
Re	Reynolds number
BL	Boundary Layer
ρ	Density
M	Mach number
$\underline{\omega}$	Vorticity vector
$\underline{A}$	An arbitrary vector function
Γ	Circulation of a vector field
ϕ	Scalar potential function
$\underline{\Psi}$	Vector potential or stream function
$\underline{r'}$	Relative position vector between the evaluation point and any point swept by the volume integral into the Green's function.
t	Time
$\frac{\partial}{\partial t}$	Eulerian time derivative
p	Pressure
ν	Cinematic viscosity coefficient
$\frac{D}{Dt}$	Lagrangian time derivative
$\underline{\delta\ell}$	Material line element
$\underline{U}_\phi$	Velocity component bound to the scalar potential function
$\underline{U}_\Psi$	Velocity component bound to the stream function
$\underline{U}_{\Psi_{1,2}}$	Velocity induced by a constant strength vortex line segment which begins at point 1 and ends at point 2
∞	Subscript ∞ denotes conditions at infinity

$\underline{n}$	Unit vector normal to a surface
TE	Trailing edge
$\Delta p_{T.E.}$	Pressure jump at the trailing edge
$\gamma_{T.E.}$	Vorticity component parallel to the trailing edge
ϕ_{upper}	Potential at the point on the upper surface of the trailing edge of the wing
ϕ_{lower}	Potential at the point on the lower surface of the trailing edge of the wing
$\Gamma_{span,wing}$	Bound vorticity on the wing oriented in the direction parallel to the trailing edge
$\Gamma_{span,wake}$	Bound vorticity on the wake oriented in the direction parallel to the trailing edge
φ	Doublet wake sheet equivalent to the vortex wake sheet $\underline{\Psi}$
$\underline{F}(t)$	Total force acting over a surface
$\underline{M}(t)$	Total moment of force acting over a surface
L	Lift component
D	Drag component
D_f	Friction drag component
D_p	Form drag component
D_i	Induced drag component
q_∞	Dynamic pressure of the asymptotic velocity
C_p	Pressure coefficient
C_l	Lift coefficient
C_{di}	Lift-induced drag coefficient
c	Reference chord
σ	Source strength
μ	Doublet strength
$\underline{U_r}$	The velocity of the relative motion between a mobile surface of the body and its frame center
$\underline{\Omega}$	The angular velocity around the body frame center
$\underline{\alpha_p}$	Vortex element

α_{x_p}	Scalar component of $\underline{\alpha}_p$ along the x direction
α_{y_p}	Scalar component of $\underline{\alpha}_p$ along the y direction
η	Core radius associated with the vorton
r_η	Ratio between the absolute distance of the evaluation point from the vorton and the core radius
FWE	Forward or also Explicit Euler integration scheme
$RK2$	Predictor-corrector, or also 2^{nd} order Runge-Kutta integration scheme
ΔS	Panel area
Δt	Discrete time step
ϵ_L	Local numerical error.
R_{max}	The radius of a circular plane of marked particles
x_{t0}	The initial separation between the center of the moving object and the plane of marked particles
y_{t0}	The starting y coordinate of a particle belonging to the marked plane of particles
X	The displacement coordinate in the x direction
Y	The displacement coordinate in the y direction
R	The radius of the circle
y_{fin}	Final y coordinate of the particle
D_P	Partial drift volume
D_V	Lagrangian drift volume
t_{el}	Elapsed time
t_{cpu}	Calculation time
AR	Aspect Ratio
$\beta(t)$	The instantaneous angle measured clockwise from the mean chord, referring to the pitch-heaving airfoil motion
β_a	Amplitude of pitching oscillation
ω_{PH}	Pitching and heaving movement frequency, related to the reduced frequency k
ϕ_{PH}	Phase angle ahead of the pitch-heaving motion

$h(t)$	The instantaneous vertical shift from the mean position, referring to the pitch-heaving airfoil motion
h_a	Amplitude of heaving oscillation
k	Reduced frequency
$NASA$	National Aeronautics and Space Administration
d	Propeller Diameter
r/R	Ratio between the radial distance from the propeller hub and the propeller radius
τ	Ratio between the thickness and the chord length, referring to the propeller radius
c/d	Ratio between the airfoil chord length and the propeller diameter
β	Propeller airfoil pitch angle
$C_{L,design}$	Design lift coefficient
AoA	Angle of attack
C_T	Thrust coefficient
T	Propeller or Rotor Thrust
n	Propeller Revolutions per Second
J	Propeller Advance Ratio
C_P^*	Sonic Pressure Coefficient
θ	Angular coordinate in a polar reference frame
r	Radial coordinate in a polar reference frame
$PMARC$	Panel Method Ames Research Center

Introduction

There are many interesting cases of wake interaction with bodies, an example is the interaction between a propfan and a wing section. Another common case in aeronautics is the mutual influence between the wings and the tail plane of an airplane, or the interaction between a rotor and a helicopter mainframe. Another interesting case is the following: the autoinduction existing between a single rotating blade and its wake. Moreover, quoting a non aeronautical example, there is a mutual influence between a skyscrapers group built in close proximity and their wakes. There are many other interesting cases but they are not quoted for the sake of brevity.

The state of the art into this research field uses the RANS (Reynolds Averaged Navier-Stokes) CFD (Computational Fluid Dynamic) model as analysis tool. Even if it is possible to simulate a wake-body interaction with this model it still requires a large amount of computational time and a correspondingly large economical effort.

The bibliography shows a great difficulty in predicting these unsteady flows, thus the common aeronautical practice, in presence of propellers and rotors and in absence of viscous flow separation effects, suggests to model rotating parts with actuator disks, coupled with an inviscid flow field solution, a BEM (Boundary Element Method or panel method) in a subsonic flow field, otherwise there is Euler's equation set. Another common practice is

the use of the blade element theory, instead of actuator disks, however the main drawback into this approach, compared to actuator disks, is the more difficult interfacing with the inviscid flow field used. Often are also produced experimental data useful for specific configurations. But it must be pointed out that the main costs in running experimental setups with mobile parts, which must be engine-driven, are the engine itself and the mobile parts.

Summarizing the main drawbacks into these approaches are the computational and the economical costs. These drawbacks and the lack of information about these phenomena are the main reason to study them, and it can be shown that they are overcame by vorton methods. Vorton methods use the same assumptions of panel methods, but the velocity field is solved with a Laplace and a Poisson equation. This is done in order to use the Helmholtz velocity decomposition and then to model the wake vorticity as vortex particles, the vortons. Introducing a vorton wake means to simulate the wake evolution as particle paths. The numerical error sources within particle path calculation can bring particles to penetrate bodies supposed impermeable. When it is considered an inviscid flow, the strength and shape of the wake is influenced by the mutual interaction with bodies: in order to correctly estimate the acting forces the penetration must be avoided.

The problem is solved creating a Matlab guide code, a 2D panel method which computes passive particles paths interacting with a moving, non-lifting, impermeable cylinder in order to find the numerical error sources in the particle paths. It has been found that the main error sources are the time step size and the time integration scheme, however directly reducing these error sources increases the computational time, which is an undesirable feature during a pre-design phase. It is more effective to apply a simple countermeasure against the few penetrating particles, without touching elements like the

time-step or the time integration scheme. Once found a countermeasure it is applied to the main program used into this thesis, the PaMS (Panel Method Solver) code, an open source unsteady panel method solver with a vorton wake formulation.

The change applied in PaMS is a replacement which works when a particle enters inside, validated by the test cases. The first test case is about a pitch-heaving airfoil interacting with a fixed airfoil. This test case shows that PaMS is able to catch the frequency of the normal forces acting over these airfoils, which is the same on both and coincides with the motion frequency. The test has been executed using symmetrical airfoils and a far upstream wind with null angle of attack in order to emphasize that the normal force arising over the downstream airfoil is due to the interaction with the wake coming from the upstream airfoil. PaMS has also been used to simulate a transonic propfan interacting with a wing section mounting a supercritical airfoil, whose results have been compared with bibliographical experimental data. In this case the result is the good fitting between the numerical and experimental data and that this happens even in the case of transonic flow, until there are no shock waves over the wing. Another important result is that if the propfan wake is removed the numerical simulation is no more able to model the downwash and the upwash effect over the wing sections behind the propfan. PaMS can also interface with structural solvers allowing a predesign sizing which lightens the economical efforts in running experimental setups, like aeroacustical tests or interaction tests between the elements of an airplane, once known the wake-body interaction. Finally, the results available at DIAS (Department of Aerospace Engineering) allowed to setup an experiment at the Air Force Academy in Pozzuoli in order to validate this method.

Chapter 1

INCOMPRESSIBLE AND INVISCID FLOWS

In this chapter, the emphasis is on the incompressible and inviscid flows on which classical panel methods are based. In order to model the wake by means of the vorton method, the velocity field will be defined by the well-known Helmholtz decomposition. For inviscid flows, the velocity field may be described by means of the decomposition into two velocity components that have a kinematic significance: a rotational component counts for the velocity field due to the vorticity in the flow whereas a potential component is used in order to enforce the boundary conditions (from now on BC) and to ensure the compatibility of the velocity and the vorticity field in the presence of boundary. In order to consider the inviscid evolution of the vorticity field generated by the aerodynamic configurations, the mechanism of generation and shedding of the vorticity from the surface of the body into the wake is expressed in terms of the Kutta condition.

1.1 The domain

Consider the external flow field surrounding a three dimensional lifting body. The domain of interest includes all fluid external to the body surfaces (see figure 1.1). In general, the lifting configuration (e.g.: aircraft) consists of the wing, the vertical tail and the horizontal stabilizer. Each lifting part has a sharp trailing edge from which trailing vortex wakes sheds.

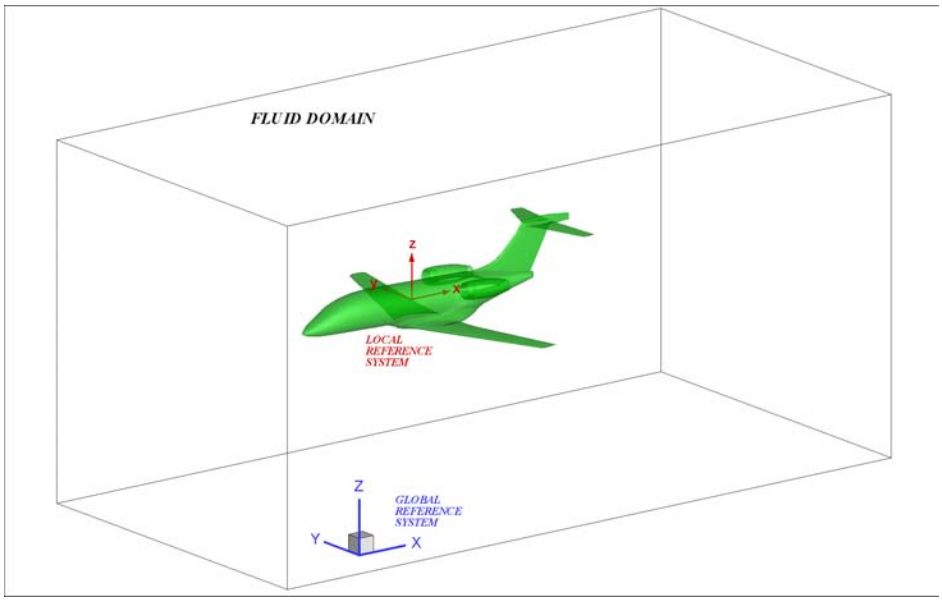

Figure 1.1: the fluid domain.

Prescribe a three-dimensional coordinate system to describe mathematically the flow of fluid through three-dimensional space. Consider the most common orthogonal coordinate system: the cartesian coordinate system. The x, y, and z are mutually perpendicular, and $\mathbf{i}$, $\mathbf{j}$, and $\mathbf{k}$ are unit vector in the x, y, and z directions, respectively. A arbitrary point P in the domain at a given time is located by the position vector $\underline{r}$, where

$$\underline{r} \;=\; \underline{r}(x,y,z,t) = x(t)\mathbf{i} \;+\; y(t)\mathbf{j} \;+\; z(t)\mathbf{k} \tag{1.1}$$

If the fluid velocity is denoted by $\underline{U}$, it can be expressed as

$$\underline{U} = \underline{U}(x, y, z, t) = u(t)\underline{i} + v(t)\underline{j} + w(t)\underline{k} \tag{1.2}$$

where $u(t)$, $v(t)$ and $w(t)$ represent the scalar component of $\underline{U}$, at a given time, along the x, y, and z directions, respectively.

The flow around the body is assumed to be inviscid and incompressible, any vorticity in the domain is localized on the thin wake regions trailing the lifting surfaces; these assumptions greatly simplify the form of the Navier-Stokes equations (from now on NS), commonly used to solve fluid-dynamic problems.

First, consider the hypothesis of inviscid flow. A flow that is assumed to involve no friction, thermal conduction, or diffusion is called inviscid flow. This kind of flow does not exist in nature but there are many practical flows where the influence of mass diffusion, viscosity, and thermal conduction is small. In these cases, it is possible to model the inviscid flows.

Theoretically, the flow is assumed to be inviscid in the limit as the Reynolds number Re goes to infinity where the Reynolds number is physically a measure of the ratio of inertia forces to viscous forces in a flow. For many practical problems, even though this high but finite parameter, the influence of the diffusive effects is limited to a very thin region adjacent to the body surface. This limited region is defined as the boundary layer (from now on BL) and the flow is essentially inviscid outside this thin region. Therefore, the considered external domain is the region outside the boundary layer. For such Re, the flow is assumed to be inviscid.

It is well-known that inviscid theory by itself cannot give satisfactory results for the prediction of the total drag.

Now, consider the hypothesis of incompressible flow. Denote the density by ρ. A flow in which the density ρ is constant is called incompressible. All

flows are compressible where a flow is called compressible where the density is variable. Really incompressible flow does not occur in nature. Similarly to the discussion of inviscid flow, there are many aerodynamic problems that can be modeled as being incompressible. Theoretically, the flow of gases is assumed to be incompressible for $M < 0.3$ where the Mach number M is the ratio of the flow velocity to the speed of sound (unless the inferior critical Mach number is lesser than 0.3) and like the Reynolds number, it is a powerful parameter in the study of gas dynamics. Practically, the flow of gases at low Mach number is essentially incompressible.

The equations of motion for a homogeneous fluid in the absence of reactions or mass diffusion are based on three physical conservation laws[1] [32]. Since the average measurable values of the flow properties are desired for aerodynamic applications, the assumption of continuous distribution of matter is imposed: this assumption is known as continuum. So the governing equations of fluid motion are derived from conservation of mass, momentum and energy equations. The resulting system of equations is known as the Navier-Stokes equations.

Since the flow is assumed to be isothermal, this leads generally to a decoupling of the energy equation from the other conservation laws. Therefore, the velocity and pressure fields are computed initially, and subsequently the energy equation may be solved for the temperature field. For flows involving temperature variations, the coupling between the temperature field and the fluid motion can occur through various effects, such as variations of viscosity or heat conductivity with temperature, influence of external forces function of temperature.

Moreover, this system of equations for incompressible flow presents a

[1]When a fluid is a composition of several chemical species with mass diffusion and/or chemical reaction, additional conservation laws may be required.

particular situation in which the unknown pressure does not appear under a time dependence form due to the non-evolutionary character of the continuity equation.

At this point, the vorticity will be briefly examined in order to introduce the role played by the vortex wake in the following chapters. This quantity is simply twice the angular velocity and is denoted by the vector $\underline{\omega}$. We know the following important result for the vorticity:

$$\underline{\omega} \;=\; \underline{\nabla} \;\times\; \underline{U} \tag{1.3}$$

In a velocity field, the curl of the velocity is equal to the vorticity. Since the curl of the velocity into the flow has a rotational discontinuity only on the thin wake region whereas it is assumed to be irrotational otherwise, $\underline{\nabla}\times\underline{U} \neq 0$ at every point in the wake and $\underline{\nabla} \times \underline{U} = 0$ at every point in the remaining domain.

An important result is the relation existing between vorticity and circulation. Assume that the surface is in a flow field and consider any point P on this surface. From Stokes'theorem[2]

$$\Gamma \;=\; -\oint_C \underline{U} \cdot \underline{ds} = -\int\int_S (\underline{\nabla} \times \underline{U}) \cdot dS \tag{1.4}$$

Therefore, the circulation about a curve C is equal to the vorticity integrated over any open surface bounded by C. Hence, if the flow is irrotational everywhere within the contour of integration and the domain included by the curve C is an open one and is included into the existence domain of the vorticity, then $\Gamma = 0$, otherwise this result is not guaranteed.

[2]Consider an open area S bounded by the closed curve C and let $\underline{A}$ be a vector field, the line integral of $\underline{A}$ over C is related to the surface integral of $\underline{A}$ over S by Stokes' theorem:

$$\oint_C \underline{A} \cdot \underline{ds} = \int\int_S (\underline{\nabla} \times \underline{A}) dS$$

The importance to make a distinction between rotational and irrotational flows lies in the fact that irrotational flows are much easier to analyze than rotational flows even though the applications of irrotational flow are limited.

Once the fluid domain has been described, see how to analyze the flow field. In the following section, it will be shown how a vector field can be expressed by means of a scalar potential component and a vector potential component by the Helmholtz decomposition.

1.2 The Helmholtz theorem

In a hydrodynamic context, Helmholtz showed in 1858 that any vector field that vanishes at infinity and has other requirements about its smoothness and its existence domain can be decomposed into two parts: one is an irrotational component which can be expressed by the gradient of a scalar function and the other is a rotational part which can be expressed by the curl of the vector function. This is the Helmholtz theorem which has very important applications in many physical problems, like the simulation of incompressible fluids, or in electromagnetism (Maxwell's equations).

As shown by Gui and Dou [29], the Helmholtz theorem states that if $\underline{A}$ is an arbitrary continuous vector function with all the second order partial derivatives in free space, and its surface integration or its any partial derivative is zero at infinity, then this vector function can be defined as the sum of the gradient of a scalar function and the curl of a vector function, that is

$$\underline{A} \;=\; \underline{\nabla}\phi \;+\; \underline{\nabla} \;\times\; \underline{\Psi} \tag{1.5}$$

with

$$\phi(\underline{r}) \;=\; \int_V \frac{\underline{\nabla} \cdot \underline{A}(\underline{r})}{4\pi|\underline{r}'|} dV \tag{1.6}$$

$$\underline{\Psi}(\underline{r}) \quad = \int_V \frac{\underline{\nabla} \times \underline{A}(\underline{r})}{4\pi|\underline{r'}|} dV \tag{1.7}$$

where $1/(4\pi|\underline{r'}|)$ is the Green's function. Equations (1.6) and (1.7) can be derived by means of the Green's Identities, $\underline{\Psi}$ is the vector potential or stream function and $\underline{\phi}$ is the scalar potential.

Note that the functions into the volume integral must be evaluated at the position $\underline{r}$, referring from from the origin, then $\underline{r}$ coincides with the evaluation point of ϕ (or $\underline{\Psi}$), while $\underline{r'}$ is the relative position between the evaluation point and any point swept by the volume integral.

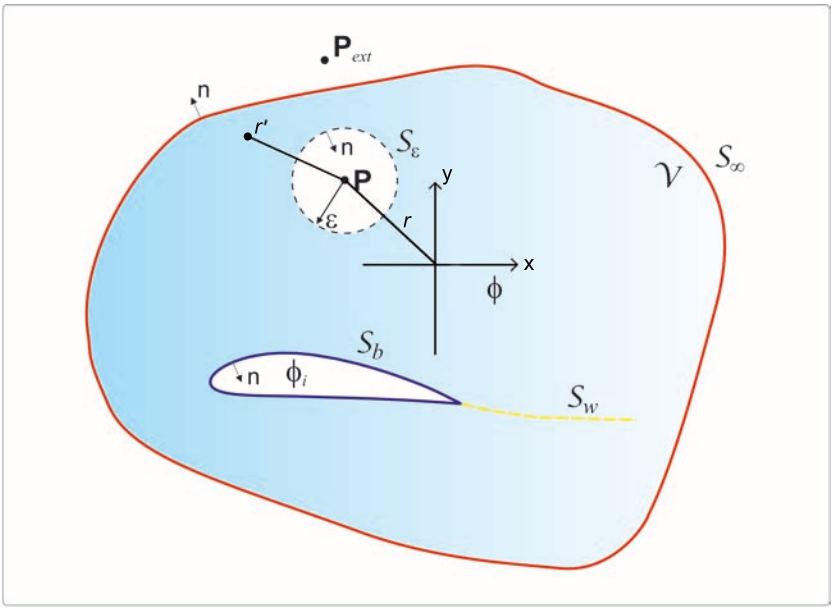

Figure 1.2: The fluid domain considered in the derivation of the Green's Theorem.

Observe that, for the vector function $\underline{A}$, the following vector identities result to be valid

$$\underline{\nabla} \cdot (\underline{\nabla}\phi + \underline{\nabla} \times \underline{\Psi}) \quad \rightarrow \quad \nabla^2\phi = \underline{\nabla} \cdot \underline{A} \tag{1.8}$$

$$\underline{\nabla} \times (\underline{\nabla}\phi + \underline{\nabla} \times \underline{\Psi}) \quad \rightarrow \quad \underline{\nabla}(\underline{\nabla} \cdot \underline{\Psi}) - \nabla^2\underline{\Psi} = \underline{\nabla} \times \underline{A} \tag{1.9}$$

where, the following analytical properties hold:

$$\underline{\nabla} \cdot (\underline{\nabla} \times \underline{\Psi}) = 0 \tag{1.10}$$

$$\underline{\nabla} \times (\underline{\nabla}\phi) = \underline{0} \tag{1.11}$$

Note that, for the Helmholtz decomposition, the choice of $\underline{\Psi}$ can be arbitrary, therefore $\underline{\Psi}$ may be solenoidal or not divergence-free. Instead, as it is shown in further on, the characteristics of the vector $\underline{A}$ depends on another considerations.

Now, if the vector potential $\underline{\Psi}$ and the vector function $\underline{A}$ are solenoidal, equations (1.8) and (1.9) become

$$\nabla^2\phi = 0 \tag{1.12}$$

$$-\nabla^2\underline{\Psi} = \underline{\nabla} \times \underline{A} \tag{1.13}$$

Equations (1.12) and (1.13) are Laplace's equation and Poisson's equation, respectively. Therefore, the problem can be worked out by solving one Laplace's equation for the irrotational component and one Poisson's equation for the solenoidal component. Equations (1.6) and (1.7) are the solutions of Laplace's equation and Poisson's equation, respectively.

1.3 The mass conservation and the vorticity evolution equations

Consider the conservation equation:

$$\frac{\partial\rho}{\partial t} + \underline{\nabla} \cdot (\rho\underline{U}) = 0 \tag{1.14}$$

For incompressible flow, $\rho(x, y, z, t)$ is constant. Therefore,

$$\partial\rho/\partial t = 0 \tag{1.15}$$

and

$$\underline{\nabla} \cdot (\rho \underline{U}) \;=\; \rho \, \underline{\nabla} \cdot \underline{U} \tag{1.16}$$

Then, the governing continuity equation for a fluid with a constant density is expressed in differential form as:

$$\underline{\nabla} \cdot \underline{U} \;=\; 0, \tag{1.17}$$

where $\underline{\nabla} \cdot \underline{U}$ is physically the time rate of change of the volume of a moving fluid element per unit volume.

The vorticity evolution equation is derived from the momentum balance equation of the NS,

$$\frac{\partial \underline{U}}{\partial t} + \underline{U} \cdot \underline{\nabla}\, \underline{U} \;= -\frac{\nabla p}{\rho} \;+\; \nu \nabla^2 \underline{U} \tag{1.18}$$

where ρ is the fluid density, p is the pressure and ν is the cinematic viscosity. Taking the curl of above equation, the resulting equation for the vorticity evolution in the domain is

$$\underline{\nabla} \times \frac{\partial \underline{U}}{\partial t} + \underline{\nabla} \times (\underline{U} \cdot \underline{\nabla}\, \underline{U}) \;= -\underline{\nabla} \times \left(\frac{\nabla p}{\rho} \right) \;+\; \underline{\nabla} \times (\nu \nabla^2 \underline{U}) \tag{1.19}$$

For fixed reference frames, the first term on the left side becomes

$$\underline{\nabla} \times \frac{\partial \underline{U}}{\partial t} = \frac{\partial (\underline{\nabla} \times \underline{U})}{\partial t} = \frac{\partial \underline{\omega}}{\partial t} \tag{1.20}$$

Similarly, the last term on the right side becomes

$$\underline{\nabla} \times (\nu \nabla^2 \underline{U}) = \nu \nabla^2 \underline{\omega} \tag{1.21}$$

Now, since there exists the identity $\underline{\nabla} \times \underline{\nabla} \cdot = 0$, the pressure term vanishes, provided that the density is uniform

$$\underline{\nabla} \times \left(\frac{\nabla p}{\rho} \right) = \underline{0} \tag{1.22}$$

The inertial term $\underline{U} \cdot \underline{U}$ can be rewritten as

$$\underline{\nabla} \times (\underline{U} \cdot \underline{\nabla}\ \underline{U}) \ = \underline{\nabla} \left(\frac{U^2}{2} \right) - \underline{U} \times \underline{\omega} \tag{1.23}$$

and then the term $\underline{\nabla} \times (\underline{U} \cdot \underline{\nabla}\ \underline{U})$ can be written

$$\underline{\nabla} \times (\underline{U} \cdot \underline{\nabla}\ \underline{U}) = \underline{\nabla} \times \underline{\nabla} \left(\frac{U^2}{2} \right) - \underline{\nabla} \times (\underline{U} \times \underline{\omega}) \tag{1.24}$$

$$= \underline{U} \cdot \underline{\nabla}\ \underline{\omega} - \underline{\omega} \cdot \underline{\nabla}\ \underline{U} + \underline{\omega}(\underline{\nabla} \cdot \underline{U}) + \underline{U}(\underline{\nabla} \cdot \underline{\omega}) \tag{1.25}$$

$$= \underline{U} \cdot \underline{\nabla}\ \underline{\omega} - \underline{\omega} \cdot \underline{\nabla}\ \underline{U} \tag{1.26}$$

Putting everything together, the vorticity equation results

$$\frac{\partial \underline{\omega}}{\partial t} + \underline{U} \cdot \underline{\nabla}\ \underline{\omega} \ = \ \underline{\omega} \cdot \underline{\nabla}\ \underline{U} + \nu \nabla^2 \underline{\omega} \tag{1.27}$$

where the first term $\underline{\omega} \cdot \underline{\nabla}\ \underline{U}$ on the right hand side represents the vorticity stretching (or how the strength and magnitude of the vorticity changes as it is exposed to velocity gradients in the fluid field). In chapter 2 it will be discussed that the stretching term may be neglected in certain applications.

Since the flow is assumed to be inviscid ($Re \to \infty$), then the vorticity can be rewritten as

$$\frac{\partial \underline{\omega}}{\partial t} + \underline{U} \cdot \underline{\nabla}\ \underline{\omega} \ = \ \underline{\omega} \cdot \underline{\nabla}\ \underline{U} \tag{1.28}$$

Observe that, for very high values of the Reynolds, the vorticity that is created at the body surface is convected along with the flow much faster than it can be diffused out across the flow. So the vorticity remains in the confines of the thin region that includes the boundary layer and the trailing wake. The fluid in the outer part of the fluid domain is effectively irrotational. However, since the fluid has been assumed to be ideal in this thesis, the vorticity is only confined in the wake: the boundary layer does not exist in ideal fluids.

Recall, now, that the evolution equation for a material line element $\underline{\delta\ell}$ can be written as follow:

$$\frac{D\underline{\delta\ell}}{Dt} \;=\; \underline{\delta\ell}\cdot\underline{\nabla}\,\underline{U} \tag{1.29}$$

It is clear that vortex lines move as material lines for inviscid flows.

Recalling, moreover, that a vortex tube is defined as the set of vortex lines that perforate a given surface part S and the circulation of a vortex tube is the same for all oriented surface patches that define the vortex tube due to free divergence of $\underline{\omega}$, the circulation of a vortex tube is conserved for inviscid flows. Vortex tubes move as material volumes and they conserve their circulation.

1.4 The Laplace's and Poisson's equations

Since the velocity $\underline{U}$ and the vorticity $\underline{\omega}$ must satisfy the mass conservation (1.17) and the vorticity evolution laws (1.28) it can be demonstrated that the velocity vector field can be decomposed by means of the Helmholtz theorem and that the velocity can be calculated using equations (1.12) and (1.13) instead of the (1.17) and the (1.28). Then the scalar potential component and the vector potential component of the velocity vector are now defined. Into the equation (1.30) ϕ is the scalar potential for the velocity $\underline{U}_\phi$ in the flow domain, $\underline{\Psi}$ is the vector potential or stream function for the velocity $\underline{U}_\Psi$ in the flow domain, $\underline{U}_\phi$ is the velocity component bound to the scalar potential function and $\underline{U}_\Psi$ is the velocity component bound to the stream function.

$$\underline{U}(\underline{r},t) \;=\; \underline{U}_\phi(\underline{r},t) \;+\; \underline{U}_\Psi(\underline{r},t) \;=\; \underline{\nabla}\phi \;+\; \underline{\nabla}\times\underline{\Psi} \tag{1.30}$$

$$\underline{U}_\Psi \;=\; \underline{\nabla}\times\underline{\Psi} \tag{1.31}$$

$$\underline{U}_{\phi} \;=\; \underline{\nabla}\phi \tag{1.32}$$

Observe that the the definition of $\underline{\Psi}$ is statement of the mass conservation. In fact, $\underline{U}_{\Psi}$ automatically satisfies the continuity equation, since the gradient of the curl of any vector is identically zero (see equation (1.10)). From a physical point of view, the lines of a constant $\underline{\Psi}$ represent stream lines, and the difference in the values of $\underline{\Psi}$ between two streamlines gives the volumetric flow rate between the two.

One important consequence of irrotationality is the existence of a velocity potential. Indeed, the equation $\underline{\xi} = \underline{\nabla} \times \underline{U} = \underline{0}$ is a necessary and sufficient condition for the existence of a potential ϕ such that

$$\underline{U}_{\phi} \;=\; \underline{\nabla}\phi \tag{1.33}$$

where $\phi(x, y, z, t)$ is the scalar potential for the velocity in the flow domain. This scalar potential consents the substitution of a three-component vector by a single scalar as the principle unknown in theoretical investigation.

The velocity potential is analogous to stream function in the sense that derivatives of ϕ yield the velocity but there are distinct differences between ϕ and $\underline{\Psi}$. First, the velocity is obtained by differentiating ϕ in the velocity direction, whereas $\underline{\Psi}$ in the direction normal to the velocity direction. Second, the velocity potential is defined only for irrotational flow, whereas the stream function can be defined for rotational or irrotational flows.

Substituting the velocity potential relationship into the mass conservation law (1.17), the resulting equation simplifies to:

$$\underline{\nabla} \cdot (\underline{\nabla}\phi + \underline{\nabla} \times \underline{\Psi}) \;=\; \underline{\nabla} \cdot (\underline{\nabla}\phi) = \nabla^2\phi = 0 \tag{1.34}$$

Then the Laplace's equation is indeed bound to the mass conservation. Note that Laplace's equation is a linear differential equation and solutions of

Laplace's equation are called harmonic functions: this is an elliptic differential equation that results in a boundary-value problem. Since the fluid's viscosity has been neglected, the no-slip boundary condition on a solid-fluid boundary cannot be enforced.

Remember that the vorticity field $\underline{\omega}(\underline{r}, t)$ is defined as the curl of the velocity:

$$\underline{\nabla} \times \underline{U} \;=\; \underline{\omega} \tag{1.35}$$

Then it is possible to use $\underline{\omega}$ into the (1.13), this means that the Poisson's equation relates the vector potential to the vorticity. Finally the equations to be solved are:

$$\nabla^2 \underline{\phi} \;=\; 0 \tag{1.36}$$

$$\nabla^2 \underline{\Psi} \;=\; -\underline{\omega} \tag{1.37}$$

Moreover, the fact that Laplace's equation is linear is very important, because the superposition of any solution of a linear differential equation is also a solution of Laplace's equation. This fact implies that the solution of a complicated flow pattern for an incompressible flow can be obtained as the sum of a number of elementary incompressible flow solutions.This consideration is the basis of the panel methods.

However it must be done a clarification about the wake and the linearity of the above equation. The wake surface in panel methods is part of the boundary, then it has a key role in determining the potential function. If the shape of the wake is already known there are no problems in determining linearly the velocity field. But the most common problems concern bodies of various geometries about which it is desired to know the velocity field and the wake. The Helmholtz conservation theorems about circulation establish a link between velocity field and the wake, thus to calculate the velocity it is

needed to know the wake shape and its vorticity distribution which are in turn linked to the unknown velocity. This is evidently a non linearity, but it can be by-passed. Prandtl, in the cases of wings, simply nailed down the wake to a plane, more recent algorithms take this great intuition of the aerodinamicist as starting guess within iterative procedures, thus the wake data are known and the velocity field can be calculated, although by attempts.

1.5 The velocity induced by vorticity: the Biot-Savart law

The velocity induced by a vorticity distribution (see figure 1.3) is both an example about how to solve the Poisson's equation and an elementary flow field to be used later. Consider Poisson's equation $\underline{\omega} = -\nabla^2 \underline{\Psi}$. The solution of this equation, using Green's theorem, is

$$\underline{\Psi} \;=\; \frac{1}{4\pi} \int_V \frac{\underline{\omega}}{|\underline{r}_0 - \underline{r}_1|} dV \tag{1.38}$$

where $\underline{\Psi}$ is evaluated at point P which is a distance $\underline{r}_0$ from the origin and is obtained by integration of the vorticity at point $\underline{r}_1$ within the volume V.Equation above and equation (1.7) are the same relationship. Clearly, the velocity is the curl of $\underline{\Psi}$

$$\underline{U}_\Psi \;=\; \frac{1}{4\pi} \int_V \underline{\nabla} \times \frac{\underline{\omega}}{|\underline{r}_0 - \underline{r}_1|} dV \tag{1.39}$$

Consider, then, an infinitesimal piece of the vorticity filament $\underline{\omega}$. Select the cross section area dS so that it is normal to $\underline{\omega}$ and the direction $d\underline{\ell}$ on the filament is

$$d\underline{\ell} \;=\; \frac{d\ell}{\omega}\, \underline{\omega} \tag{1.40}$$

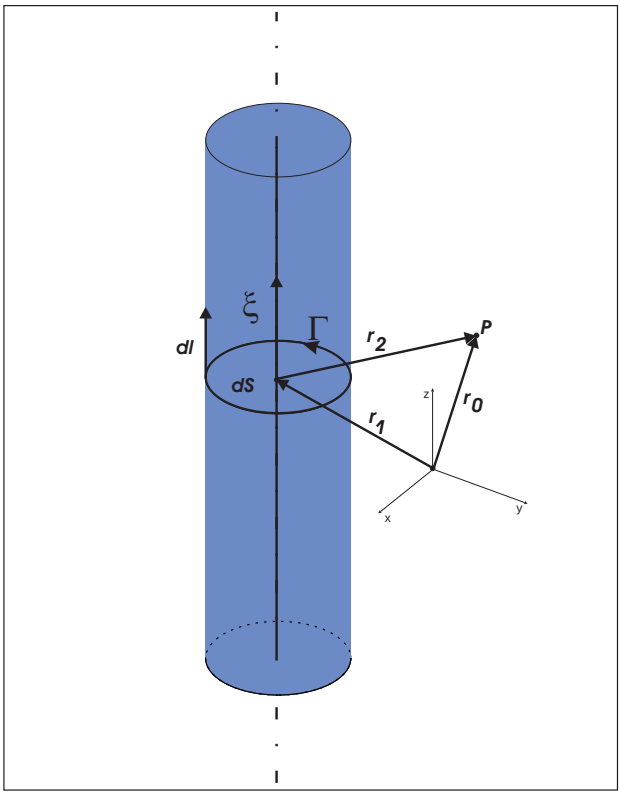

Figure 1.3: the velocity at point P induced by a vortex distribution.

Since the circulation Γ and dV are, respectively

$$\Gamma = \omega \, dS \tag{1.41}$$

$$dV = dS \, dl \tag{1.42}$$

then the integral term becomes

$$\underline{\nabla} \times \frac{\underline{\omega}}{|\underline{r}_0 - \underline{r}_1|} = \underline{\nabla} \times \Gamma \frac{d\underline{\ell}}{|\underline{r}_0 - \underline{r}_1|} = \Gamma \frac{d\underline{\ell} \times (\underline{r}_0 - \underline{r}_1)}{|\underline{r}_0 - \underline{r}_1|^3} \tag{1.43}$$

By substituting the above result in equation (1.39), resulting equation is the Biot-Savart law, which states

$$\underline{U}_\Psi = \frac{1}{4\pi} \int_V \Gamma \frac{d\underline{\ell} \times (\underline{r}_0 - \underline{r}_1)}{|\underline{r}_0 - \underline{r}_1|^3} dV \tag{1.44}$$

or in differential form

$$d\underline{U}_\Psi = \frac{\Gamma}{4\pi} \frac{d\underline{\ell} \times (\underline{r}_0 - \underline{r}_1)}{|\underline{r}_0 - \underline{r}_1|^3} \tag{1.45}$$

In case of a volume distribution of vorticity, a similar manipulation of equation (1.39) leads to the following result

$$\underline{U}_\Psi = \frac{1}{4\pi} \int_V \frac{\underline{\omega} \times (\underline{r}_0 - \underline{r}_1)}{|\underline{r}_0 - \underline{r}_1|^3} dV \tag{1.46}$$

1.5.1 The velocity induced by a straight vortex segment

The first one to make use of a vortex filament concept in the analysis of inviscid, incompressible flow was Helmholtz, who established several basic principles known as Helmholtz theorems. First, the strength of a vortex filament is constant along its length. Second, a vortex filament cannot end

in a fluid: it must extend to the boundaries of the fluid which may be $\pm\infty$ or form a closed path.

The derivation of the velocity induced by a straight vortex segment $d\underline{\ell}$ is based on the the Biot-Savart law. As a vortex line cannot start or end in a fluid, the contribution of a segment is one of a section of a continuous vortex line. Moreover, the components of the velocity induced by this vortex segment will be only tangential components.

Let $\underline{r_1}$ and $\underline{r_2}$ be the positions of the two edges of the vortex segment. The vector connecting the edges is

$$\underline{r}_0 \;=\; \underline{r}_2 \;-\; \underline{r}_1 \tag{1.47}$$

Then, the distance d and the cosines of the angles β_1 and β_2 are

$$d \;=\; \frac{|\underline{r}_1 \;\times\; \underline{r}_2|}{|\underline{r}_0|} \tag{1.48}$$

$$\cos\beta_1 \;=\; \frac{\underline{r}_0 \;\cdot\; \underline{r}_1}{|\underline{r}_0|\;|\underline{r}_1|} \tag{1.49}$$

$$\cos\beta_2 \;=\; \frac{\underline{r}_0 \;\cdot\; \underline{r}_2}{|\underline{r}_0|\;|\underline{r}_2|} \tag{1.50}$$

The velocity $\underline{U}_{\Psi_{1,2}}$ has the direction normal to the plane defined by the point P and the vortex edges $1, 2$ and the directional vector is given by

$$\frac{\underline{r}_1 \;\times\; \underline{r}_2}{|\underline{r}_1 \;\times\; \underline{r}_2|} \tag{1.51}$$

By substituting these quantities, the induced velocity is

$$\underline{U}_{\Psi_{1,2}} \;=\; \frac{\Gamma}{4\pi}\;\frac{\underline{r}_1 \;\times\; \underline{r}_2}{|\underline{r}_1 \;\times\; \underline{r}_2|}\;\underline{r}_0 \cdot \left(\frac{\underline{r}_1}{r_1} - \frac{\underline{r}_2}{r_2}\right) \tag{1.52}$$

Constant-strength vortex line segments can be used to model the wing or the wake for lifting flows, as provided in chapters 2 and 3.

1.6 The boundary conditions

Consider the incompressible flow fields over different aerodynamic bodies. It is clear that each flow is going to be distinctly different because of the different geometry. But these different flows are all governed by the same equations: $\nabla^2\phi = 0$ and $\nabla^2\underline{\Psi} = -\underline{\omega}$. How, then, can the exact solution be found? The answer to these questions lies in the fact that, as known, in every single mathematic model, the boundary conditions must be considered like integral part of the same model. Moreover, in this unsteady flow problem, the unsteady nature of the boundary conditions must be considered for the solution uniqueness for all times. This unsteady nature can be due to changes in time of the velocity vector of the uniform flow that collides the body, or changes in time of the position and the form of the body surface, or changes in times of the form of possible flexible surfaces like the wake and the surfaces of separation between different flows. These changes in time require the time updating of the boundary conditions.

Therefore, the boundary conditions need to be specified on all solid surface and at infinity, and updated in time. Moreover, to analyze aerodynamic bodies, a wing trailing edge condition (Kutta condition) that imposes a condition of smoothness on the flow field at the trailing edge is necessary .

1.6.1 Infinity boundary conditions

Since the boundary is located far away so that the flow properties on the boundary are not influenced by the body, then it is at infinity where the disturbances due the body moving through a fluid that initially at rest decays to zero in all directions. Hence, at infinity,

$$\underline{U}(\underline{r},t) \;=\; \underline{\nabla}\phi \;+\; \underline{\nabla}\times\underline{\Psi} \;=\; \underline{U}_\infty \tag{1.53}$$

These are the boundary conditions on velocity at infinity.

1.6.2 Wall boundary conditions

Regarding the wall boundary condition, since the body has a solid surface, then the flow can not penetrate the surface. For viscid flows, the velocity is zero at the surface due to the friction between the fluid and the solid surface. However, since the flow is assumed to be inviscid, the velocity at the surface can be finite and tangent to the surface because the flow cannot penetrate the surface or not tangent to the surface for the case of a solid boundary with transpiration. For this work, it is assumed the case of solid surfaces without transpiration. Clearly, this wall tangency condition implies a zero component of velocity normal to the surface.

Let $\underline{n}$ be a unit vector normal to the surface. In terms of the vector and scalar potentials, the flow tangency conditions can be written as:

$$\underline{U} \cdot \underline{n} \; = \; (\underline{\nabla}\phi \; + \; \underline{\nabla} \times \underline{\Psi}) \; \cdot \underline{n} = \; 0 \tag{1.54}$$

Observe that only the normal velocity boundary condition is applied at the wall, because of the inviscid flow assumption. For the viscid flows, the conditions to apply to the body surface are two: one is the normal velocity boundary condition, other is the tangent velocity condition.

1.7 The wing trailing edge Kutta condition

The net force produced by surfaces with sharp geometric cusps when the body moves relative to a fluid, is due to the pressure distribution over the body surface. Flows from moving around these cusps are impeded by the fact that these requires infinite pressure stresses and therefore the flows tend to leave smoothly the sharp corner and shed a trailing shear wake. Since the flow is assumed to be inviscid and irrotational, a Kutta condition must be applied to all wing trailing edges for the physicalness of the solution. In fact, the Kutta condition states that the flow leaves the sharp trailing edge of an airfoil smoothly and the velocity there is finite.

In the case of aerodynamic bodies, the capacity to manage the following Kutta wake, if necessary, its fluctuations cover an important role, so the wing trailing edge Kutta condition must be applied in time.

Moreover, since the trailing edge angle is finite, the normal component of the velocity, from both sides of the airfoil, must vanish. For a continuous velocity, this is possible if the pressure difference is zero:

$$\Delta p_{_{T.E.}} = 0 \tag{1.55}$$

this is the Kutta condition which requires that there is no pressure jump across the trailing edge.

Additionally, this can be obtained by requiring that the flow above the wing be vorticity free. The Kutta condition along the trailing edge, so that the vorticity component parallel to the trailing edge ($\gamma_{_{T.E.}}$) is zero, results:

$$\gamma_{_{T.E.}} = 0 \tag{1.56}$$

In order to prescribe the streamwise vorticity release at the trailing edge, a linearized version of the pressure continuity at the trailing edge is used

$$\phi_{upper} - \phi_{lower} = \Delta\phi_{wake} \tag{1.57}$$

Here, the subscripts *upper* and *lower* refer to points on the upper and lower surfaces of the trailing edge of the wing. The flow field without and with the imposition of the Kutta condition is presented in figure 1.4.

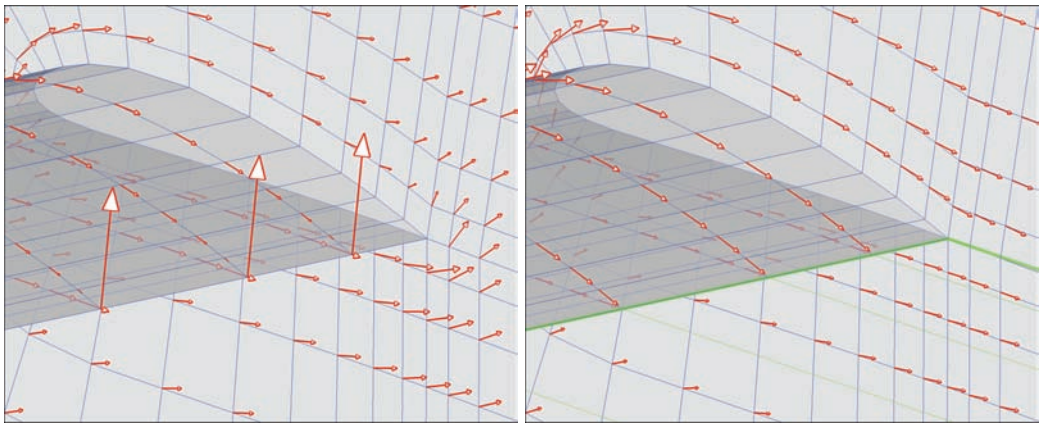

Figure 1.4: the flow field at the wing trailing edge without (left) and with (right) the imposition of the Kutta condition.

For unsteady flows, a time dependent component of the Kutta condition is also enforced. This additional condition requires that any increase in bound vorticity on the wing must be balanced by an equivalent increase in vorticity in the wake. This increased vorticity is oriented in the direction parallel to the trailing edge. The formal statement of the condition is the combined change with respect to time of the wing bound circulation and the wake circulation add to zero:

$$\left[\frac{d\Gamma_{span,wing}}{dt}\right] = -\left[\frac{d\Gamma_{span,wake}}{dt}\right] \tag{1.58}$$

where Γ represents the circulation strength of the wing and wake. Hence,

the rate at which body vorticity increases must be equal and opposite to the rate of vorticity shed into the wake.

1.8 The Unsteady Bernoulli equation

The pressure field can be computed by Bernoulli equation, once the flow field is determinate. The Bernoulli equation is the most widely used equation in fluid mechanics, and assumes frictionless flow with no work or heat transfer.

Since this thesis presents a potential-vorticity approach, the applicable unsteady Bernoulli equation will be briefly derived, starting from the incompressible Euler equations:

$$\frac{\partial \underline{U}}{\partial t} + \underline{U} \cdot \underline{\nabla}\, \underline{U} = -\frac{\underline{\nabla} p}{\rho} \tag{1.59}$$

All space excluding the trailing vortex wake region has zero vorticity, therefore the resulting equation is:

$$\frac{\partial \underline{U}}{\partial t} + \frac{1}{2}\underline{\nabla}|\underline{U}|^2 = -\frac{\underline{\nabla} p}{\rho} \tag{1.60}$$

By using the Helmholtz decomposition, the above equation becomes:

$$\frac{\partial(\underline{\nabla}\phi) + \partial(\underline{\nabla} \times \underline{\Psi})}{\partial t} + \frac{1}{2}\underline{\nabla}|\underline{\nabla}\phi + \underline{\nabla} \times \underline{\Psi}|^2 = -\frac{\underline{\nabla} p}{\rho} \tag{1.61}$$

Collecting similar terms, and re-arranging, the above equation results

$$\frac{\partial(\underline{\nabla}\phi)}{\partial t} + \frac{\partial(\underline{\nabla} \times \underline{\Psi})}{\partial t} + \frac{1}{2}\underline{\nabla}\left|\underline{\nabla}\phi + \underline{\nabla} \times \underline{\Psi}\right|^2 + \frac{\underline{\nabla} p}{\rho} = 0 \tag{1.62}$$

Now, integrating the Bernoulli equation along the streamline from surface point x_1, to a farfield reference point at ∞ where the velocity is zero since the body moves in the domain, and $p = p_\infty$ result in:

$$\int_\infty^{p_{x_1}} \frac{\partial(\underline{\nabla} \times \underline{\Psi})}{\partial t} d\underline{C} + \left(\frac{\partial \phi}{\partial t}_{x_1} + \frac{1}{2}\left|\underline{\nabla}\phi + \underline{\nabla} \times \underline{\Psi}\right|^2_{x_1}\right) = \frac{p_\infty - p_{x_1}}{\rho} \tag{1.63}$$

Therefore, the term $\frac{\partial \phi}{\partial t}$, defined in an Eulerian reference frame, can be computed by converting of a body Lagrangian reference frame:

$$\frac{\partial \phi}{\partial t} = \frac{D\phi}{Dt} - \underline{U} \cdot \underline{\nabla}\phi \tag{1.64}$$

The overall unsteady Bernoulli equation, used to determine the forces and pressures on the body, results:

$$\int_{\infty}^{p_{x_1}} \frac{\partial(\underline{\nabla} \times \underline{\Psi})}{\partial t} d\underline{C} + \frac{D\phi}{Dt} - \underline{U} \cdot \underline{\nabla}\phi + \frac{1}{2}|\underline{\nabla}\phi + \underline{\nabla} \times \underline{\Psi}|_{x_1}^2 = \frac{p_\infty - p_{x_1}}{\rho} \tag{1.65}$$

The importance of the unsteady term due to domain vorticity in the computation of the pressure will be discussed below. Now, note that this unsteady term is difficult to handle in the form:

$$\int_{\infty}^{p_{x_1}} \frac{\partial(\underline{\nabla} \times \underline{\Psi})}{\partial t} \cdot d\underline{C} \tag{1.66}$$

So, by considering the contribution of the vortex wake as an analogous contribution due to a doublet sheet, one can obtain:

$$\int_{\infty}^{p_{x_1}} \frac{\partial(\underline{\nabla} \times \underline{\Psi})}{\partial t} \cdot d\underline{C} = \int_{\infty}^{p_{x_1}} \frac{\partial(\underline{\nabla}\varphi)}{\partial t}|_{wake} \cdot d\underline{C} \tag{1.67}$$

Integrating the expression for the wake potential φ is no more difficult to handle:

$$\int_{\infty}^{p_{x_1}} \frac{\partial \varphi}{\partial t}|_{wake} \cdot d\underline{C} = \frac{\partial \varphi}{\partial t} = \frac{D\varphi}{Dt} - \underline{U} \cdot \underline{\nabla}\varphi \tag{1.68}$$

where, $\nabla\varphi$ is the velocity due to the wake. Therefore, the overall unsteady Bernoulli equation is:

$$\frac{D\varphi}{Dt} + \frac{D\phi}{Dt} - \underline{U} \cdot \underline{\nabla}(\phi + \varphi) + \frac{1}{2}\,|\underline{\nabla}\phi + \underline{\nabla}\varphi|_{x_1}^2 = \frac{p_\infty - p_{x_1}}{\rho} \tag{1.69}$$

1.9 Computation of forces and moments

Once the pressure field has been determined by Bernoulli equation, the aerodynamic forces and moments on the lifting body can be computed. These quantities can seem complex but, in all cases, they are due to only two basic sources over the body surface:

- pressure distribution;
- shear stress distribution.

It's well-known that the only way nature has to communicate an aerodynamic force to a solid body moving through a fluid, is through the pressure and shear stress distributions which exist on the surface. Pressure and shear stress have the same dimension (force per unit area) and they vary along the surface. The first source acts normally to the body surface. The second source acts tangentially and it is due to the frictional effect of the flow "rubbing" against the surface as it moves around the body. The shear stress τ_w is defined as the force per unit area acting tangentially on the body surface due to friction.

The net effect of the pressure and shear stress distributions integrated over the complete body surface is a resultant aerodynamic force $\underline{F}$ and moment $\underline{M}$ on the body. Therefore, from the unsteady Bernoulli equation, the resultant force and moment can be computed as below:

$$\underline{F}(t) = \int_{S(t)} (p_\infty - p_{x_1}(t))\underline{n}\, dS(t) \tag{1.70}$$

$$\underline{M}(t) = \int_{S(t)} \underline{r} \times [(p_\infty - p_{x_1}(t))\ \underline{n}]\ dS(t) \tag{1.71}$$

where $\underline{r}$ must be specified where starts from since moment of force varies with the reference point of the reference frame. In aeronautical practice the most common choice is the aerodynamic focus, but it is not the only choice.

The resultant force can be split in two component: lift $\underline{L}$ and drag $\underline{D}$. The first is defined as the component of $\underline{F}$ perpendicular to the relative wind. The second is defined as the component of $\underline{F}$ parallel to the relative wind.

Consider, now, viscous effects on drag. The presence of friction in a flow produces two sources of drag:

- skin friction drag D_f due to the shear stress at the wall;
- pressure drag due to flow separation D_p, called form drag.

Since the viscosity has been neglected in this work, the total drag cannot be satisfactory determined. In fact, it is possible to compute only the pressure force with inviscid theory. However, there exists a source of drag induced by lift D_i that can be computed in inviscid theory too.

1.9.1 Pressure, force and moment coefficients

In fluid dynamics, it is common to use the pressure coefficient rather than pressure. The pressure coefficient C_p is a dimensionless pressure and its usefulness is known in aerodynamics, from subsonic to hypersonic flow. The pressure coefficient is defined as

$$C_p = \frac{p - p_\infty}{q_\infty} = \frac{p - p_\infty}{\frac{1}{2}\rho_\infty U_\infty^2} \tag{1.72}$$

The pressure coefficient is an important quantity because the distribution of C_p over the body surface leads directly to the value of the lift coefficient C_L (that will be defined later) and the calculation of the effect of Mach number M_∞ on C_L by the Prandtl-Glauert rule.

Similarly, the dimensional lift, drag, and moment coefficients can be de-

fined from dimensional analysis, as

$$C_L = \frac{L}{q_\infty S} \tag{1.73}$$

$$C_D = \frac{D}{q_\infty S} \tag{1.74}$$

$$C_M = \frac{M}{q_\infty S c} \tag{1.75}$$

where S and c are the lifting body area and chord of reference, respectively.

Chapter 2

PANEL METHODS

In the previous chapter, the fundamental fluid dynamic equations and the conditions leading to the simplified ideal flow problem were formulated and discussed. Now, the emphasis is placed on the theory and the numerical procedure used to solve regions of the flow field assumed to be inviscid, incompressible and also irrotational. Therefore, the elementary solutions of Laplace equation and the basic methodology for obtaining the solutions of the more complex potential flow problems will be described in this chapter.

2.1 Basic solutions of Laplace equation

Laplace equation over bodies may be solved by the distribution of elementary solutions whose strengths are obtained by enforcing the impermeability flow or a fixed normal flow condition on the solid boundaries. But, when the complexity of the method increases, the calculation becomes more complicate. Therefore, some typical numerical elements upon which some numerical solutions are based, will be presented in this section. Particularly, attention is addressed to some three-dimensional constant-strength singularity elements

[14][34][25].

In the general case, the potential may be integrated over a curve, surface or volume, in order to generate the corresponding singularity elements. In these cases, it must not be addressed to strength (like in the case of point elements), but strength density per unit of length, area or volume, respectively.

Particularly, it is possible to imagine elementary solutions of Laplace equation that are distributed over plane geometric elements oriented in space: these elements may be quadrilateral or triangular. Therefore, let σ be the strength per unit of area for the distributed source, and analogously let μ for the distributed doublet. The validity of the equations which will be derived will be related to the plane quadrilaterals, but these may be applied also to triangular elements which are plane by definition.

Before to describe the three-dimensional constant-strength singularity elements, the free stream solution of Laplace equation will be briefly discussed.

The most simple solution of Laplace equation regards a uniform free stream. In fact, equation (1.34) is certainly fulfilled by the follow potential

$$\phi(x, y, z) = u_\infty x + v_\infty y + w_\infty z \tag{2.1}$$

which represents a uniform flow field

$$\underline{U} = \left(\frac{\partial\phi}{\partial x}, \frac{\partial\phi}{\partial y}, \frac{\partial\phi}{\partial z}\right) = (u_\infty, v_\infty, w_\infty) \tag{2.2}$$

2.1.1 Quadrilateral source

Begin to consider a surface element bounded by four straight lines, with a constant-strength source distribution σ (see figure 2.1). Consider a reference frame with origin in the quadrilateral center and with z axis directed along

the normal to the quadrilateral. Thus, the potential in any point P is given by:

$$\phi(x,y,z) = -\frac{\sigma}{4\pi}\int\int_S \frac{dS}{\sqrt{(x-x_0)^2+(y-y_0)^2+z^2}} \tag{2.3}$$

Equation (2.3) may be rewritten by means of the Hess and Smith [31] pro-

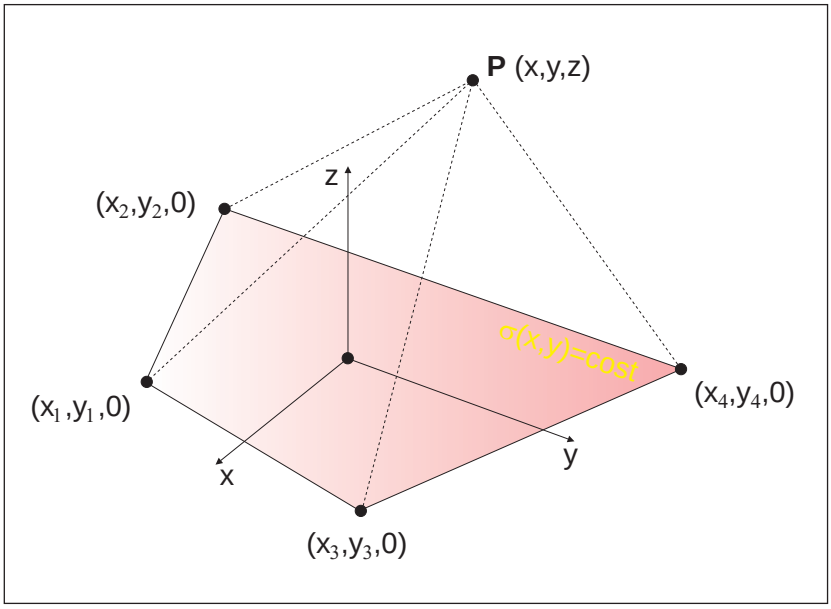

Figure 2.1: quadrilateral constant-strength source element.

cedure in function of the coordinates of the four quadrilateral vertexes:

$$\phi(x,y,z) = -\frac{\sigma}{4\pi}\sum_{(ij)=(1,2,3,42,3,4,1)} \frac{\widehat{x}_i\,\widehat{y}_{ij}-\widehat{y}_i\,\widehat{x}_{ij}}{d_{ij}} \ln\frac{r_i+r_j+d_{ij}}{r_i+r_j-d_{ij}} +$$
$$-|z|\frac{\sigma}{4\pi}\sum_{(ij)=(1,2,3,42,3,4,1)}\left[\tan^{-1}\left(\frac{m_{ij}e_i-h_i}{zr_i}\right)-\tan^{-1}\left(\frac{m_{ij}e_j-h_j}{zr_j}\right)\right] \tag{2.4}$$

from which the velocity components derives:

$$u(x,y,z) = \frac{\sigma}{4\pi}\sum_{(ij)=(1,2,3,42,3,4,1)} \frac{\widehat{y}_{ij}}{d_{ij}} \ln\frac{r_i+r_j-d_{ij}}{r_i+r_j+d_{ij}} \tag{2.5}$$

$$v(x,y,z) = \frac{\sigma}{4\pi}\sum_{(ij)=(1,2,3,42,3,4,1)} \frac{-\widehat{x}_{ij}}{d_{ij}} \ln\frac{r_i+r_j-d_{ij}}{r_i+r_j+d_{ij}} \tag{2.6}$$

$$w(x,y,z) = \frac{\sigma}{4\pi}\sum_{(ij)=(1,2,3,42,3,4,1)} \tan^{-1}\left(\frac{m_{ij}e_i-h_i}{zr_i}\right) +$$
$$- \frac{\sigma}{4\pi}\sum_{(ij)=(1,2,3,42,3,4,1)} \tan^{-1}\left(\frac{m_{ij}e_j-h_j}{zr_j}\right) \tag{2.7}$$

where

$$\begin{aligned}
\widehat{x}_i &= x - x_i & i &= 1,2,3,4 \\
\widehat{y}_i &= y - y_i & i &= 1,2,3,4 \\
\widehat{x}_j &= x - x_j & j &= 2,3,4,1 \\
\widehat{y}_j &= y - y_j & j &= 2,3,4,1 \\
\widehat{x}_{ij} &= x_j - x_i & (ij) &= (1,2,3,42,3,4,1) \\
\widehat{y}_{ij} &= y_j - y_i & (ij) &= (1,2,3,42,3,4,1) \\
d_{ij} &= \sqrt{(x_j - x_i)^2 - (y_j - y_i)^2} & (ij) &= (1,2,3,42,3,4,1) \\
m_{ij} &= (y_j - y_i)/(x_j - x_i) & (ij) &= (1,2,3,42,3,4,1) \\
r_i &= \sqrt{(x - x_i)^2 + (y - y_i)^2 + z^2} & i &= 1,2,3,4 \\
e_i &= (x - x_i)^2 + z^2 & i &= 1,2,3,4 \\
h_i &= (x - x_i)(y - y_i) & i &= 1,2,3,4
\end{aligned} \tag{2.8}$$

Equations (2.5) and (2.6) show how the velocity components u and v are defined everywhere except on the quadrilateral boundary. For the component w, equation (2.7) shows that two limit cases exist when $z = 0$: one discontinuity when the point P lies on the quadrilateral

$$w(z = \pm 0) = \frac{\pm\sigma}{2} \tag{2.9}$$

and a null value when P is outside of the quadrilateral

$$w(z = \pm 0) = 0 \tag{2.10}$$

Figure 2.2 is based on the implementation of the equations (2.3), (2.5), (2.6), (2.7) and it shows the flow field induced by a quadrilateral source.

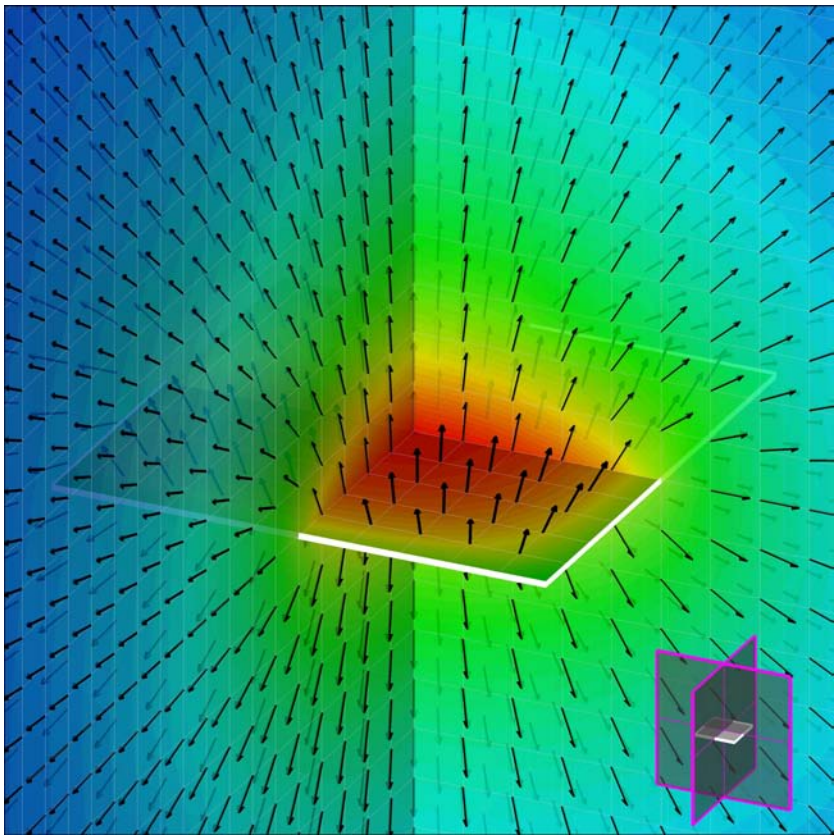

Figure 2.2: quadrilateral source - uniform velocity vector and isopotential contour.

2.1.2 Quadrilateral doublet

Consider a quadrilateral element with a constant-strength doublet distribution which points in the z direction, as showed in figure 2.3. Similar to the source element, the velocity potential may be obtained by integrating the point elements:

$$\phi(x,y,z) = -\frac{\mu}{4\pi}\int_S \frac{z\ dS}{[(x-x_0)^2+(y-y_0)^2+(z-z_0)^2]^{3/2}} \tag{2.11}$$

Following again the Hess and Smith procedure, one may obtain also this

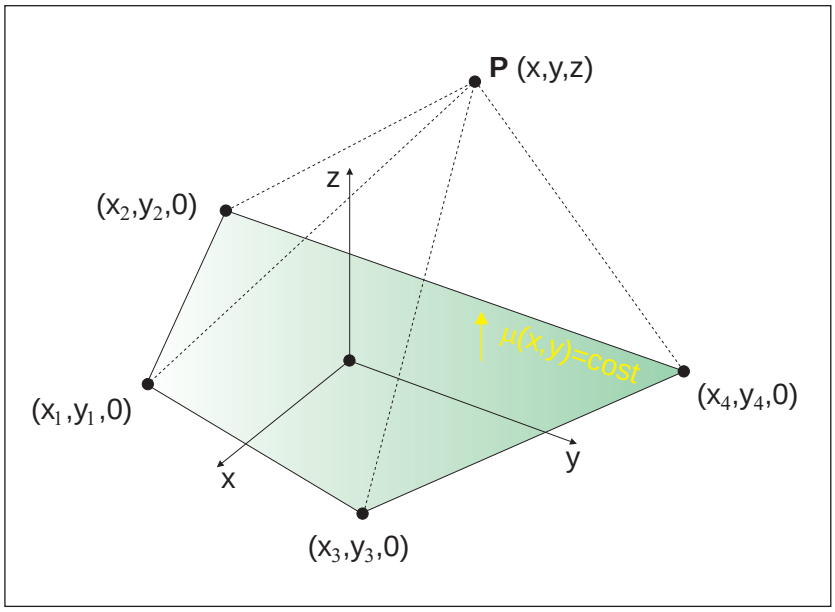

Figure 2.3: quadrilateral doublet element.

potential in function of the quadrilateral vertex coordinates:

$$\phi(x,y,z) = \frac{\mu}{4\pi} \sum_{(ij)=(1,2,3,42,3,4,1)} \tan^{-1}\left(\frac{m_{ij}e_i - h_i}{zr_i}\right) +$$

$$-\frac{\mu}{4\pi} \sum_{(ij)=(1,2,3,42,3,4,1)} \tan^{-1}\left(\frac{m_{ij}e_j - h_j}{zr_j}\right) \tag{2.12}$$

and the corresponding velocity components:

$$u(x,y,z) = \frac{\mu}{4\pi} \sum_{(ij)=(1,2,3,42,3,4,1)} \frac{-z\widehat{y}_{ij}(r_i + r_j)}{r_i r_j \{r_i r_j - [\widehat{x}_i\widehat{x}_j + \widehat{y}_i\widehat{y}_j + z^2]\}} \tag{2.13}$$

$$v(x,y,z) = \frac{\mu}{4\pi} \sum_{(ij)=(1,2,3,42,3,4,1)} \frac{z\widehat{x}_{ij}(r_i + r_j)}{r_i r_j \{r_i r_j - [\widehat{x}_i\widehat{x}_j + \widehat{y}_i\widehat{y}_j + z^2]\}} \tag{2.14}$$

$$w(x,y,z) = \frac{\mu}{4\pi} \sum_{(ij)=(1,2,3,42,3,4,1)} \frac{[\widehat{x}_j\widehat{y}_i - \widehat{x}_i\widehat{y}_j](r_i + r_j)}{r_i r_j \{r_i r_j - [\widehat{x}_i\widehat{x}_j + \widehat{y}_i\widehat{y}_j + z^2]\}} \tag{2.15}$$

Observe that the doublet potential may be developed from the source

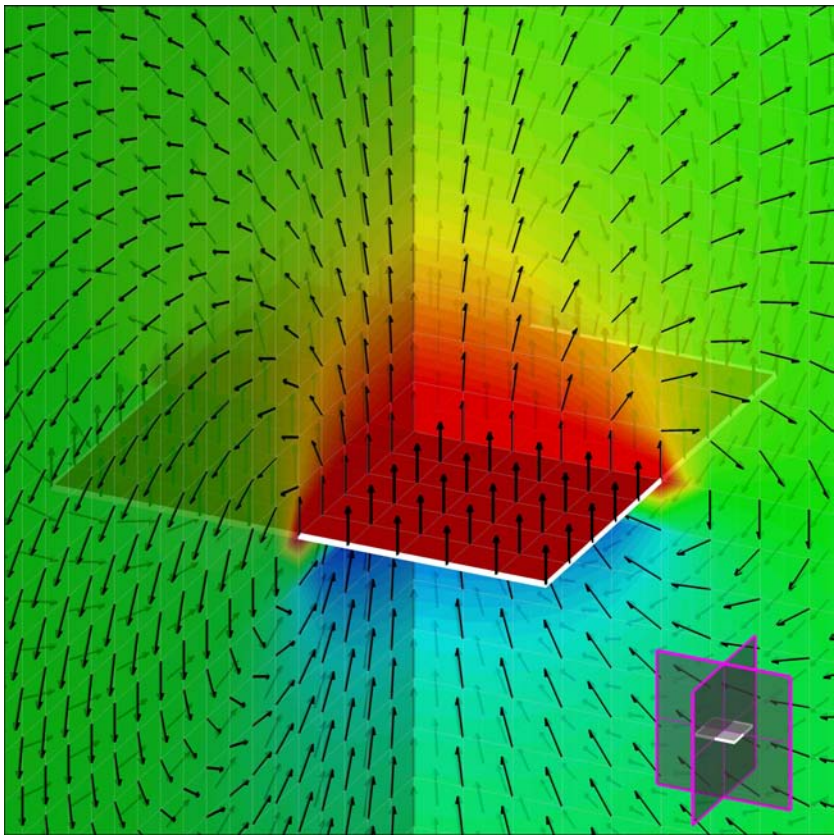

Figure 2.4: quadrilateral doublet - uniform velocity vector and isopotential contour.

way because

$$\phi_{doublet} = -\frac{\partial}{\partial n}\phi_{source} \tag{2.16}$$

As the source element, equation (2.12) shows that there exists a discontinuity when $z = 0$:

$$\phi(z = \pm 0) = \frac{\pm\mu}{2} \tag{2.17}$$

Similar to the previous case, the potential and velocity fields illustrated in figure 2.4 are based on the implementation of the obtained equations.

2.1.3 Constant doublet panel equivalence to vortex ring

Continue to consider the quadrilateral doublet with constant strength μ with its potential which may be written as

$$\phi = -\frac{\mu}{4\pi}\int_S \frac{z}{r^3}dS \tag{2.18}$$

where $r = \sqrt{(x-x_0)^2 + (y-y_0)^2 + z^2}$.

The velocity is

$$\begin{aligned}\underline{U} = \underline{\nabla}\phi = -\frac{\mu}{4\pi}\int_S \underline{\nabla}\frac{z}{r^3}dS = \\ = \frac{\mu}{4\pi}\int_S \left[\mathbf{i}\frac{\partial}{\partial x_0}\frac{z}{r^3} + \mathbf{j}\frac{\partial}{\partial y_0}\frac{z}{r^3} + \mathbf{k}\left(\frac{1}{r^3} - \frac{3z}{r^5}\right)\right]dS\end{aligned} \tag{2.19}$$

where

$$\frac{\partial}{\partial x}\frac{1}{r^3} = -\frac{\partial}{\partial x_0}\frac{1}{r^3} \tag{2.20}$$

$$\frac{\partial}{\partial y}\frac{1}{r^3} = -\frac{\partial}{\partial y_0}\frac{1}{r^3} \tag{2.21}$$

Now, consider a vortex filament of circulation Γ along the curve bounding the quadrilateral, labeled as C (figure 2.5). Clearly, the velocity field induced by this filament is given by the Biot-Savart law (see chapter 1) as

$$\underline{U} = \frac{\Gamma}{4\pi}\int_C \frac{d\underline{\ell}\times\underline{r}}{|\underline{r}|^3} \tag{2.22}$$

Thus, for $d\underline{\ell} = (dx_0, dy_0)$ and $\underline{r} = (x-x_0, y-y_0, z)$, the velocity results expressed as following

$$\underline{U} = \int_C \left\{\mathbf{i}\frac{z}{r^3}dy_0 - \mathbf{j}\frac{z}{r^3}dx_0 + \mathbf{k}\left[(y-y_0)dx_0 - (x-x_0)dy_0\right]\right\} \tag{2.23}$$

At this point, recall Stokes theorem for a vector $\underline{A}$

$$\int_C \underline{A}\cdot d\underline{\ell} = \int_S \underline{n}\cdot\underline{\nabla}\times\underline{A}dS \tag{2.24}$$

With $\underline{n} = \underline{k}$ above equation becomes

$$\int_C \underline{A} \cdot d\underline{\ell} = \int_S \left(\frac{\partial A_y}{\partial x_0} - \frac{\partial A_x}{\partial y_0} \right) dS \tag{2.25}$$

Applying Stokes theorem on the above velocity integral, one gets

$$\underline{U} = \frac{\Gamma}{4\pi} \int_S \left[\mathbf{i} \frac{\partial}{\partial x_0} \frac{z}{r^3} + \mathbf{j} \frac{\partial}{\partial y_0} \frac{z}{r^3} - \mathbf{k} \left(\frac{\partial}{\partial x_0} \frac{x - x_0}{r^3} + \frac{\partial}{\partial y_0} \frac{y - y_0}{r^3} \right) \right] dS \tag{2.26}$$

Therefore, if $\Gamma = \mu$ the velocity field induced by the vortex ring is identical to the velocity of the doublet quadrilateral (see also figure 2.4).

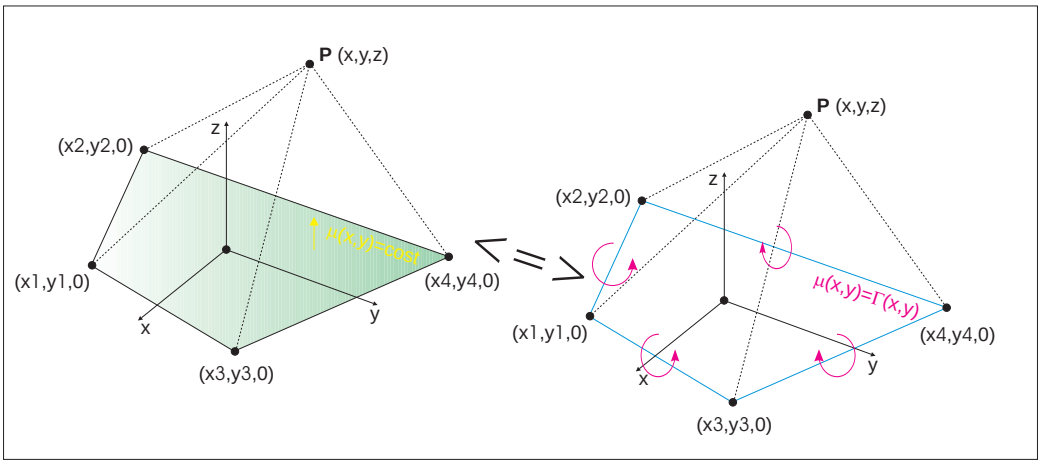

Figure 2.5: quadrilateral doublet element and its vortex ring equivalent.

2.2 Panel method formulation

For most engineering applications the problem requires a solution in a fluid domain. Usually this domain contains a solid body with additional boundaries that may define an outer flow boundary.

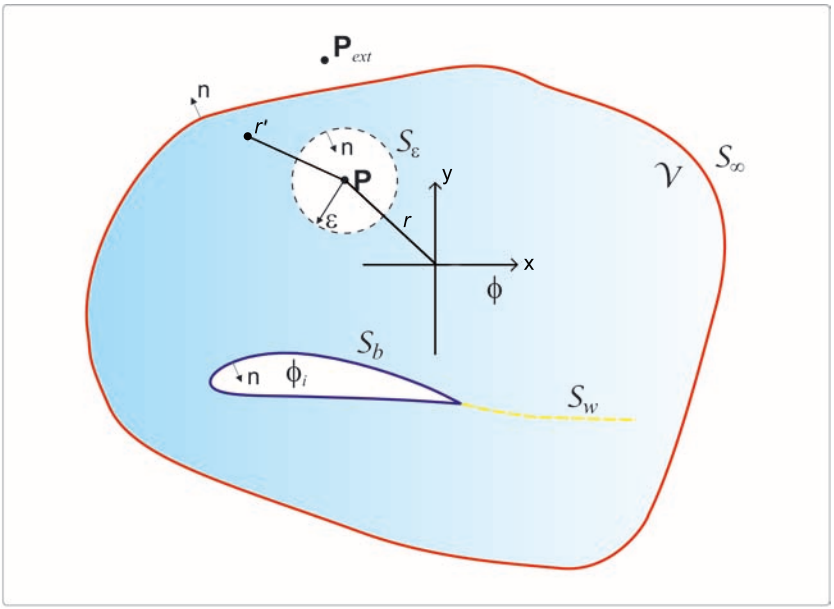

Figure 2.6: The fluid domain considered in the derivation of the Green's Theorem.

Consider the scalar potential governed by Laplace's equation:

$$\nabla^2 \phi = 0. \tag{2.27}$$

The mathematical problem defined by Laplace's equation with the boundary conditions is described schematically by figure 2.6. Laplace's equation must be solved for an arbitrary body with boundary S_B enclosed in a volume V, with the outer boundary S_∞ (with the normal defined so that it always points outside the region of interest V) [14][34][25][41][30].

Inside the domain V the general solution of Laplace's equation is possible to obtain by means of the Green's Identity that follows from the divergence

theorem that is

$$\iint_S \underline{A} \cdot \underline{n} dS = \iiint_V \underline{\nabla} \cdot \underline{A} dV \tag{2.28}$$

Particularly, consider the vector

$$\underline{A} = \phi_1 \underline{\nabla} \phi_2 - \phi_2 \underline{\nabla} \phi_1 \tag{2.29}$$

where ϕ_1 and ϕ_2 are two scalar functions of position. Applying the divergence theorem to the vector $\underline{A}$, results:

$$\iint_S (\phi_1 \underline{\nabla} \phi_2 - \phi_2 \underline{\nabla} \phi_1) \cdot \underline{n} dS = \iiint_V \left(\phi_1 \nabla^2 \phi_2 - \phi_2 \nabla^2 \phi_1\right) dV \tag{2.30}$$

This equation is the second of Green's Identities where the surface integral is taken over all the boundaries S, including a wake sheet model S_W (necessary to impose the Kutta condition) and the outer boundary S_∞:

$$S = S_B + S_W + S_\infty \tag{2.31}$$

Let one set

$$\phi_1 = \frac{1}{r} \tag{2.32}$$

and

$$\phi_2 = \phi \tag{2.33}$$

where ϕ is the potential of the flow in V, and r is the distance from a point $P(x, y, z)$ is another potential that satisfies Laplace's equation.

This way the second Green's Identity results:

$$\iint_S \left(\frac{1}{r} \underline{\nabla} \phi - \phi \underline{\nabla} \frac{1}{r}\right) \cdot \underline{n} dS = \iiint_V \left(\frac{1}{r} \nabla^2 \phi - \phi \nabla^2 \frac{1}{r}\right) dV \tag{2.34}$$

When the point P is outside of V, equation (2.34) becomes

$$P \notin V \Longrightarrow \iint_S \left(\frac{1}{r} \underline{\nabla} \phi - \phi \underline{\nabla} \frac{1}{r}\right) \cdot \underline{n} dS = 0 \tag{2.35}$$

In the particular case where the point P is inside the region, the point P must be excluded from the region of integration and it is surrounded by a small sphere of radius ϵ. In the remaining region V outside of the sphere ϵ both ϕ_1 and ϕ_2 satisfy Laplace's equation. Therefore, equation (2.34) becomes

$$P \in V \Longrightarrow \iint\limits_{S+S_\epsilon} \left(\frac{1}{r} \underline{\nabla} \phi - \phi \underline{\nabla} \frac{1}{r} \right) \cdot \underline{n} dS = 0 \tag{2.36}$$

Now introduce a spherical coordinate system at P to obtain the integral over the sphere. Since the vector $\underline{n}$ points inside the small sphere, equation (2.36) becomes

$$\iint\limits_{S} \left(\frac{1}{r} \underline{\nabla} \phi - \phi \underline{\nabla} \frac{1}{r} \right) \cdot \underline{n} dS - \iint\limits_{S_\epsilon} \left(\frac{1}{r} \frac{\partial \phi}{\partial r} + \frac{\phi}{r^2} \right) dS = 0 \tag{2.37}$$

The integration over the surface of the spherical exclusion region reduces to:

$$\iint\limits_{S_\epsilon} \left(\frac{\phi}{r^2} \right) dS = 4\pi\phi(P) \tag{2.38}$$

Finally, equation (2.37) becomes

$$\phi(P) = \frac{1}{4\pi} \iint\limits_{S} \left(\frac{1}{r} \underline{\nabla} \phi - \phi \underline{\nabla} \frac{1}{r} \right) \cdot \underline{n} dS \tag{2.39}$$

Equation (2.39) is the third Green's Identity that gives the value of the $\phi(P)$ at any point in the flow, within the region V, in terms of the values of the ϕ and $\partial\phi/\partial n$ on the boundaries S.

When the flow of interest occurs inside the boundary of the S_B and hence the resulting *internal potential* is ϕ_i, the point P inside the region V is outside of S_B and applying equation (2.35), results

$$0 = \frac{1}{4\pi} \iint\limits_{S_B} \left(\frac{1}{r} \underline{\nabla} \phi_i - \phi_i \underline{\nabla} \frac{1}{r} \right) \cdot \underline{n} dS \tag{2.40}$$

where $\underline{n}$ points out from S_B.

By adding equations (2.39) and (2.40), we obtain the formula that includes the influence of the inner potential:

$$\phi(P) = \frac{1}{4\pi} \iint_{S_B} \left[\frac{1}{r} \underline{\nabla}(\phi - \phi_i) - (\phi - \phi_i) \underline{\nabla} \frac{1}{r} \right] \cdot \underline{n} dS +$$

$$+ \frac{1}{4\pi} \iint_{S_W + S_\infty} \left(\frac{1}{r} \underline{\nabla}\phi - \phi \underline{\nabla} \frac{1}{r} \right) \cdot \underline{n} dS \tag{2.41}$$

Regarding the contribution of the S_∞ integral in equation (2.41), this can be defined as

$$\phi_\infty(P) = \frac{1}{4\pi} \iint_{S_\infty} \left(\frac{1}{r} \underline{\nabla}\phi - \phi \underline{\nabla} \frac{1}{r} \right) \cdot \underline{n} dS \tag{2.42}$$

This contribution depends on the reference frame: for example, this potential can be selected as a constant in the region in an inertial system where the body moves through an otherwise stationary fluid. Furthermore, since the wake surface is assumed to be thin, $\partial\phi/\partial n$ is continuous across it. By means of these assumptions, equation (2.41) becomes

$$\phi(P) = \phi_\infty(P) + \frac{1}{4\pi} \iint_{S_B} \left[\frac{1}{r} \underline{\nabla}(\phi - \phi_i) - (\phi - \phi_i) \underline{\nabla} \frac{1}{r} \right] \cdot \underline{n} dS +$$

$$- \frac{1}{4\pi} \iint_{S_W} (\phi_U - \phi_L) \underline{n} \cdot \underline{\nabla} \frac{1}{r} dS \tag{2.43}$$

This formula provides the value of $\phi(P)$ in terms of ϕ and $\partial\phi/\partial n$ on the boundaries. One can observe that the flow problem reduces to determining the value of ϕ and $\partial\phi/\partial n$ on the boundaries.

When the point P lies on the boundary S_B, the potential $\phi(P)$ becomes singular. Therefore, in order to exclude the point from V, the integration is carried out only around the surrounding hemisphere. Equation (2.43)

becomes

$$\phi(P \in S_b) = \phi_\infty(P) + \frac{1}{4\pi}\int\int_{S_B} \frac{1}{r}\underline{n}\cdot\underline{\nabla}(\phi-\phi_i)dS+$$

$$-\frac{1}{4\pi}\int\int_{S_B-P}(\phi-\phi_i)\underline{n}\cdot\underline{\nabla}\frac{1}{r}dS \pm \frac{1}{2}(\phi-\phi_i)_p+$$

$$-\frac{1}{4\pi}\int\int_{S_W}(\phi_U-\phi_L)\underline{n}\cdot\underline{\nabla}\frac{1}{r}dS \tag{2.44}$$

where the factor $1/2$ is due to the use of the hemisphere instead of the sphere, and the sign is due to the direction of $\underline{n}$.

The solution of the above relationship let us evaluate the potential in any point P that lies on the boundary S_B, in terms of ϕ and $\partial\phi/\partial n$ on the boundaries.

2.2.1 Boundary conditions

The solution of equation (2.44) must satisfy a number of known boundary conditions which can be imposed on the solid surfaces and the fluctuating wake. Particularly, the Neumann condition must be satisfied on the surface S_B so:

$$\underline{n}\cdot\underline{\nabla}\phi = -U_{n_T} - U_{n_R} \tag{2.45}$$

where U_{n_R} is the resultant normal component of velocity relative to the surface due to the motion of the body, and U_{n_T} is the normal component of the velocity due to possible flows of transpiration through the surface, therefore this term is zero for the case of a solid boundary with no transpiration.

Instead, no condition in terms of potential results a necessity on the surface S_W, because it itself represents the imposition of the wing trailing edge

Kutta condition. The rise in potential lies in the fact that it must assure that the velocity does not rotate round the trailing edge. This way the presence of the wake does not introduce additional unknowns to the problem, because the rise in potential on the wake is associated to the unknown potentials near the trailing edge and the contribution of the S_W integral must be considered as a known term.

However, a constraint exists for the wake, due to the wake form. This form must be determined considering that the wake cannot support a load, because the wake is not a solid surface. Therefore, the wake form must be aligned with the local flow direction, which means to establish a condition of tangency of the velocity in every point:

$$\underline{U} \cdot \underline{n}|_{S_W} = 0 \tag{2.46}$$

Note that it is necessary to know the flow field $\underline{U}$ but the goal of the analysis is $\underline{U}$. This non-linearity can be overpassed to approach the wake with a fixed form, independent of the flow field, or with the support of solution iterative techniques.

2.2.2 Singularity model

A given flow field can be obtained from an infinite number of configurations of distributions of singularities (sources and doublets) on the problem boundaries (S_B, S_W), each combination producing a different flow in the inside region.

A unique combination of singularities can be obtained with different singularity models. Particularly, one way that can be considered is to specify one of the singularity distributions and to solve for other using boundary conditions only on the side of the boundary. Another way is to apply certain

constraining relationships on the singularity distributions.

One important characteristic for certain of the singularity models from the numerical point of view, is that the flow field generated in the inner region by the model is related to the boundary [41]. Particularly, the jump from the internal flow to the external flow should be a small passing through the boundary. Therefore, a minimum perturbation from the singularities is required. To satisfy this requisite one can treat the internal flow directly in equation (2.44), obtaining a unique singularity distribution by specifying boundary conditions on both sides of the surface. In this case, the inner velocity potential ϕ_i is specified directly in equation (2.44): this is an internal Dirichlet boundary condition. Particularly, consider the internal flow equal to outset flow $\phi_i = \phi_\infty$. This way, equation (2.44) becomes:

$$0 = \frac{1}{4\pi} \int\int_{S_B} \frac{1}{r} \underline{n} \cdot \underline{\nabla}(\phi - \phi_\infty) dS +$$

$$-\frac{1}{4\pi} \int\int_{S_B - P} (\phi - \phi_\infty) \underline{n} \cdot \underline{\nabla} \frac{1}{r} dS + \frac{1}{2}(\phi - \phi_\infty)_p +$$

$$-\frac{1}{4\pi} \int\int_{S_W} (\phi_U - \phi_L) \underline{n} \cdot \underline{\nabla} \frac{1}{r} dS \tag{2.47}$$

where the perturbation potential on the exterior surface $\phi - \phi_\infty$, is now the doublet density

$$4\pi\mu = \phi - \phi_\infty \tag{2.48}$$

whereas the source distribution is

$$4\pi\sigma = -\underline{n} \cdot (\underline{\nabla}\phi - \underline{\nabla}\phi_\infty) = -U_n + U_{n_\infty} \tag{2.49}$$

Note that the source distribution is therefore established at the outset.

At this point, equation (2.47) becomes

$$\iint_{S_B} \frac{\sigma}{r} dS - \iint_{S_B - P} \mu \underline{n} \cdot \underline{\nabla} \frac{1}{r} dS + 2\pi\mu_p - \iint_{S_W} \mu^w \underline{n} \cdot \underline{\nabla} \frac{1}{r} dS = 0 \qquad (2.50)$$

where $\mu^w = (\phi_U - \phi_L)/4\pi$ is the known wake doublet density at the trailing edge.

Moreover, note that sources and doublets have a physical sense. The thickness effects can be simulated by means of the doublets, the non symmetrical conditions by means of the sources.

Equation (2.49) shows that the Neumann condition can be satisfied only by the sources and the sources are known too.

So far thick configurations having a distinct internal volume enclosed by the surface S have been concerned. When the configurations having a indistinct internal volume (parts of the configuration are extremely thin), then these configurations can be represented by open surfaces. In this case, equation (2.43) becomes

$$\begin{aligned} \phi(P) = \phi_\infty(P) \; + \; & \frac{1}{4\pi} \iint_{S_B} \left(\frac{1}{r} \underline{\nabla}(\phi_U - \phi_L) - (\phi_U - \phi_L) \underline{\nabla} \frac{1}{r} \right) \cdot \underline{n} dS + \\ - \; & \frac{1}{4\pi} \iint_{S_W} \mu^w \underline{n} \cdot \underline{\nabla} \frac{1}{r} dS \end{aligned} \qquad (2.51)$$

If the normal velocity is continuous through the sheet then the term $\underline{n} \cdot (\underline{\nabla}\phi_U - \underline{\nabla}\phi_L) = 0$, disappearing the source term and the above relationship becomes:

$$\phi(P) = \phi_\infty(P) - \iint_{S_B} \mu \underline{n} \cdot \underline{\nabla} \frac{1}{r} dS - \iint_{S_W} \mu^w \underline{n} \cdot \underline{\nabla} \frac{1}{r} dS \qquad (2.52)$$

where $\mu = (\phi_U - \phi_L)/4\pi$ is the jump in total potential across the sheet.

Applying the external Neumann boundary condition, then

$$\underline{n} \cdot \underline{\nabla}\phi(P) = \underline{n} \cdot \underline{\nabla}\phi_\infty(P) - \iint_{S_B} \mu \underline{n} \cdot \underline{\nabla} \left(\underline{n} \cdot \underline{\nabla} \frac{1}{r} \right) dS +$$

$$-\int\int_{S_W} \mu^w \underline{n} \cdot \underline{\nabla} \left(\underline{n} \cdot \underline{\nabla} \frac{1}{r} \right) dS \tag{2.53}$$

where $\underline{n} \cdot \underline{\nabla}\phi(P) = 0$ in case of no transpiration.

Equations (2.50) and (2.53) are the basic equations for the solution of the flow problem. These equation can be written so:

$$\phi(P) = \phi_\infty(P) + \phi'(P) \tag{2.54}$$

$$\underline{n} \cdot \underline{\nabla}\phi(P) = \underline{n} \cdot \underline{\nabla}\phi_\infty(P) + \underline{n} \cdot \underline{\nabla}\phi'(P) \tag{2.55}$$

where ϕ' represents the potential of perturbation.

By means of the resolution of these equations the unknown singularity distributions may be obtained on the body surface and that content to compute the flow field by means of the derivation of the potential.

2.2.3 Computation of velocities and forces

Once the singularity distribution strengths are known, the total velocity in every point of the domain is possible to compute by means of the following equation

$$\underline{U}(P) = \underline{U}_\infty(P) - \int\int_{S_B} \mu \underline{\nabla} \left(\underline{n} \cdot \underline{\nabla} \frac{1}{r} \right) dS +$$

$$+ \int\int_{S_B} \sigma \underline{\nabla} \frac{1}{r} dS - \int\int_{S_W} \mu^w \underline{\nabla} \left(\underline{n} \cdot \underline{\nabla} \frac{1}{r} \right) dS \tag{2.56}$$

The above relationship is the basic for many numerical solutions and has been obtained by taking the gradient of total scalar potential of equation (2.43).

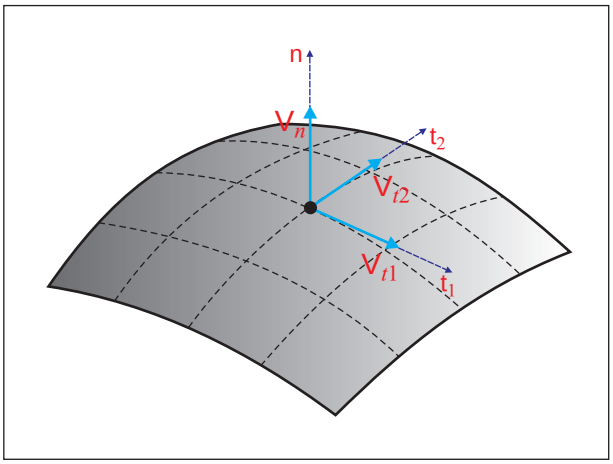

Figure 2.7: panel local reference frame for evaluating the normal and tangential velocity components.

Instead, when the point P lies on the boundary, it is necessary to consider equation (2.44) and to use following equation

$$\underline{U}(P \in body) = \underline{U}_\infty(P) - 2 \iint_{S_B - P} \mu \underline{\nabla} \left(\underline{n} \cdot \underline{\nabla} \frac{1}{r} \right) dS +$$

$$+2 \iint_{S_B} \sigma \underline{\nabla} \frac{1}{r} dS - 2 \iint_{S_W} \mu^w \underline{\nabla} \left(\underline{n} \cdot \underline{\nabla} \frac{1}{r} \right) dS \qquad (2.57)$$

However, as the particular choice of the source values, it is possible to compute the velocity by taking the gradient of the potential in a local reference frame centered in the point of interest, as showed in figure 2.7.

In fact, as the normal component of velocity disturbance has been established, it is possible to compute the tangential components of the same velocity disturbance by means of the derivatives of the doublet intensity along two direction tangential to the body:

$$\underline{u}(P) = u_{t_1} \mathbf{i}_{t_1} + u_{t_2} \mathbf{i}_{t_2} + u_n \mathbf{i}_n = \frac{\partial \mu}{\partial t_1} \mathbf{i}_{t_1} + \frac{\partial \mu}{\partial t_2} \mathbf{i}_{t_2} - \sigma \mathbf{i}_n \qquad (2.58)$$

In the case of a Neumann boundary condition, above equation becomes:

$$\underline{u}(P) \;=\; \pm\frac{\partial\mu/2}{\partial t_1}\mathbf{i}_{t_1} \;\pm\; \frac{\partial\mu/2}{\partial t_2}\mathbf{i}_{t_2} \;-\; \underline{U}_\infty \cdot \mathbf{i}_n \tag{2.59}$$

where the signs $+/-$ represent the upper and lower sides, respectively. These components will be summed at the un-disturbed local velocity in order to obtain the total velocity:

$$\underline{U}(P \in \textit{body}) = \underline{U}_\infty(P) + \underline{u}(P) \tag{2.60}$$

After the distributions of velocity and $\partial\phi/\partial t$ have been computed on the bodies, by means of Bernoulli theorem, one may obtain the corresponding distributions of pressure to integrate in order to compute forces and moments.

2.3 Panel method numerical procedure

In the above section, the solution to the potential flow problem has been obtained analytically, only after some geometrical simplifications in the boundary conditions have been made.

In most of the cases, the numerical application is characterized by the treatment of more realistic geometries and the fulfillment of the boundary conditions on the corresponding surface. In this section, the numerical procedure will be examined.

The numerical method to solve the potential flow problem is based on the surface distribution of singularity elements, then the problem solution has been reduced to finding the strength of these elements.

From the numerical point of view, a solution can be obtained if the body and wake geometries are discretized separately from singularity distribution [30]. In most of applications, the body and wake surfaces are represented

by a large number of small quadrilateral and/or triangular regions which are planar in most methods. These small quadrilateral regions are called panels defined by functions of the kind $z = f(x, y)$ in a local reference frame (see figure 2.8); therefore this type of method is called panel method. Thus, as the body is divided into N surface panels, so the wake is represented by N_w wake panels. Every single panel is characterized by means of its grid points.

By means of the discretization process, panels are defined by polynomials on which the order of desired accuracy to represent the real geometry depends. This accuracy rises with the polynomial order.

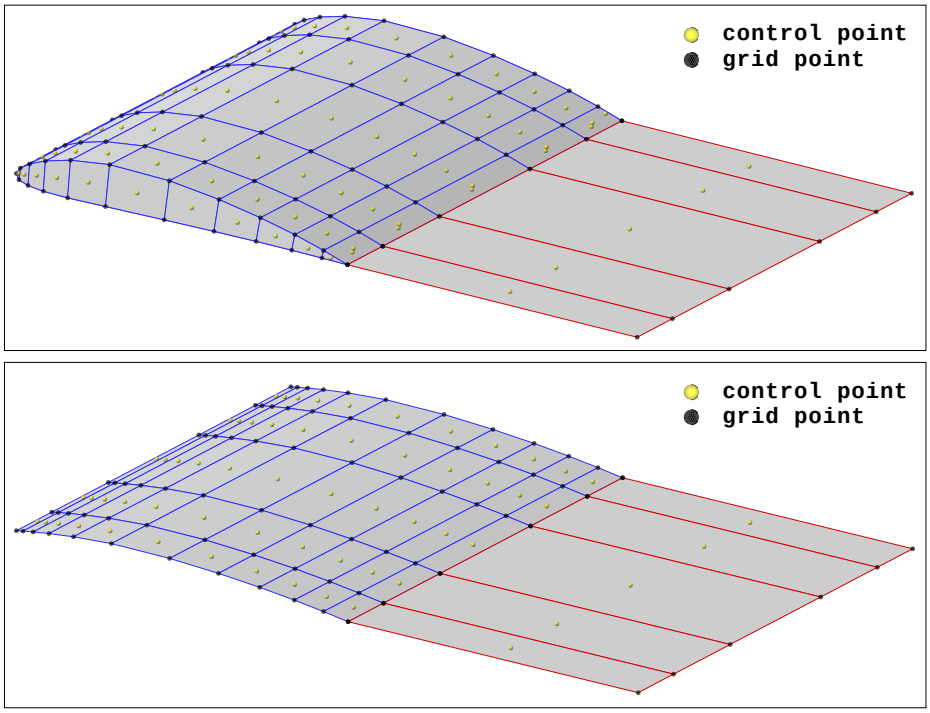

Figure 2.8: examples of discretized (thick and thin) body and wake geometries.

The singularity distribution must be subdivided into panels which are coinciding with the body panels where the singularity strength may be assumed constant (low-order), linearly variable (first order) or parabolic (second order). Generally, the order of accuracy used for the singularity distribution

is equal to the order of the body discretization, since the schematization accuracy of lower order should be, however, decisive.

For the singularities, the simplest discretization is the constant strength over quadrilateral panel, defined by plane surfaces and rectilinear borders. This discretization allows to have a notable simplicity of calculus and of numerical implementation but requires a great number of panels in order to compensate the accuracy loss due to low polynomial order. However, this choice results to be the most used technique of panels methods.

Once the body and wake surfaces have been discretized, the control point in which the boundary condition must be imposed results automatically individuated into the centroid of each panel. For thick bodies, the condition of zero normal flow or assigned normal flow across the body surfaces may be defined by using Dirichlet formulation (2.50). For thin bodies, this condition may be defined by using Neumann formulation (2.53), as seen in previous section. Thus, equations (2.50) and (2.53) may be rewritten in each control point of N_B panels (of which N_B^d of Dirichlet type and N_B^n of Neumann type) present on the surfaces. Particularly, let J, r_J and N_w be the panel in which the boundary condition is imposed on the control point (see figure 2.9), the distance respect to the panel of which the effect is computed and the wake panel number, respectively, results

$$\sum_{K=1}^{N_B} \iint_{panel\ K} \mu_K \ \underline{n} \cdot \underline{\nabla} \ \frac{1}{r_J} dS + \sum_{L=1}^{N_W} \iint_{panel\ L} \mu_L^w \ \underline{n} \cdot \underline{\nabla} \ \frac{1}{r_J} dS =$$

$$= \sum_{K=1}^{N_B} \iint_{panel\ K} \sigma_K \ \frac{1}{r_J} dS \qquad (J=1,...,N_B^d) \qquad (2.61)$$

$$\sum_{K=1}^{N_B} \underline{n}_J \cdot \iint_{panel\ K} \mu_K \underline{\nabla} \left(\underline{n} \cdot \underline{\nabla} \frac{1}{r_J} \right) dS + \sum_{L=1}^{N_W} \underline{n}_J \cdot \iint_{panel\ L} \mu_L^w \underline{\nabla} \left(\underline{n} \cdot \underline{\nabla} \frac{1}{r_J} \right) dS =$$

$$= \sum_{K=1}^{N_B} \underline{n}_J \cdot \iint_{panel\ K} \sigma_K \underline{\nabla} \frac{1}{r_J} dS - \underline{n}_J \cdot (\underline{U} - \underline{U}_\infty) \quad (J = 1, ..., N_B^n) \tag{2.62}$$

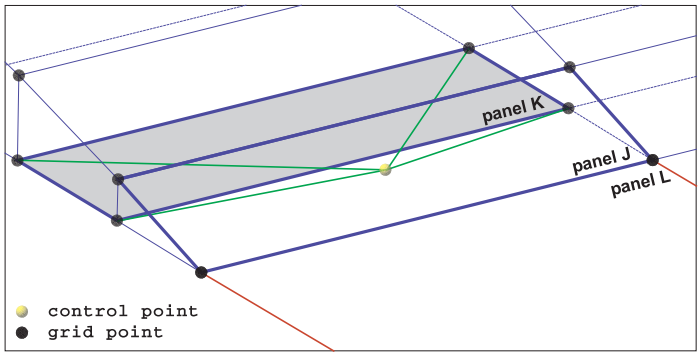

Figure 2.9: schematization for the influence coefficients.

The integrals in the above equations are over the single panel surface, and each one represents the influence that the generic panel K or L produces on the control point of the panel J. Moreover, these integrals may be substituted by summations extended to the corresponding grid points. For the elements with constant or unitary singularity strength, this influence is due only to the panel geometry and it may be synthesized using some coefficients, called

influence coefficients:

$$B^d_{JK} = \int\int_{panel\ K} \frac{1}{r_J} dS \tag{2.63}$$

$$B^n_{JK} = \underline{n}_J \cdot \underline{U}^\sigma_{JK} \quad ; \quad \underline{U}^\sigma_{JK} \int\int_{panel\ K} \underline{\nabla} \frac{1}{r_J} dS \tag{2.64}$$

$$C^d_{JK} = \int\int_{panel\ K} \underline{\nabla} \frac{1}{r_J} dS \; ; \quad C^d_{JJ} = -2\pi \tag{2.65}$$

$$C^n_{JK} = \underline{n}_J \cdot \underline{U}^\mu_{JK} \quad ; \quad \underline{U}^\mu_{JK} \int\int_{panel\ K} \underline{\nabla} \left(\underline{n} \cdot \frac{1}{r_J} \right) dS \tag{2.66}$$

where the apexes d and n are always indicative of the imposed condition type.

By using the influence coefficients, equations (2.61) and (2.62) become

$$\sum_{K=1}^{N_B} C^d_{JK} \mu_K + \sum_{K=1}^{N_W} C^d_{JK} \mu^w_L = \sum_{K=1}^{N_B} B^d_{JK} \sigma_K \qquad (J = 1, ..., N^d_B) \tag{2.67}$$

$$\sum_{K=1}^{N_B} C^n_{JK} \mu_K + \sum_{K=1}^{N_W} C^n_{JK} \mu^w_L = \sum_{K=1}^{N_B} B^n_{JK} \sigma_K \; - \underline{n}_J \cdot (\underline{U} - \underline{U}_\infty)_J \qquad (J = 1, ..., N^n_B) \tag{2.68}$$

When the source strengths related to the condition of zero normal flow across the body surfaces (equation (2.49)) are assigned for thick bodies or fixed equal to zero for thin body, it is possible compute the influence coefficients B^d_{JK} e B^n_{JK}, letting unknown only the doublet terms. Moreover, the Kutta condition permits to rewrite also the wake doublets μ^w_L in function of the body doublets μ_K. In fact, for thick body, every single wake panel will have one side coinciding with the trailing edge of the body on which two panels (one upper panel, one lower panel) of the same body converge.

Let μ_L^u, μ_L^l, μ_L^w be the doublet strength of the upper panel, the doublet strength of the lower panel, and the doublet strength of the near wake panel (see figure 2.10), by the Kutta condition results

$$\mu_L^w = \mu_L^u - \mu_L^l \tag{2.69}$$

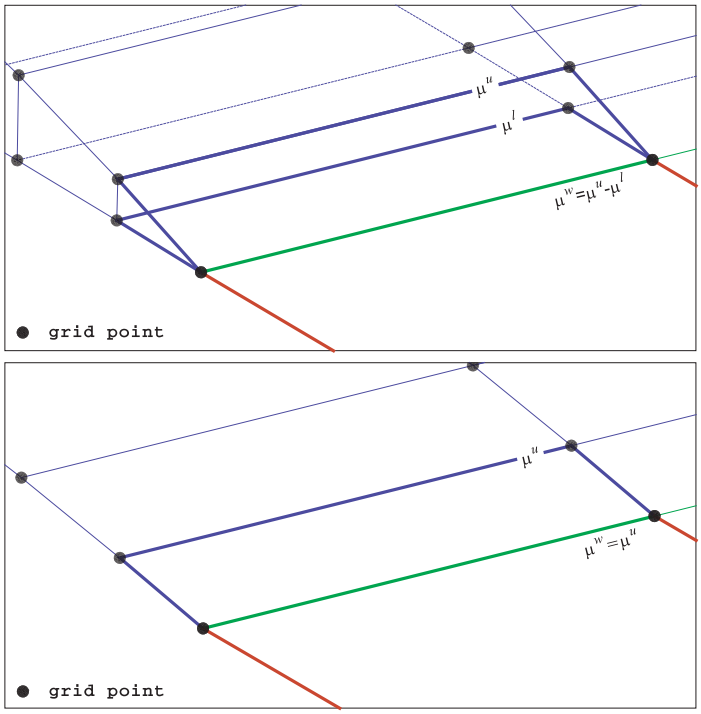

Figure 2.10: reference frame for the Kutta condition.

As for the bodies without thickness (figure 2.10), there is not difference between upper and lower, therefore

$$\mu_L^w = \mu_L^l \tag{2.70}$$

Thus, the influence of any panel wake becomes:

$$C_{JK}^d \mu_L^w = C_{JK}^d(\mu_L^u - \mu_L^l) \tag{2.71}$$

$$C_{JK}^n \mu_L^w = C_{JK}^n \mu_L^l \tag{2.72}$$

Equations (2.71) and (2.72) consent to trace the doublet influence of the doublets on the wake panels back to the corresponding doublets near the trailing edge, correcting simply the influence coefficients C^d_{JK} and C^n_{JK}, thus

$$A^d_{JK} = C^d_{JK} \qquad \textit{panel K not at the trailing edge} \tag{2.73}$$

$$A^d_{JK} = C^d_{JK} - C^d_{JL} \qquad \textit{panel K at the upper trailing edge} \tag{2.74}$$

$$A^d_{JK} = C^d_{JK} + C^d_{JL} \qquad \textit{panel K at the lower trailing edge} \tag{2.75}$$

$$A^n_{JK} = C^n_{JK} \qquad \textit{panel K not at the trailing edge} \tag{2.76}$$

$$A^n_{JK} = C^n_{JK} + C^n_{JL} \qquad \textit{panel K at the trailing edge} \tag{2.77}$$

Finally, one obtains:

$$\sum_{K=1}^{N_B} A^d_{JK}\mu_k = \sum_{K=1}^{N_B} B^d_{JK}\sigma_K \qquad (J = 1, ..., N^d_B) \tag{2.78}$$

$$\sum_{K=1}^{N_B} A^n_{JK}\mu_k = \sum_{K=1}^{N_B} B^n_{JK}\sigma_K - \underline{n}_J \cdot (\underline{U} - \underline{U}_\infty)_J \qquad (J = 1, ..., N^n_B) \tag{2.79}$$

Another condition of the wake form must be added to equations (2.78) and (2.79). This is a no-linear problem since this condition corresponds to the imposition of a variation of the wake form which fluctuates freely in the domain [15]. In the case of flexible wake, this condition may be imposed by annulling the normal velocity components in the control points of every single wake panel:

$$\underline{U} \cdot \underline{n}_L = 0 \quad (L = 1, ..., N_W) \tag{2.80}$$

Equations (2.78) and (2.79) for the N_B control point drive to a set of N_B linear algebraic equations in the N_B strength unknown of surface doublets μ_K.

The numerical solution of this set is generally stable, because the unknown doublet distribution is quite little, since it is due to only perturbation potential.

2.3.1 Unsteady panel methods

The method of solution of incompressible, irrotational flow that is developed so far does not include the unsteady nature of the problem. Therefore, it will be shown that this method may include time-dependency that will be introduced through the boundary conditions and the use of the unsteady Bernoulli equation.

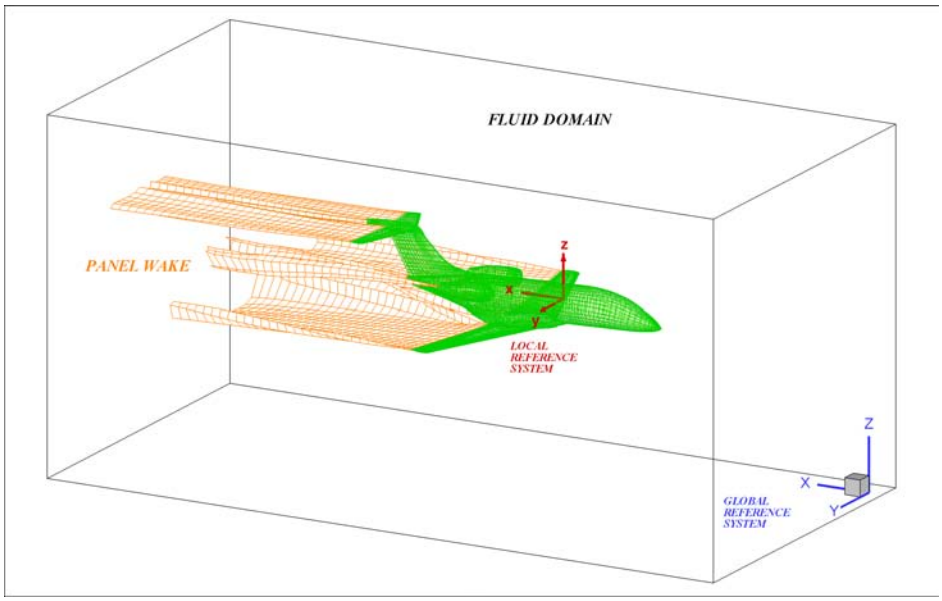

Figure 2.11: inertial frame and body frame used to describe the motion of the body.

The choice of the coordinate systems is very important for the formulation of the unsteady problem. In order to prescribe correctly the boundary conditions on the solid body surfaces, consider a body-fixed coordinate system $(0, x, y, z)$ and a fixed-in-space global reference frame $(0, X, Y, Z)$ which is assumed to be known, as illustrated in figure 2.11. Suppose the body motion law is known, the zero normal flow boundary condition becomes:

$$\frac{\partial \phi}{\partial n} = (\underline{U}_\infty - \underline{U}_r - \underline{\Omega} \times \underline{r}) \cdot \underline{n} \tag{2.81}$$

where $\underline{r} = \underline{r}(x, y, z)$, $\underline{U}_\infty$, $\underline{U}_r$ and $\underline{\Omega}$ are the position of any point in the body reference frame, the velocity of the body frame origin in global coordinates, the relative motion of the surface due to deformation of the body, the angular velocity, respectively.

2.3.2 Unsteady panel wake model

Regarding the wake, the solution is based on a time-stepping technique: the wake is formed in the inertial coordinate system as the body from which the wake separates moves away from its initial position, shedding from known separation lines on the surface body (trailing edges of wings, for example). During every single time step, the wing moves along its flight path and every trailing edge vortex panel sheds a wake panel with a strength (related to the Kutta condition) corresponding to its circulation in the previous time step. It is as if the trailing edge leaves its "tracks" during its pass or, if the body is motionless and surrounded by the stream, the trailing edge is trailed by the flow [14] (see figure 2.12). So a new row of wake panels is added to the wake at the separation line and all the preexisting rows of wake panels are convected downstream with the local velocity field in the inertial reference frame at each time step [9][10][8][13].

In detail, at the beginning of the motion no wake panels exist but only the wing bound vortex panels exist where the closing segment of the trailing edge vortex elements represents the starting vortex or separation line.

During the second time step, the wing is moved along its flight path and each trailing edge vortex panel sheds a wake panel. This first wake sheet, used to account for the vorticity recently shed into the domain from the wing trailing edge, imposes a well defined potential jump at the trailing edge to satisfy the Kutta condition: this condition is used as a boundary condition

to determine the strength of the doublets to be shed into the first row of a wake. Therefore, every single wake panel has a vortex strength equal to the circulation obtained by fulfilling the Kutta condition at the trailing edge. Once the trailing edge vortexes are given, the buffer wake sheet is determined automatically.

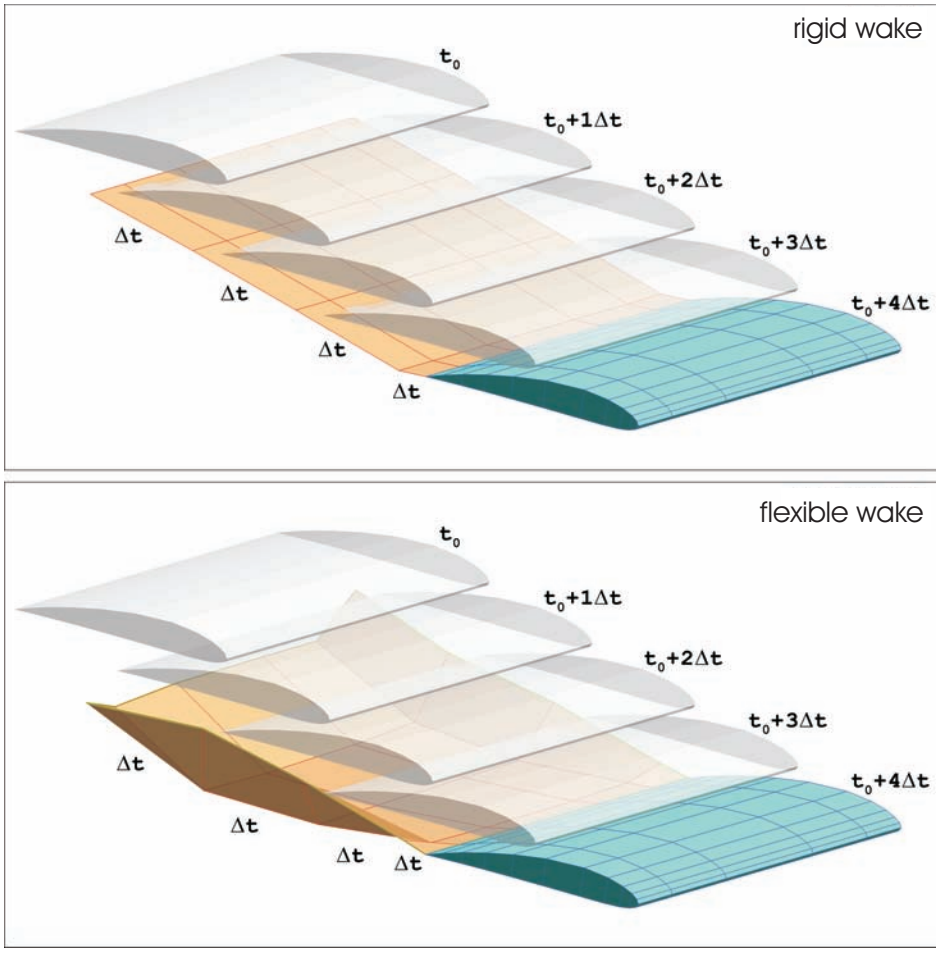

Figure 2.12: examples of generation of rigid (above) and flexible (below) unsteady wake.

During the third time step, two rows of wake panel exist: new first row of wake panels closest to the trailing edge where the Kutta condition must be imposed is shed by previous time-step trailing edge vortex panel, second row

is known since corresponds to the convected previous time-step wake panel row where the Kutta condition was resolved. Therefore, at the rising of time the rows successive to the wake panel row, closest to the trailing edge are known.

This time stepping methodology may be continued at every single time step in which vortex wake is moved by the local velocity. Thus, unsteady phenomenon like wake rollup may be simulated.

At this point, it is clear that in order to model the wake the following steps are taken: define the wake separation line which coincides with the trailing edge and is treated as the first section of the wake; identify which patch a wake separates from, the side of the patch which is parallel to the separation line and the row of panels within the patch that the wake separates from. As described by Katz and Plotkin [61], this row of wake panels have a length dimension in the streamwise direction corresponding to

$$c_w \, |U_\infty| \, \cdot t$$

where the value of c_w is typically chosen to be $0.2 \div 0.3$. In the present implementation, a value of 0.25 was found to be adequate. This reduced value of c_w is a result of the use of vortex rings to model the wake vorticity rather than higher order vorticity distributions.

In this sense, from a numerical point of view, observe the importance of the distance and relative angle to the trailing edge. In fact, the wake vortex location should be aligned with the wing trailing edge and be placed closer to the latest position of the trailing edge. Therefore, the doublet when placed in the time interval introduces an approximation that underestimates the induced velocity when compared to the continuous wake vortex sheet result. This is so, since the distance of the continuous wake from the trailing edge during the time interval is a zero distance whereas the distance of an

equivalent panel placed in the time interval is not zero. Therefore, to correct this wake discretization error it is necessary to place the wake panel with a value of length dimension in the streamwise direction chosen to be $0.2 \div 0.3$. Instead, for the successive rows of wake panels, the value of c_w is chosen to be 1: the length in the streamwise direction of $|U_\infty| \cdot t$.

Let N_{ts} be the time step in which one wishes to compute the solution and M_W the number of wake panels generated at each time step. Equations (2.78) and (2.79) are corrected in this way:

$$\sum_{K=1}^{N_B} A^d_{JK}\mu_K = \sum_{K=1}^{N_B} B^d_{JK}\sigma_K - \sum_{I=1}^{N_{ts}-1}\sum_{L=1}^{M_W} C^d_{JIL}\mu^w_{IL} \qquad (J = 1, ..., N^d_B) \tag{2.82}$$

$$\sum_{K=1}^{N_B} A^n_{JK}\mu_K = \sum_{K=1}^{N_B} B^n_{JK}\sigma_K - \sum_{I=1}^{N_{ts}-1}\sum_{L=1}^{M_W} C^n_{JIL}\mu^w_{IL} - \underline{n}_J \cdot (\underline{U} - \underline{U}_\infty)_J \qquad (J = 1, ..., N^n_B) \tag{2.83}$$

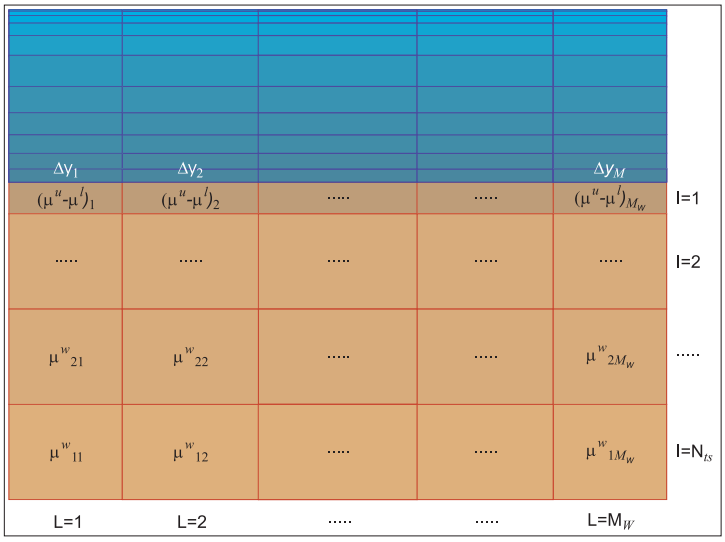

Figure 2.13: references for the indices of the wake panels.

Clearly, equations (2.82) and (2.83) are valid for any choice of N_{ts}, supposing the solution is computed in all below $N_{ts}-1$ time steps; particularly, equations (2.82) and (2.83) are equal to equations (2.78) and (2.79) when $N_{ts}=1$, respectively (figure 2.13).

The wake can be rigid, flexible or a combination of the two. If the wake is flexible, it is deformed at each time step by the local velocity induced by the presence of all the bodies and wakes being modeled therefore it is necessary to compute the velocity field into the grid points and/or control points of the wake panels and to deform these panels so that equation equations (2.80) are fulfilled correctly. In the case of rigid wake, the problem is linearized by the fact that the wake is imposed and thus the flow field can not influence the wake.

So far the wake modeling is only characterized by using of common wake panels. In the next chapter, it is going to be shown how the wake may be modeled by means of three dimensional singularity point vortex which will be really generated by the panels wake.

2.3.3 Computation of velocities and forces

For the computation of the total velocity in any point P outside the body, rewrite equation (2.56) in discrete term:

$$\underline{U}(P)=\underline{U}_{\infty}(P)-\sum_{K=1}^{N_B}\underline{U}_K^{\mu}\mu_K-\sum_{K=1}^{N_B}\underline{U}_K^{\mu}\mu_L^{w}+\sum_{K=1}^{N_B}\underline{U}_K^{\sigma}\sigma_K \tag{2.84}$$

where the coefficients

$$\underline{U}_K^{\sigma}=\int\int_{panel\ K}\underline{\nabla}\frac{1}{r}dS \quad ; \quad \underline{U}_K^{\mu}=\int\int_{panel\ K}\underline{\nabla}\left(\underline{n}\cdot\underline{\nabla}\frac{1}{r}\right)dS \tag{2.85}$$

have the same physical significance of the corresponding coefficients of equation (2.65) and (2.66).

In the same way, one can start by equation (2.57) for velocity calculation in every single point lying on the body surfaces, particularly in the grid points and control points. However, for the points lying on the surfaces, it is most advantageous to use equation (2.58) which, for the computation of the tangential components of velocity perturbation, may be applied to an explicative scheme, as follow:

$$u_{t1} = \frac{\mu(J_3) - \mu(J_1)}{d_1 + d_3} \quad ; \quad u_{t2} = \frac{\mu(J_4) - \mu(J_2)}{d_2 + d_4} \tag{2.86}$$

In the case of a Neumann boundary condition (see equation 2.59), the tan-

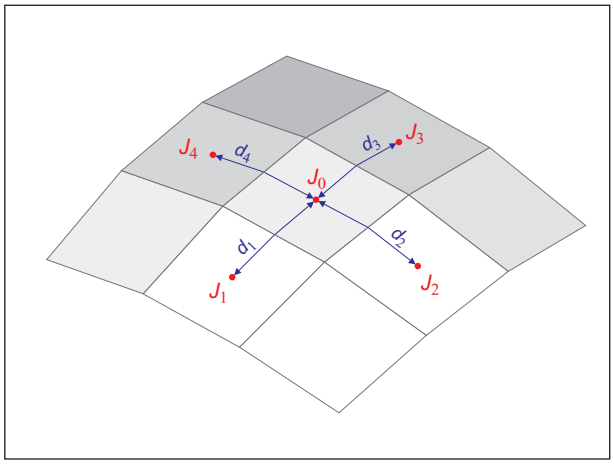

Figure 2.14: schematization of the computation of the velocity perturbation components.

gential component of velocity perturbation becomes:

$$u_{t1} = \pm\frac{(\mu(J_3) - \mu(J_1))/2}{d_1 + d_3} \quad ; \quad u_{t2} = \pm\frac{(\mu(J_4) - \mu(J_2))/2}{d_2 + d_4} \tag{2.87}$$

In reality, the panel distribution results difficultly so regular as illustrated in figure 2.14, therefore, in order to apply equation (2.58) it is necessary to use a more complex computational technique how, for example, building a function of doublet strength distribution on the basis of a large number of

control point into the round of the interest point:

$$\widehat{\mu} = f(\xi_i, \eta_i, \zeta_i, \mu_i) \quad (i = 1, ..., n) \tag{2.88}$$

with the purpose to compute the derivatives.

After the velocity computation over the surfaces, it is possible to compute the corresponding distribution of pressure or, alternatively, of the pressure coefficient:

$$p = p_\infty + \frac{1}{2}\rho_\infty(\underline{U}_\infty^2 - \underline{U}^2) - \rho_\infty \frac{\mu(t) - \mu(t - \Delta t)}{\Delta t} \tag{2.89}$$

$$C_p = 1 - \frac{U^2}{U_\infty^2} + \frac{\mu(t) - \mu(t - \Delta t)}{\Delta t}\frac{2}{U_\infty^2} \tag{2.90}$$

thus, the force acting on every body:

$$\sum_{J=1}^{N_B} p_J \underline{n} S_J = \underline{F} \tag{2.91}$$

2.4 The vorton method for wake

The wake problem was analyzed by several authors. In particular way, Helmholtz analyzed the problem of two-dimensional body submerged in a flow field with the presence of a wake (called Helmholtz wake) behind the body whereas Von-Kármán studied the formation of vortices (called Kármán vortices) from a cylinder [50]. The goal of this section is to present and analyze a new vortex method as a tool for the direct numerical simulation of unsteady, inviscid and incompressible flows and, particularly, of vorticity localized on the thin wake regions. This new method is the vorton method, also called vortex particle method. The wake is a vorticity region which may be discretized in several ways. In panel methods, as already shown, the wake

is discretized into panels. In the present method, the wake is discretized into vortons.

2.4.1 The vorton method

To present this technique, consider a vorticity region and let V be the volume of this region. Since vortex methods are based on the discretization of the vorticity domain, consider a generic uniform grid taken as a set of cubes of volume h^3. A vorton, also called vortex particle, is simply a three-dimensional point vortex $\underline{\alpha}_p$ equal to the vorticity multiplied by h^3, according to Cottet and Koumoutsakos [23]. This vortex element may be expressed as

$$\underline{\alpha}_p(x, y, z, t) \;=\; \alpha_{x_p}(t)\underline{i} \;+\; \alpha_{y_p}(t)\underline{j} \;+\; \alpha_{z_p}(t)\underline{k} \tag{2.92}$$

where $\alpha_{x_p}(t)$, $\alpha_{y_p}(t)$ and $\alpha_{x_p}(t)$ represent the scalar component of $\underline{\alpha}_p$, at a given time, along the x, y and z directions, respectively. In figure 2.15, the equivalence between a vorton and a simple vorticity region of vorticity (vortex tube with constant section area) is represented. Clearly, a vortex tube may be also discretized into so many vortons: as described by Winckelmans and Leonard [62], a vorton may be thought of a small section of a vortex tube.

The vector potential for this element is a solution of Poisson's equation $\nabla^2\underline{\Psi} = -\underline{\omega}$. The solution of Poisson's equation is given by equation (A.9) which is an integral over the volume of vorticity. According to Strickland et al. [56][55], the vector potential is so given by

$$\underline{\Psi}_p(\underline{r}, t) \;=\; \frac{\underline{\alpha}_p(\underline{r}, t)}{4\pi|\underline{r}|} \tag{2.93}$$

where $\underline{r}$ is the distance from the vorton to the point of evaluation. Observe that above equation is singular for $\underline{r} = 0$. This singularity may lead to very large values when $|\underline{r}|$ approaches zero, therefore a core-function ξ_ψ is

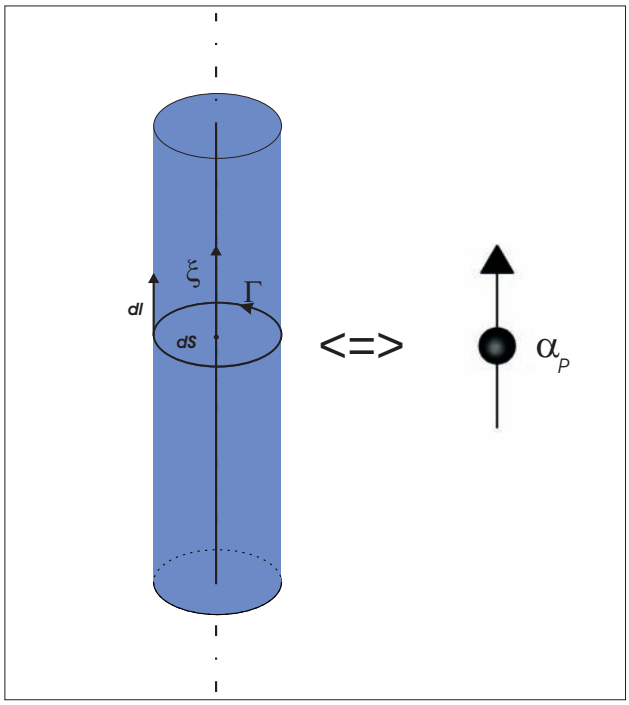

Figure 2.15: vortex tube and its corresponding vorton.

necessary to regularize the vector potential. Let η and r_η be the core-radius associated with the vorton and the ratio between the absolute distance of the evaluation point and the core-radius ($r_\eta = |r|/\eta$). The core-function ξ_ψ is so that, when $r_\eta < 1$, the vector potential decays linearly to zero.

The velocity field induced by a single vorton is given by the curl of the vector potential:

$$\underline{U}_{\Psi_p}(\underline{r}, t) = \underline{\nabla} \times \underline{\Psi}_p(\underline{r}, t) \tag{2.94}$$

Therefore, a vorton is a singularity element with the velocity magnitude that decays as $1/r^2$, see figure 2.16. Since $\underline{\Psi}_p$ is a solution of Poisson's equation, the velocity field due to the single vorton is rotational and solenoidal everywhere. As for the vector potential, the velocity results singular for $\underline{r} = 0$. Introducing a core function ξ_U as similarly done with the vector potential, this core function forces the velocity to decay linearly to zero when $r_\eta < 1$,

as illustrated in figure 2.16.

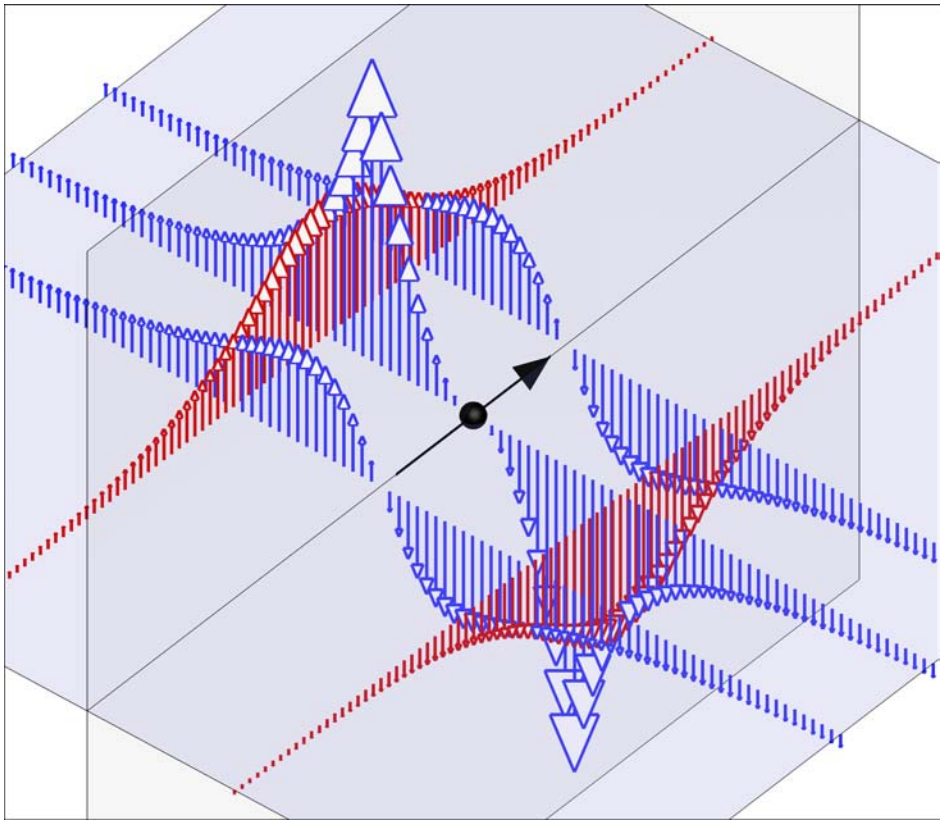

Figure 2.16: flow field induced by a vorton.

Note that a vorton results different from a two-dimensional vortex point. In fact, a 2D vortex is a solution of the Laplace's equation $\nabla^2\phi = 0$, where $\underline{U} = \underline{\nabla}\phi$ is irrotational by definition. Therefore, it is a singularity element with only a tangential velocity component whose magnitude decays as $1/r$, being $\underline{\nabla}\phi = -\underline{\Gamma}/(2\pi r)$ as illustrated in figure 2.17.

Moreover, the vorton evolution is governed by the vorticity evolution equation (1.28), therefore every single vorton is convected by the local velocity and strained by the local velocity gradient (stretching term in the vorticity evolution equation).

In order to approximate the exact initial vorticity field as accurately as

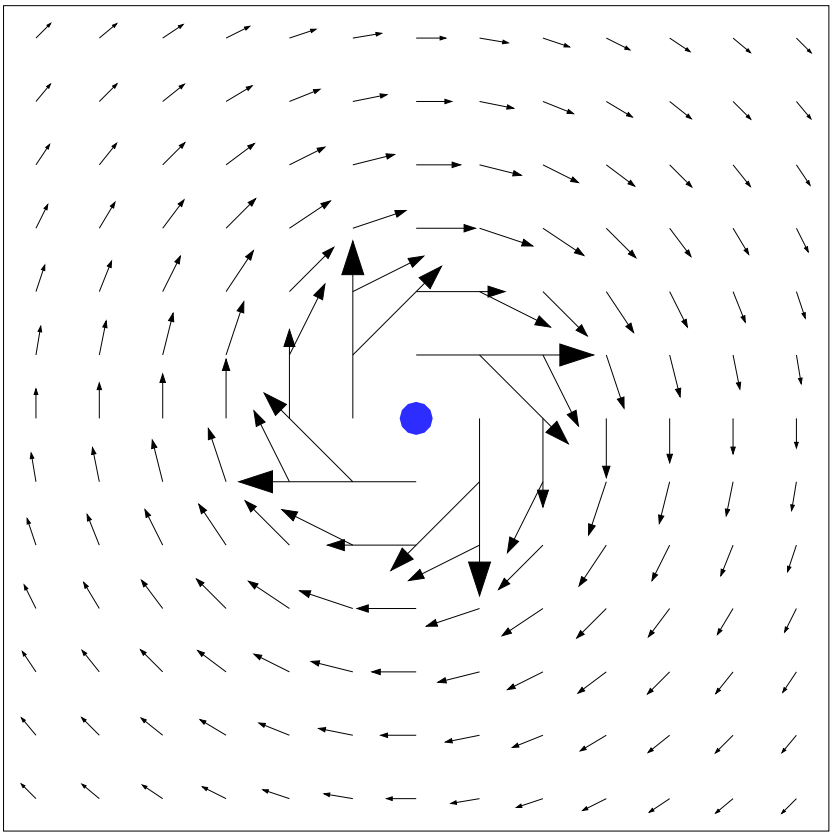

Figure 2.17: flow field induced by a two-dimensional vortex.

possible, now it is described the way to initialize the vortons. For the purpose, begin by considering the vorticity region of interest, which is the thin wake trailing the body surfaces. As shown in the previous chapter, this may be equivalently represented using equivalent doublet sheets and vortex rings. Thus, the problem is how to convert the wake commonly represented using vortex rings or equivalent doublet panels into the vortons, or also it is to be understood how to assign the strength to the vortons in order to represent the vorticity region correctly by means of vortons. According to Willis [60], the following steps are taken:

1. determine the equivalent vortex representation for every single doublet

panel to be converted to vortons;

2. fix the number of vortons to be generated from every single panel;

3. divide the panel into equal area segments.

Therefore, the vorton is computed by integrating the strength of the vortex line surrounding the panel area segment

$$\underline{\alpha}_p(\underline{r},t) = \int \Gamma(t)\underline{ds} \tag{2.95}$$

In the vorton method, the vorticity is replaced by a set of vortons and therefore the vorticity field is approximated as the linear combination of the vorticities represented by the vortons, as follows

$$\underline{\omega}(\underline{r},t) \;=\; \sum_P \underline{\alpha}_p(\underline{r},t) \tag{2.96}$$

as shown by Winckelmans and Leonard [62], Willis et al. [60][61], Lebental [35], Alkemade et al [3], Voutsinas et al. [59], Chatelain et al. [20], Aksman and Novikov and Orszag [2], Park and Kim [49], Eldredge [28], Chatelain and Leonard [21], Voutsinas et al. [48], Spalart [53], Cottet and Koumoutsakos [23].

The velocity field $\underline{U}_\Psi(\underline{r},t)$ is taken as the curl of the streamfunction which solves the Poisson's equation

$$\nabla^2\underline{\Psi}(\underline{r},t) \;=\; -\,\underline{\omega}(\underline{r},t) \tag{2.97}$$

Recalling that the Green's function $G(\underline{r},\underline{r}')$ for $\nabla^2 G = \delta(r,r')$ in unbounded domain is $G(\underline{r},\underline{r}') = -1/(4\pi|\underline{r}-\underline{r}'|)$ (as shown in section A.1) and according to equation (2.93), the vector potential is the summation over the vector potential of all the vortons in the domain:

$$\underline{\Psi}(\underline{r},t) = \frac{1}{4\pi}\sum_p \frac{\underline{\alpha}_p(\underline{r},t)}{|\underline{r}-\underline{r}_p(t)|} \tag{2.98}$$

The velocity vector is obtained as the curl of the streamfunction $\underline{\Psi}$, as follow

$$\underline{U}_{\Psi}(\underline{r},t) \;=\; \underline{\nabla}\times\underline{\Psi}(\underline{r},t) \;=\; \frac{1}{4\pi}\sum_{p}\frac{\left[\underline{r}-\underline{r}_p(t)\right]\times\underline{\alpha}_p(\underline{r},t)}{|\underline{r}-\underline{r}_p(t)|^3} \tag{2.99}$$

where the velocity components are:

$$u_{_{\psi}} \;=\frac{1}{4\pi}\sum_{p}\frac{1}{|\underline{r}-\underline{r}_p|^3}\left[(z-z_p)\alpha_{y_p}-(y-y_p)\alpha_{z_p}\right] \tag{2.100}$$

$$v_{_{\psi}} \;=\frac{1}{4\pi}\sum_{p}\frac{1}{|\underline{r}-\underline{r}_p|^3}\left[(x-x_p)\alpha_{z_p}-(z-z_p)\alpha_{x_p}\right] \tag{2.101}$$

$$w_{_{\psi}} \;=\frac{1}{4\pi}\sum_{p}\frac{1}{|\underline{r}-\underline{r}_p|^3}\left[(y-y_p)\alpha_{x_p}-(x-x_p)\alpha_{y_p}\right] \tag{2.102}$$

Therefore, the rotational velocity field may be constructed by means of a linear combination of a set of basis velocity fields, every one of which is induced by a vorton. Clearly, the implementation results very simple and easy.

Similarly, the gradient of the velocity used for the vorticity stretching in the vorticity evolution equation results:

$$\underline{\nabla}\;\underline{U}_{\Psi}(\underline{r},t)=\frac{1}{4\pi}\sum_{p}\underline{\nabla}\left[\frac{(\underline{r}-\underline{r}_p)\times\underline{\alpha}_p(\underline{r},t)}{|\underline{r}-\underline{r}_p|^3}\right] \tag{2.103}$$

Regarding the vorton evolution, this is characterized by a change of strength and position in time. Each vorton displacement derives from the velocity field caused by the other vortex particle [3].

Now, in the Lagrangian representation, the position evolution of a single vorton is governed by the velocity vector, as follow

$$\frac{D}{Dt}\underline{r}_p(t)=\underline{U}_p(\underline{r}_p(t),t) \tag{2.104}$$

As for the evolution of the particle strength, the biggest difference between two-dimensional and three-dimensional vortex method is the existence of the stretching term. In two-dimensional case, since the vorticity direction

is perpendicular to the velocity direction, this term always goes to zero. In three-dimensional case, the evolution of vorticity is governed by the stretching term which changes the orientation of the vorticity as well as its value for every timestep. Vorton deformation is derived from the Helmholtz equation, therefore in Lagrangian approach follow

$$\frac{D}{Dt}\underline{\alpha}_p(\underline{r},t) = \underline{\alpha}_p \cdot \underline{\nabla}\ \underline{U}_p(\underline{r}_p(t),t) \tag{2.105}$$

At this point, the equations of the evolution of the vortons are discretized using a forward Euler scheme. First, the position of the vorton is updated,

$$\underline{r}(t+1) \ = \ \underline{r}(t) \ + \ \underline{U}_p(\underline{r}(t),t)\ \Delta t \tag{2.106}$$

Second, the strength of the particle is updated,

$$\underline{\alpha}_p(t+1) \ = \ \underline{\alpha}_p(t) \ + \underline{\alpha}_p(t) \cdot \underline{\nabla U}_p(\underline{r}(t),t)\ \Delta t \tag{2.107}$$

Clearly, the use of higher order time stepping method will be beneficial in increasing solution accuracy.

A system of vortons can, in turn, be used to model body surfaces, container boundaries, free-surfaces, internal flows, jet flows, turbulent internal flow, and wakes in unsteady three-dimensional flow fields.

In the present work, vortons will be used to model wakes in unsteady, inviscid and incompressible flows because these vortex elements are more easily manipulated than the traditional wake sheet representation. In fact, panel methods presents the need to compute the induction of the flow field due to four segments of each doublet panel whereas the vorton discretization offers the possibility to compute the induction due only to a point for every single vorton. Hence, the vorton method results to be more attractive because it has also the advantage that the three-dimensional point vortexes are somehow independent as they do not necessarily belong to a specific wake panel for all times.

To summarize, the vorton method has been shown in order to solve Poisson's equation in the wake. Moreover, the two evolution equations of the position and strength of the vortex particles have been presented also. Now, it is necessary to compute the initial strength and position of the vortons when they are created in the wake. Before this, it is necessary to describe the wake model in detail.

2.4.2 Conversion of the wake panels to vortons

As seen in above chapter, the wake in a common panel method may be modeled by means of a distribution of doublets with a strength so that the Kutta condition at the trailing edge results fulfilled. Now, the goal is to describe the conversion of the wake panels to vortons for an unsteady wake model which consists of a distribution of panels and a distribution of vortons.

In the wake model with vortons, the wake is divided into two parts: a near wake and a far wake. As regards the near wake, close to the wing, the wake is modeled using a wake sheet slicing the domain. This buffer wake sheet imposes the prescribed potential jump in the normal direction across the wake sheet and this is used to account for the vorticity recently shed into the domain from the wing trailing edge. Regarding the far wake, this is represented using a distribution of vortons. This wake decomposition is presented in figure 2.18.

The buffer sheet is at least composed of two rows of panels trailing from the wing trailing edge. Closest to the trailing edge, the panels of the first row are unknown wake panels because initially have an unknown strength: their strength is determined by the Kutta condition. Instead, the panels of second row are known wake panels since correspond to the convected previous time-step unknown wake panels where the Kutta condition was resolved at

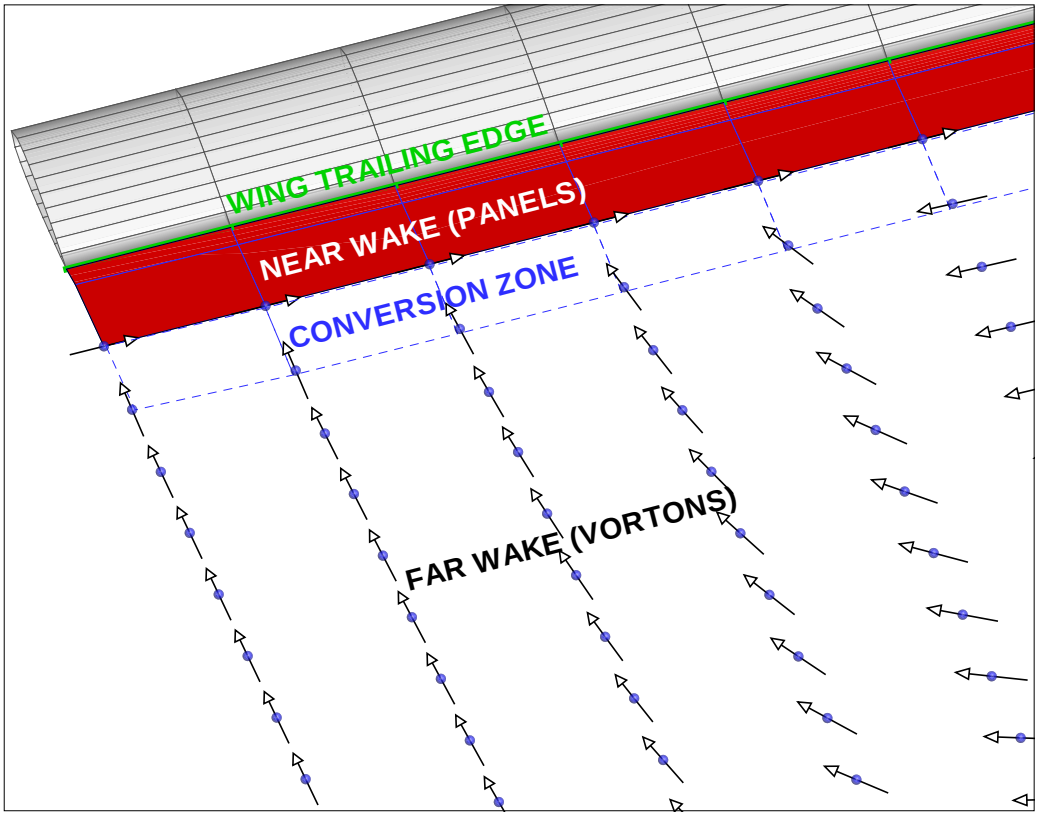

Figure 2.18: wake model with vortons.

$t = t - \Delta t$.

As described for the unsteady panel wake, also in this case the first row of wake panels has a length dimension in the streamwise direction corresponding to $c_w|U_G| \cdot t$ where the value of c_w is chosen to be 0.25. The panels of the second row have a known strength corresponding to the previous timestep trailing edge potential jump with a value of c_w is chosen to be 1.

At each time step, the previous time-step second row of wake panels is converted into vortons.

Similarly to the panel wake model, the wakes will be constructed gradually at every time step generating a new row of buffer panels closest to the trailing edge and, furthermore, vortex particles will be created as the near

parts of the wakes evolve.

An important point that must be considered for the conversion of the dipole wake sheet to vortons, is the equivalence between the change in doublet strength along the surface and vorticity oriented in the surface tangential direction normal to the doublet gradient (see section 2.1). In the particular case of constant doublet panels, the vortex analogue is a vortex ring around the perimeter of the given panel: hence, the strength of the vortex line segment between two adjacent constant strength panels is merely the difference in doublet strengths. Therefore, the vorton is computed by integrating the strength of the vortex line segments between adjacent panels depending on chosen model.

To summarize, the conversion is done in the following way [35]:

- the corners of each near panel of the second row are convected with the local velocity;
- the location and strength of vortons are calculated according to the model used;
- the strength of the vortex line between the near and the far wake is updated.

The adopted model is called DIAS model. It is characterized by the conversion of the wake panels to vortons localized on the vertexes of the transformed panels.

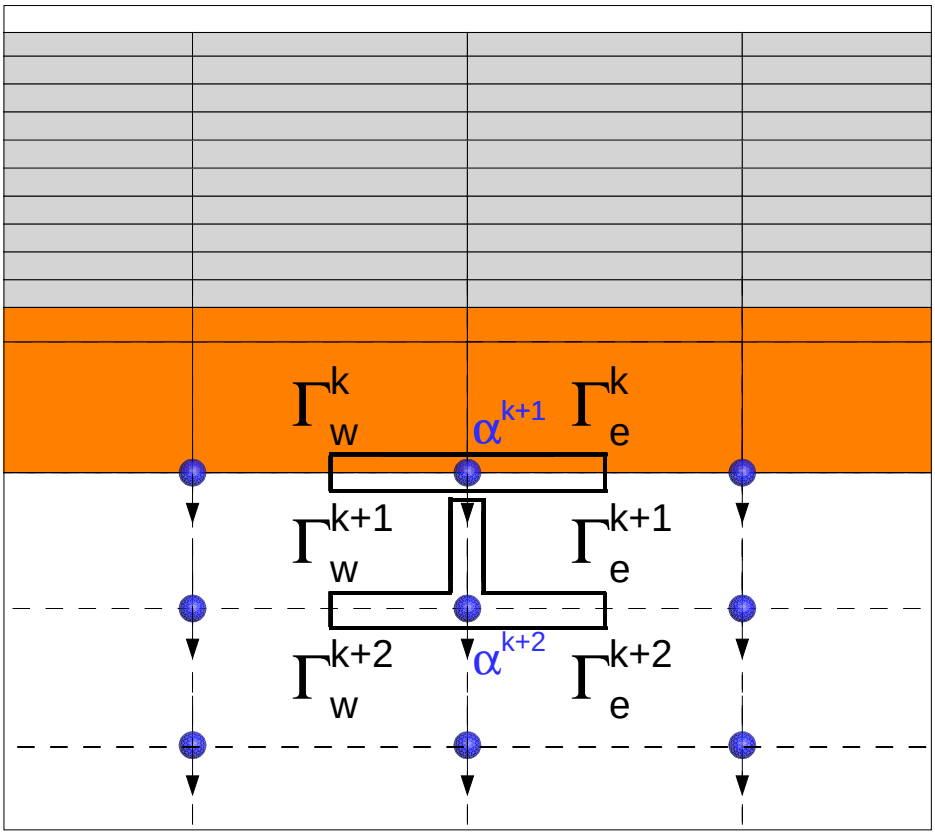

Figure 2.19: DIAS vorton wake model - the mechanism of vortex particles generation.

With the notation of figure 2.19 the vortons have the following strengths

$$\underline{\alpha}^{k+1} = \quad t_{3w}^{k}(\Gamma_{w}^{k} - \Gamma_{w}^{k+1}) \quad + \quad t_{3e}^{k}(\Gamma_{e}^{k} - \Gamma_{e}^{k+1}) \tag{2.108}$$

$$\underline{\alpha}^{k+2} = \quad t_{2E}^{k+1}(\Gamma_{E}^{k+1} - \Gamma_{W}^{k+1}) \quad +0.5 \quad t_{3W}^{k+1}(\Gamma_{W}^{k+1} - \Gamma_{W}^{k+2}) + \\ +0.5 \quad t_{3E}^{k+2}(\Gamma_{E}^{k+1} - \Gamma_{E}^{k+2}) \tag{2.109}$$

Chapter 3

INVISCID FLOWS OF PARTICLES

In the previous chapter it has been shown that in certain conditions the wake can be modeled with vortons instead of panels. Even if the behavior of vortons is less troublesome than that of the wake panels when dealing with wake-body interactions, as shown in Nola's work [64], there is still the chance that vortons can enter into the bodies. This is a numerical error, then it is required to indicate what are the sources of this error, what are the possible countermeasures and what are their advantages and disadvantages. In simple words high order integration schemes with fine paneling and fine time-stepping give the best accuracy results but they cost greater computational time than low order, coarse codes; however during the initial design phases fast codes are more rewarding. Due to this, quadrangular panel methods adopting a step-by-step time integration scheme are amongst the most widespread panel methods. Moreover, since changing the time integration scheme into an existing panel method means a major re-organization of the code and since the time step is often decided by other requirements than

the trajectory integration accuracy, then this chapter is orientated towards the ascertainment of this error and the possible countermeasures, excluded a time step modification and a major re-organization of the code. In order to understand what could happen to vortons in a 3D flow it has been created from scratch a simple 2D unsteady Douglas-Neumann panel method with two different time integration schemes which allowed a qualitative evaluation of the problem. In particular in this chapter are shown what are the advantages and disadvantages of an explicit Euler, or step-by-step (from now on FWE), time integration scheme with an elemental flow of passive scalar particles, compared to a predictor-corrector time integration scheme (also known as Heun method or as 2^{nd} order Runge-Kutta, from now on RK2). Since choosing to move the particles or the body first it is part of the time integration scheme itself and since this choice just implies a different starting error it has been chosen to move the particles first into the 2D code, which has been a natural way to develop it at the beginning.

An irrotational and inviscid flow induced by a non lifting 2D circle moving at constant speed has a well known analytical solution for the velocity potential ϕ and the stream function $\underline{\Psi}$. Thus this body is often the subject of test cases, as done here. Precisely ψ is just scalar in a 2D case. Unfortunately it has not been found any bibliographical reference about an analytical function $\underline{r}(t)$ of a particle moving into this flow to compare directly to a numerical trajectory computed with a FWE time integration scheme. Therefore it has been developed the Appendix B to know what is the final position of a particle in this flow, when the circle has arrived far downstream. This appendix has been useful in understanding if the results obtained from the 2D Douglas-Neumann panel method with the RK2 scheme are a good reference to compare with analogous results obtained with the FWE scheme.

3.1 The sources of numerical error into panel methods

There are errors due to numerical approximations done into panel methods, which must be kept into reasonable bounds, most often it is sought for convergence when a discretized independent variable approaches zero. The first source of error is the spatial discretization of the model. Panel methods are a design tool useful to create objects of aeronautical (and many others) interest, therefore the panel shape must be coherent with a given representation of the object itself. As an example it is not correct to use parabolic panels to discretize the body and then the wake is discretized with a simple quadrangular discretization: in any case rules the error due to the coarsest spatial discretization, it is in any case $\propto \Delta S$, where ΔS is the panel area. If the parabolic discretization is applied everywhere then the error is $\propto \Delta S^2$.

There is another source of error to account. As already explained into §2.3 and in [15] there is a non linearity into the computation of the wake, which can be reduced or not if it is introduced an iteration during the computation of its singularity strength. But there is also another problem. When it is expected that the wake interacts with other bodies downstream, as already shown in Nola's work [64], a panel formulation of the wake is more troublesome than a vorton formulation. When using vortons, as already shown in §2.4 arises a new error source due to the core radius. If it is not strictly required using vortons then choosing between a vorton wake and a panel wake means to trade-off between a faster or a more accurate way to calculate it.

If it is done the hypothesis that the object is not discretized and that it is known its exact velocity field and wake singularity distribution at each instant then it is possible to assume that the error bound to the spatial discretization

is null. However it is still standing an error bonded to the discretization of the time Δt. In this case, if it is desired to compute the trajectory of a particle, there is a local error approximation $\epsilon_L \propto (U_\infty \Delta t)^{p+1}$. Actually the power p depends upon the time integration scheme, as an example $p = 1$ if the integration scheme is a FWE. Another example is the RK2 time integration scheme, about which it is known that $p = 2$ [71]. So far have been listed other error sources, which come together with this last one just listed, therefore it is desirable to choose a coherent time integration scheme, acting differently could result into wasted effort of code programming.

Choosing a coherent time integration scheme for an unsteady panel method means also to make a coherent choice about moving first the fluid particles or the moving solid objects. Until the particles are passive, moving first them or the objects just means creating a different starting error, once it is done the first movement the sequence is the same and then the approximation error is comparable. If it is assumed that there is no wake and the particle is assumed to be passive, the approximation error of its path can be considered a linear sum of the approximation errors of the adopted time integration scheme and that of panel model.

However it is required to remove the assumption of passive fluid particle, since the interest is towards the interaction between the wake and bodies. Doing this means to introduce another non linearity bound to the wake because the vortons and the bodies have mutual influence. Therefore the approximation error is still a function of the approximation errors of the adopted time integration scheme and that of panel model, but now this function is no more linear.

All these sources of error can bring a vorton to penetrate a body, in a way which is going to be shown in the next sections. Since this situation is

non physical when it is assumed the impermeability of the bodies, an in-out check is both a mean to control if the error has unacceptably grown and the first step to take when dealing with vortons.

Another way to control this error is to act over the sources, doing such things like reducing the time step Δt or the panel area ΔS, using high order panel models, but this is not cheap. Using an high order panel method in place of a low order one, like a panel method with quadrangular panels, means to accept a greater computational time and a more accurate programming. Since it has just been explained that the error induced by panel discretization and time step are connected through the vortons, in order to preserve the benefit of the better accuracy it is necessary to pay attention at the coherence between the panel method and the time integration scheme. This means that it is not possible to upgrade an existing panel method through small changes, if it is desired a more accurate panel method there is need for a major re-organization of the code.

Even if it is done everything it is required to achieve the better accuracy the time cost could not be affordable. Considering the case of a panel method used for initial design purposes, the time cost is not affordable because during an initial design phase it is required to execute the greatest number of operations in a given time, especially if during this phase it is working by comparisons. Fulfill more restrictive accuracy requirements is the target of a more advanced state of the design process, during which it is questionable the use of a panel method.

All these problems are interconnected and share being caused by the error of numerical integration. Thus they also exist in 2D cases, although there are some discounts, such as a direction of integration and an easier way to assign the Kutta condition. This means that it is at least possible to qualitatively

establish what errors can occur into a given 3D panel method using a simpler but still coherent with it 2D analysis.

In order to gain a better insight with particles behavior, it is now specified, once for all, that the analyses done into this chapter required a 2D Douglas-Neumann source panel method, a simple code created with Matlab, with two different time integration schemes, one is the FWE and the other one is a RK2, with particles moved before the body. The main subject is understanding how dealing with vortons since this is still an open problem, the details of the tests are reported into the next sections. It is needed understanding, at least qualitatively, if the number of penetrating vortons is limited or not. In a positive case it can be concluded that it is acceptable to delete a few vortons into a whole flow field without sensibly changing the accuracy of a 3D panel method if this models the bodies with quadrangular panels and the wake with vortons moved by a FWE time integration scheme.

3.2 The intersecting vortons problem

The intersecting vortons problem must be considered, because it is not due to a particular discretization, but to the discretization itself. It can be taken a simple 2D example, a vertical line of passive particles subject to a steady uniform flow with a velocity equal to $1m/s$, placed at $x = -6m$ from the origin, going towards a non moving, impermeable, non lifting cylinder centered with the axes origin, choosing a simple FWE time discretization and a $\Delta t = 1.458sec$. As it can be seen in figure (3.1d) some particles entered into the cylinder after some time-steps. This is an error since it has not been respected the condition of impermeability and worse, the wrong position feels a velocity induction which will not allow the particle to approach again the

true position within any reasonable tolerance. In figure (3.2) it is shown the same case, the only change done is the time step which has been divided by four.

This is of course a problem of numerical inaccuracy, and most often (but not always) can be solved adopting a smaller Δt. Now it is taken as an example the case shown in figure (3.3), where are considered some particles disposed along the y axis, the circle is moving with a velocity equal to $-1m/s$ in the x direction and with $-cos(t)$ law in the y direction, the time-step is still $\Delta t = 1.458sec$. As in the previous case the particles are incorporated by the circle. When the algorithm reaches the situation shown in figure (3.3d) the circle is incorporating some particles, and then computes the new position of the particles, as can be seen in figure (3.3e). In this figure it is clear that the position update done to an incorporated particle is wrong. In figure (3.4) it is shown the same case, the only change done is the time step which has been divided by four.

Using a smaller Δt is a possible solution, but it cannot be in general the solution because of some theoretical and practical problems. The first theoretical observation is due to the convergence property of the integration scheme. It is well known that it is possible to correlate the error of a convergent integration scheme and an infinitesimal integration step, a time step in this case. Usually the smaller is the Δt, the smaller is the error. But this is not always true and this is the first theoretical problem. Another theoretical problem is the following. Calculating a particle position in various time steps equals performing an integration over the time of a velocity function. Also the stability property depends upon the adopted discretization and the analyzed case, and since it is known that it is not always true that a scheme is stable with $\Delta t \to 0$ it is also explained this problem [69][70][71][72].

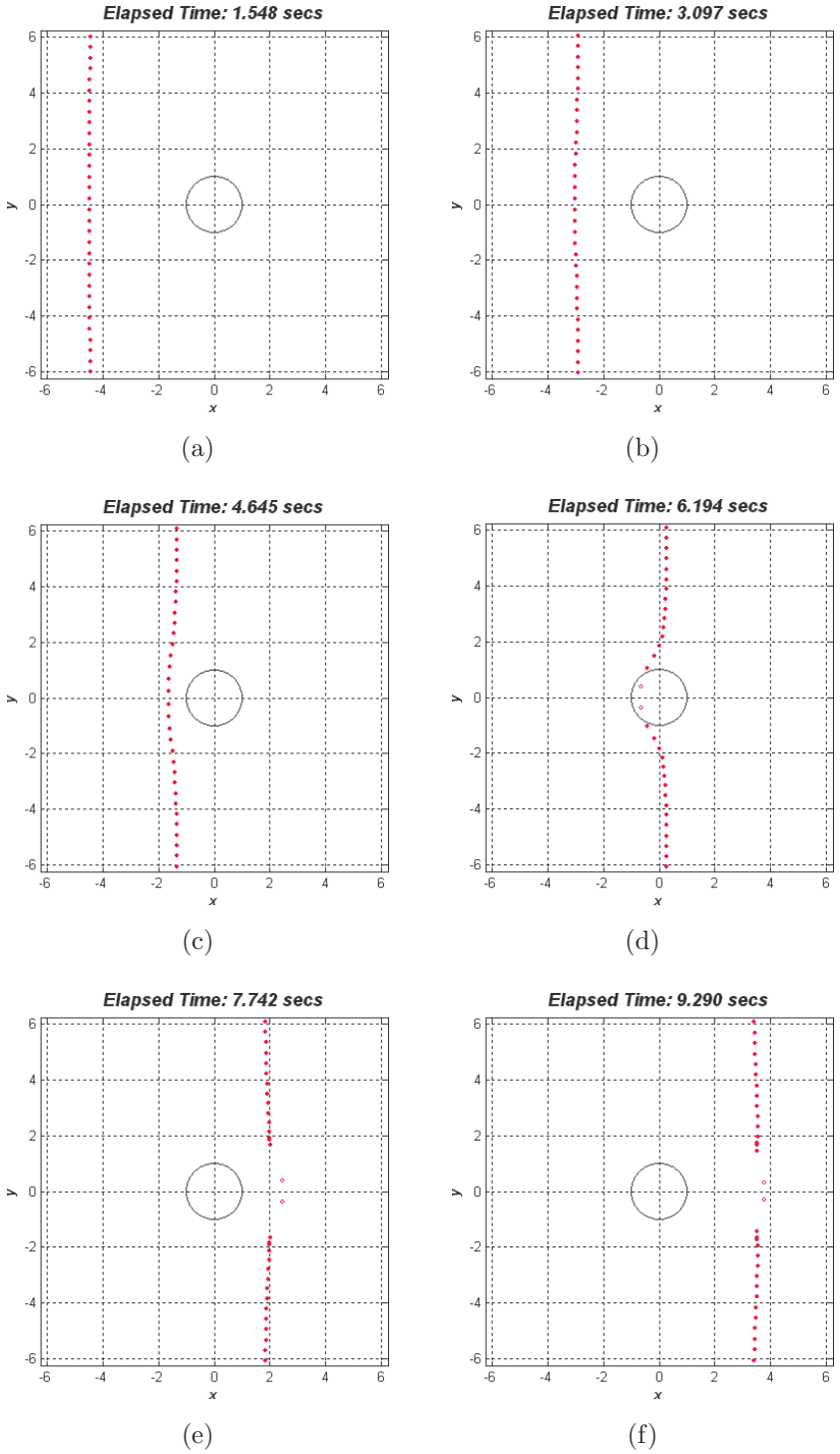

(a) (b) (c) (d) (e) (f)

Figure 3.1: 2D passive particles entering into a non lifting circle

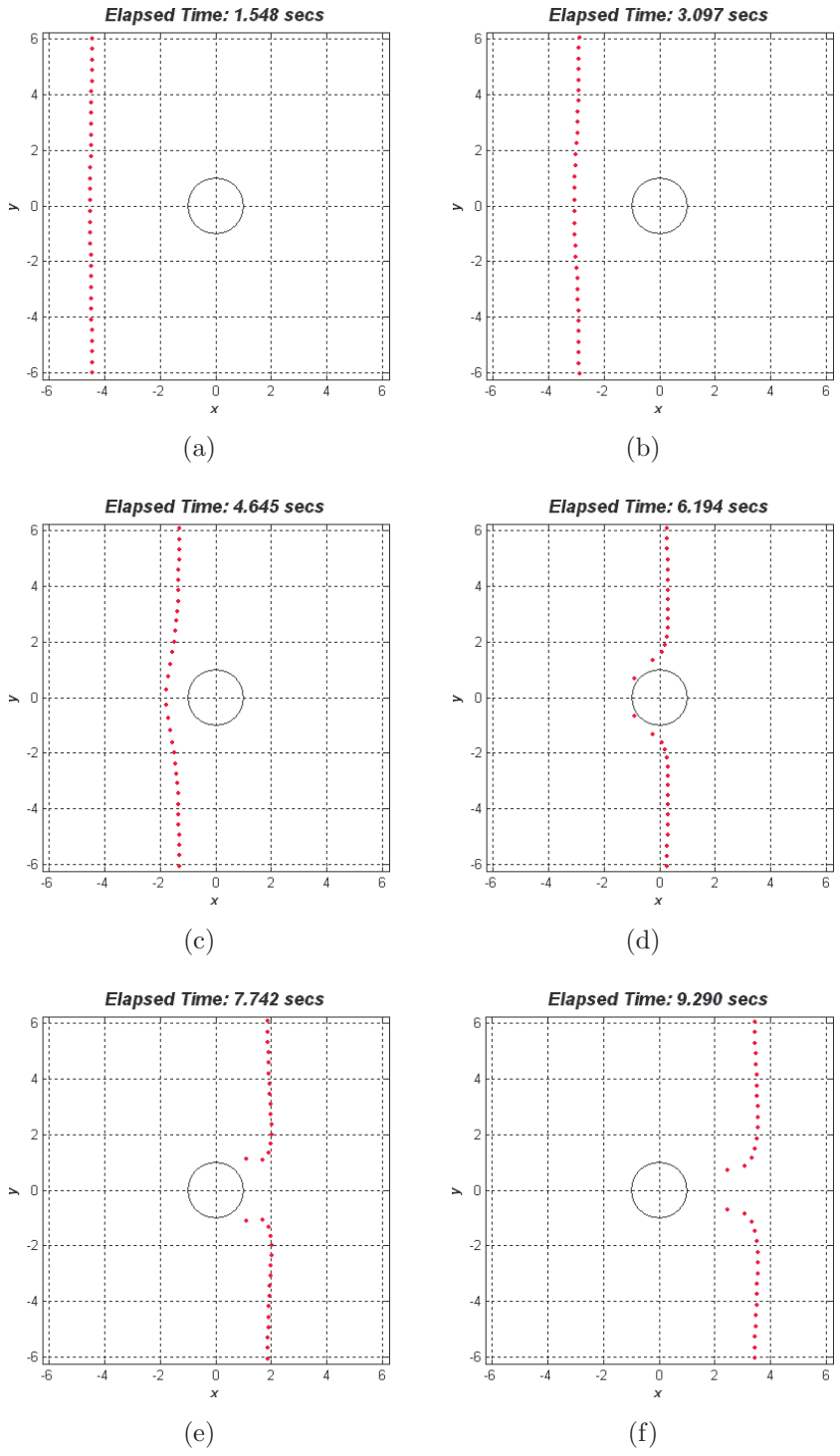

(a) (b) (c) (d) (e) (f)

Figure 3.2: 2D passive particles non-entering into a non lifting circle after a time-step reduction

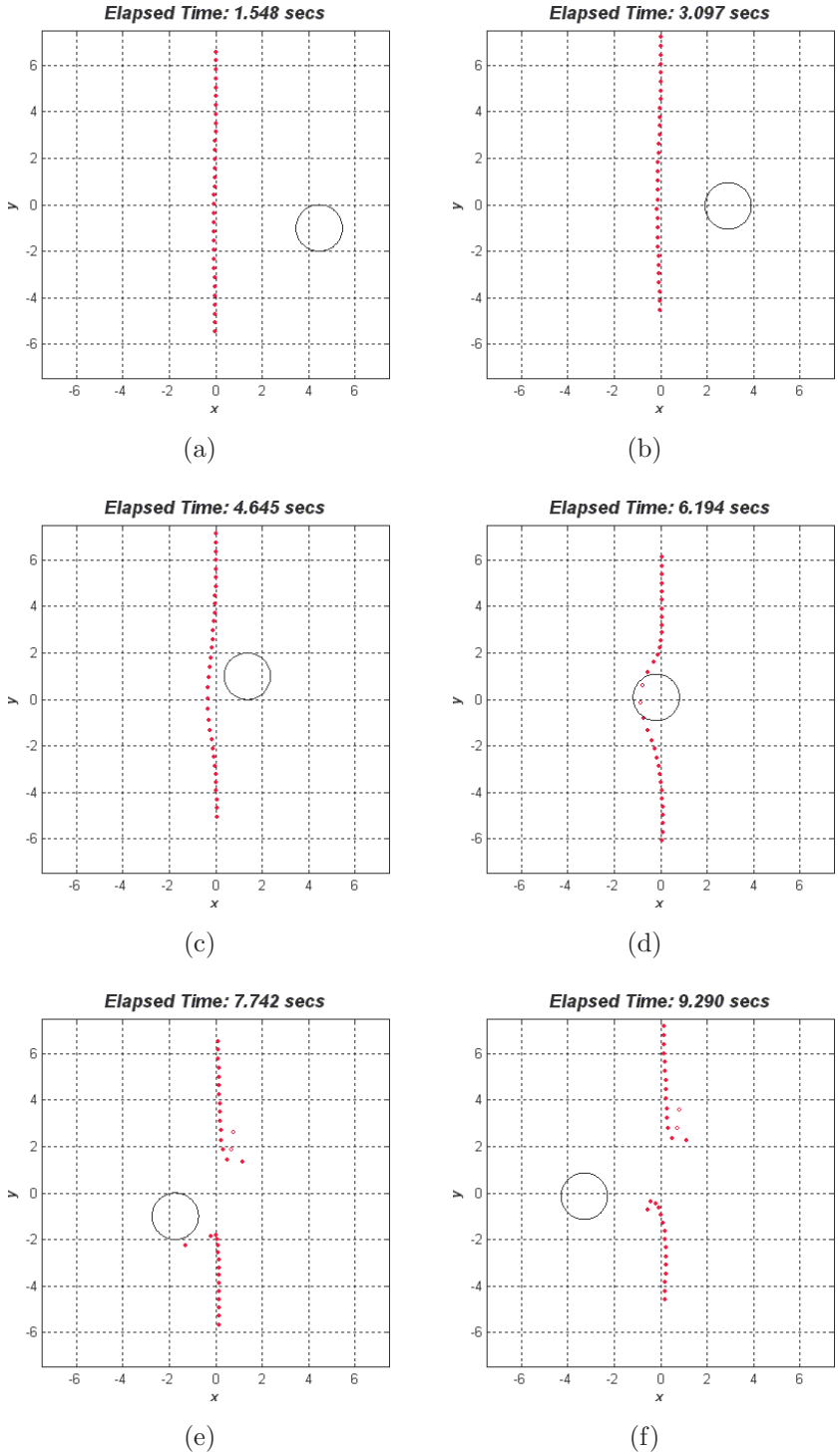

(a) (b) (c) (d) (e) (f)

Figure 3.3: 2D passive particles incorporated by an oscillating, non lifting circle.

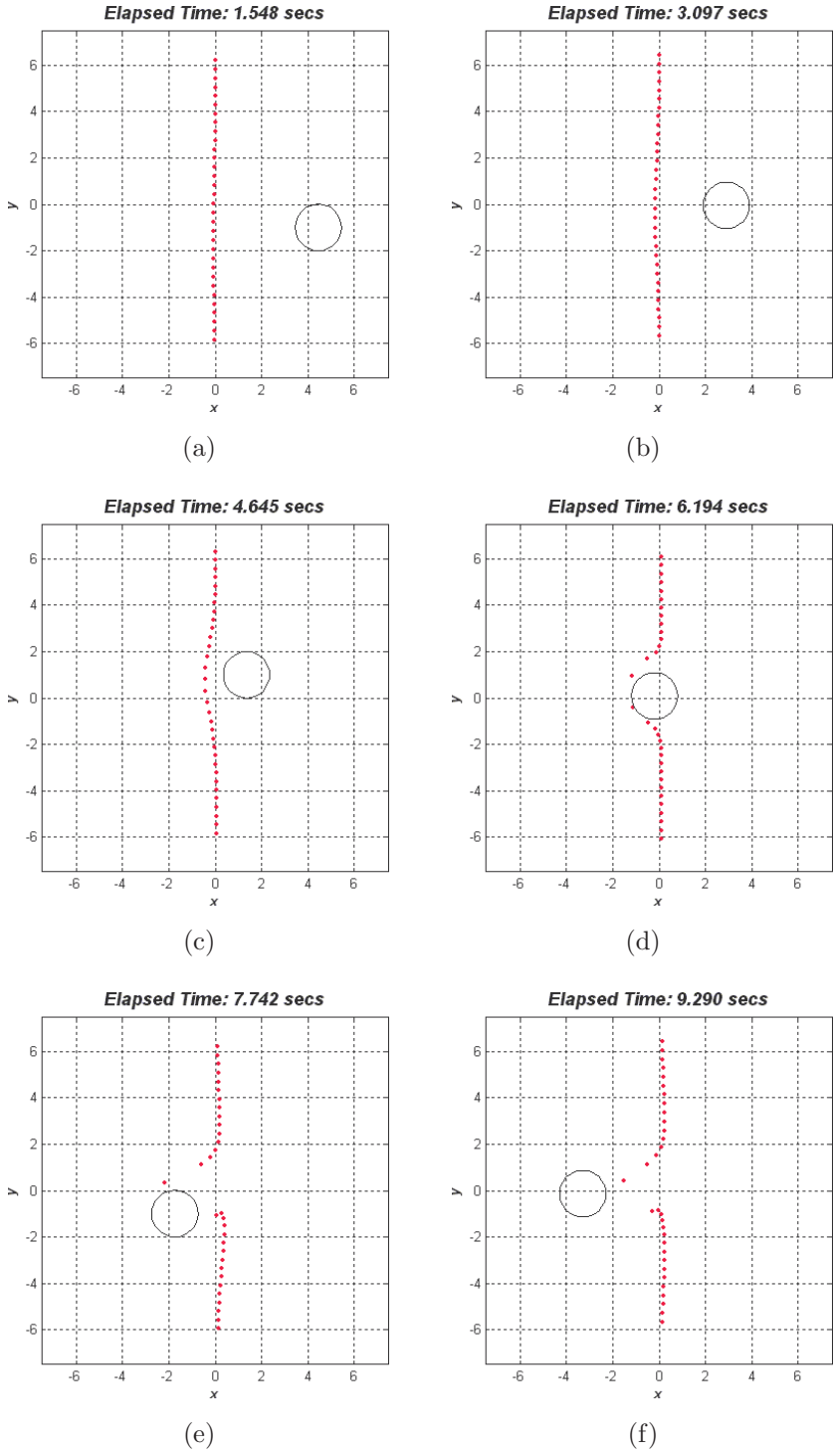

(a) (b) (c) (d) (e) (f)

Figure 3.4: 2D passive particles not incorporated by an oscillating, non lifting circle after a time-step reduction.

The practical problem is that sometimes the timestep is frozen by other requirements that fall outside the user's ones, or simply because the smaller is the timestep the bigger is the elaboration elapsed time, which could go beyond reasonable values.

This means that there are two ways to solve the problem of the intersecting vortons. The first solution, given the time-step, is to find a time discretization scheme which does not suffer the problem. The second solution is to create a warning mechanism which reacts with a countermeasure if the problem happens. The two solutions do not exclude each other, however, as written in the above section, the first solution needs an approach different from the upgrade of an existing code, therefore it is not going to be considered in this work.

3.3 The penetrating particle check

Creating a penetrating particle check means creating a simple mechanism to deal with particles. Whatever way it is dealing with particles the first step is avoiding them penetrating, or, if this is not possible, checking when they enter. Once it has been checked that the particle has entered it can be deemed appropriate to delete the particle, or to correct anyhow its trajectory, or, if it is not a passive particle, to somehow distribute or not the convected information. However, any decision is deemed the most appropriate cannot prescind from first checking if the particle has entered or not. This check mechanism has to fulfill the following requirements:

- Low computational time costs
- Simple implementation into Panel methods

In figure (3.5) it is shown an irregular, 2D body paneled with irregular panels. Full points represent the knots of the body, the emptied points represent the panel centroids. The only vector represented in figure implies that all the normal vectors of the panels must point outwards from the body.

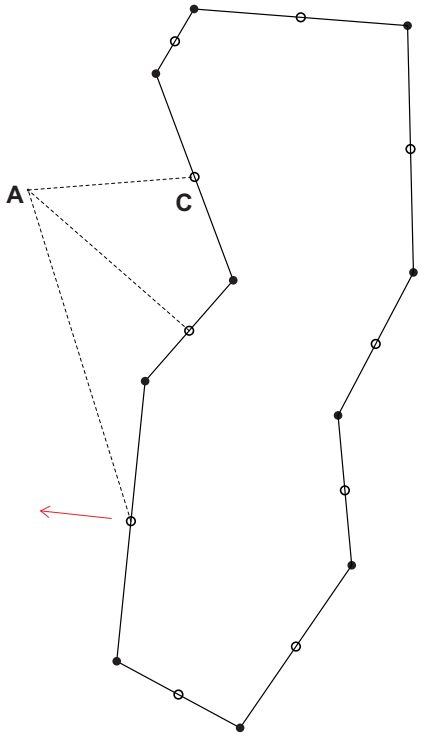

Figure 3.5: Irregular, 2D body paneled with irregular panels.

The penetrating particle check requires as input data the normal vector, the panel centroid and the list of adjacent panels per each panel and the coordinates of the point A, which is evaluated. To establish whether the point A is inside or outside it is evaluated the distance from every panel centroid (the dashed lines); once it is estimated which is the closest centroid, this point is named C and the panel which belongs to it is going to be used to do the inside-outside evaluation.

Thus, known the vector $\vec{CA}$, it is projected along the panel unit vector belonging to the same panel of the point C. If the result is positive, then the point A is outside the body (figure (3.6a)), otherwise this evaluation is repeated and crossed also considering the adjacent panels. If there is at least one panel giving an outside answer (figure (3.6b)), then the point is considered outside, otherwise it is inside (figure (3.6c)).

This type of evaluation is rudimental, therefore it should be used carefully, but it is really simple to implement into panel methods and its input data are all already available since they are created in previous calculations done by the main parts of a panel methods code.Once evaluated that the particle is inside, a possible countermeasure is to divide by two the main timestep creating a secondary timestep, update the particle position using the secondary timestep until the sum of the secondary timesteps has reached again the main timestep and re-check if the particle is still inside: in positive case, iterate, in negative case, the main timestep is restored. This approach has been used in the next section but it is anticipated that it is poor. Other two possible treatments of the penetrating particle are shown in figure (3.7), and will be considered in the next chapter.

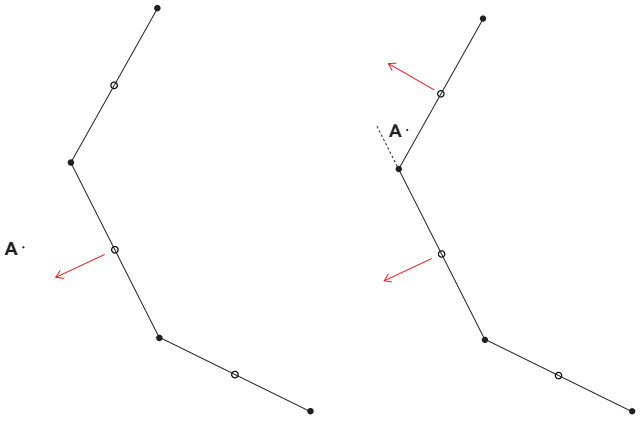

(a) Point A is outside

(b) Point A is outside after the cross check with the adjacent panels

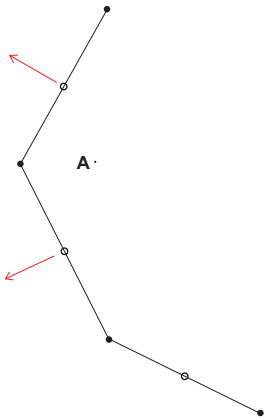

(c) Point A is inside

Figure 3.6: The penetrating particle check.

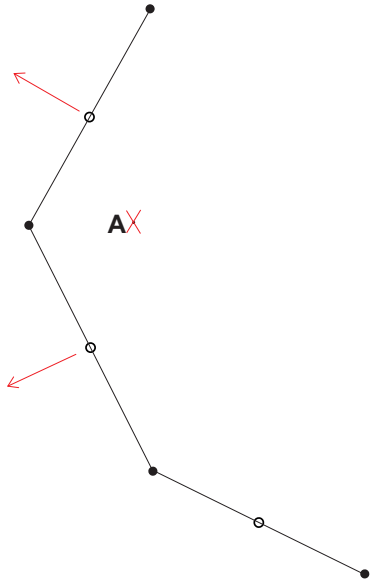

(a) Vorton deletion

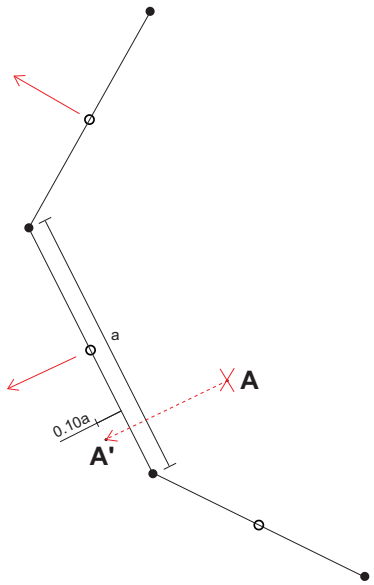

(b) Vorton replacement

Figure 3.7: The possible options for penetrating vortons treatment

3.4 Particle trajectories in a flow induced by a non lifting circle, moving at uniform speed

In this section it is analyzed the flow induced by a non lifting circle, moving at uniform speed. The circle is approximated by thirty-two equally dimensioned source panels. It has been chosen this number of panels because it is gives a panel length to chord ratio comparable to that of the 3D cases analyzed in chapter five. Usually the panels are not equally spaced, the leading edge panels are smaller than the other ones, but this is done because it is necessary to respect a given ratio between curvature and panel size in order to well represent the flow. Since the circle is a geometrical figure with the property of being a constant curvature figure it is better to equally size the panels. In figure (3.8) it is shown a sketch of the flow induced by a circle moving with uniform speed. In all the tests executed in this chapter the circle velocity in the x direction is assigned and equal to $U_\infty = 1m/s$, together with the circle radius which is unitary. Thus these two data are considered assigned and they shall not be repeated from now on.

The main interest in this work is the interaction between the wake vortons and the bodies immersed into this wake and the related problems. Part of these problems, as already seen in the above sections, is the fact that in some conditions even passive particles can enter into solid bodies, and this is an evident error in particle trajectory calculation. Therefore in this section the interest goes towards the trajectory calculation using two different time integration schemes, the RK2 and the FWE. Since a trajectory computed with the first scheme is far more accurate than the same one computed with the second scheme, the trajectories calculated with the RK2 scheme are used

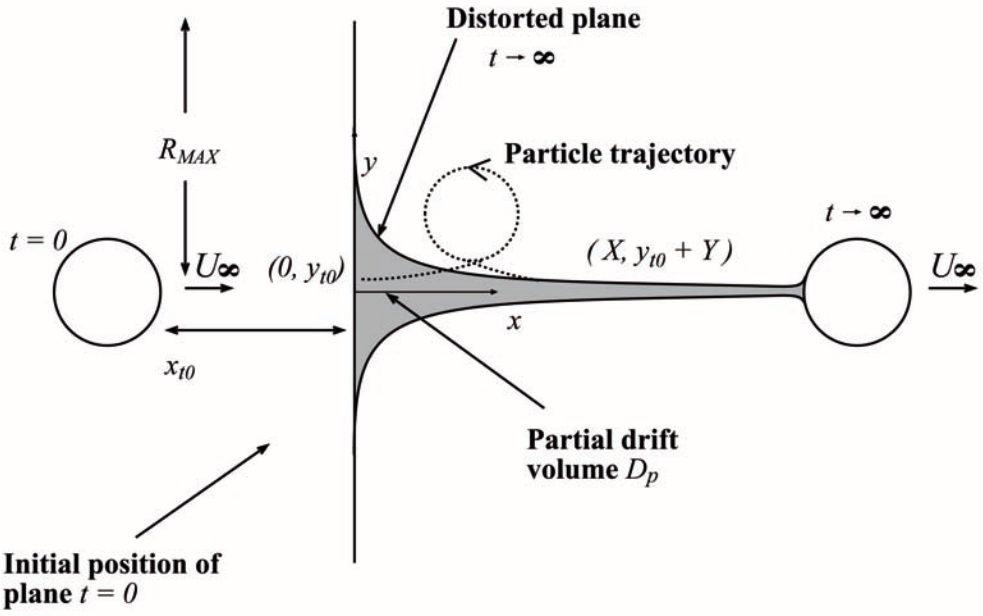

Figure 3.8: A sketch of the flow induced by a non lifting cylinder, moving at uniform speed

as a comparing term to probe the quality of those computed with the FWE scheme, once shown that it is proper to do so. All of this it is done in order to understand if there are just a few particles which enter or not into the body. Once understood this, since the problem in how dealing with vortons is still open, if they are just a few the error introduced by their simple deletion is comparable to the other errors which afflict a low order panel method.

3.4.1 The reference trajectories

As already written above, it has not been found any bibliographical reference about an analytical function $\underline{r}(t)$ of a particle moving into this flow to be directly compared to a numerical trajectory computed with a FWE time integration scheme. Therefore it has been developed the Appendix B to know what is the final position of a particle in this flow, when the circle has arrived far downstream. In figure (3.8) are pictured some quantities used in this appendix useful to compute the (3.2), which plays a key role. The radius of a circular plane of marked particles is named R_{max}, x_{t0} is the initial separation between the center of the moving object and the plane of marked particles, positive as shown in figure, y_{t0} is the starting y coordinate of a particle belonging to the marked plane of particles, X and Y are the displacement coordinates respectively in the x and y direction, R is the radius of the moving circle. The equation (3.2) is important because the displacement X also coincides with the x coordinate of the final position of the particle, while the y coordinate is y_{fin}, not Y.

$$y_{fin} = y\left(1 - \frac{R^2}{r^2}\right) \tag{3.1}$$

$$X = \int_{\theta_0}^{\pi} \frac{R^2(1 - 2sin^2\theta)r}{R^2 sin\theta + r y_{fin}} d\theta \tag{3.2}$$

About the (3.2) it is important to know that X is a function of x_{t0} and of y_{t0}, and that into the integrand θ is the integration variable and it is also the independent variable of the functions r and y_{fin} [1]. It is also important to know that the circle is moving along the x axis. If R_{max} goes to infinity it is possible to compute D_P the partial drift volume, and if also x_{t0} goes to plus infinity $D_P = D_V$ where D_V is the Lagrangian drift volume. The existence of these volumes (areas in a 2D case) is related to the fact that when a solid object passes through a plane of marked particles they tend to be displaced when the object has arrived far downstream [2]. The Lagrangian drift volume D_V is equal to the volume corresponding to the added mass of the body, in this case it is the area of a unitary radius circle. It is always $D_P < D_V$ because when x_{t0} is not plus infinity there are some particles into the marked plane which assume $X < 0$, while when x_{t0} is plus infinity there are only particles into the marked plane which assume $X > 0$ [73] [74] [79].

$$D_p = \int_{-\infty}^{\infty} X dy \tag{3.3}$$

To check if the trajectories computed with a 2D Douglas-Neumann panel method with a RK2 time integration scheme is a good reference for a comparison with the trajectories obtained from the FWE scheme it is needed analyzing the (3.3). To build the figure (3.9) the marked plane of infinite radius has been replaced with a distribution of passive particles which span along the y axis, between $y = -12m$ and $y = 12m$, equally spaced but in a variable number, corresponding to the abscissa in figure. The drift area is reported on the ordinate axis, it is computed via a trapezoidal integration of the (3.3), given the final position of the particles. The plots with circle

[1] See the Appendix B and the symbology to know their meanings

[2] See Appendix B and bibl. [73] [74] for the details

markers match the integration of the (3.3) using the final particle positions computed with the (3.1) and (3.2); since the (3.2) applies when the moving circle has arrived far downstream these plots are labeled in legend with "$\Delta t = \infty$". Instead the plots with "x" markers correspond to the case using as final positions those extracted from the numerical RK2 trajectories of the particles after a finite elapsed time, reported in legend. These trajectories have been computed using a time-step $\Delta t \cong 0.01$. The legend also reports the x_{t0} quantity. In figure (3.9) it is shown that the trends given by the points created from the RK2 trajectories give area results of lesser entity than the analogous given by equations (3.1) and (3.3). This is due to the fact that computing a numerical trajectory it is not possible to assign an infinite elapsed time t_{el}. However it is clear that the plots are trending towards the exact Lagrangian drift area value, which is about $3.14m^2$.

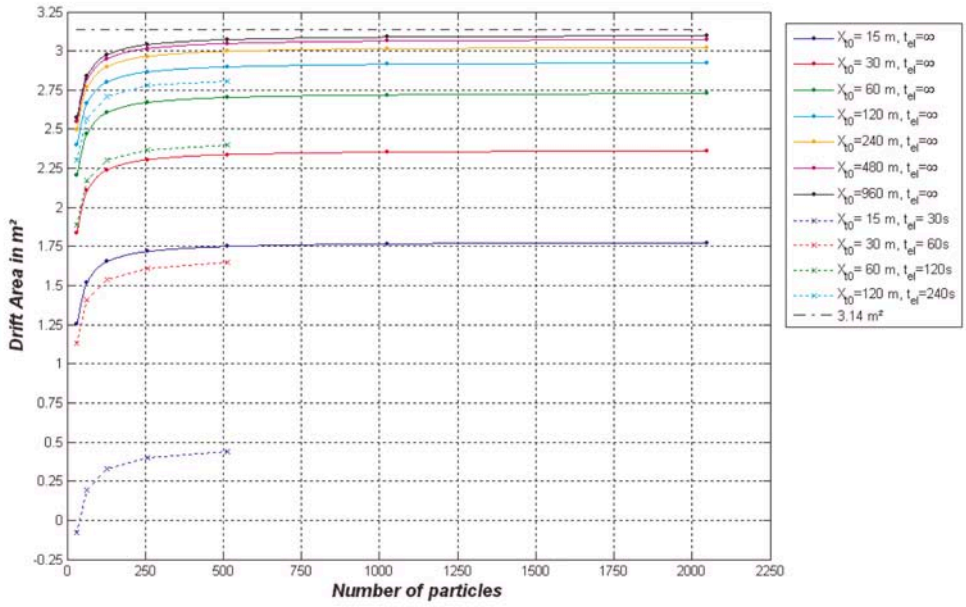

Figure 3.9: Trends of the Lagrangian drift areas, based on the equation (3.2) and on the numerical trajectory calculation

In figure (3.10) the red line represents the numerical integration of the (3.2), therefore it represents the position of the particle when the circle has arrived far downstream, in this case it is $x_{t0} = 12m$. This figure indicates that the displacement can be either positive or negative, as already anticipated above. However the axes are not scaled in order to show that this negative displacement has a curvature which brings the displacement at zero when y_{t0} goes to infinity, as it should be expected by the reader.

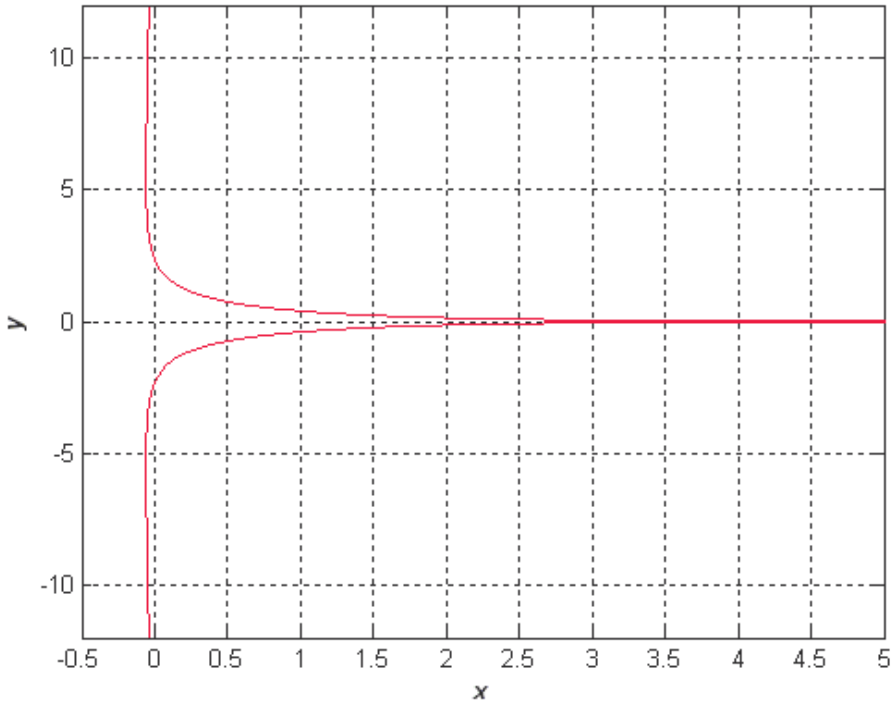

Figure 3.10: Final positions of the particles induced by a circle moving at uniform velocity and starting at $12m$ from the marked plane of particles

In figure (3.11) the red line has the same meaning which has in figure (3.10), instead the blue lines are trajectories computed assuming that the overall elapsed time is $t_{el} = 24s$ and it is $x_{t0} = 12m$ again. These trajectories

are computed assuming a time step $\Delta t = 0.0625s$ and using a RK2 time integration scheme. During preliminary tests smaller time steps did not give remarkable differences. Moreover, observing figure (3.11), there is a small gap between the red line and the final position of the trajectory, because to compute a trajectory it is needed a finite elapsed time, which means a finite traslation of the circle, while the red line is related to an infinite traslation of the circle. Finally the shape of the trajectories is similar (but of course not coincident) to those in [74]. These checks show that it is proper to compare the trajectories computed with a FWE integration scheme with the analogous done with the RK2 one, provided these trajectories use a sufficiently small Δt.

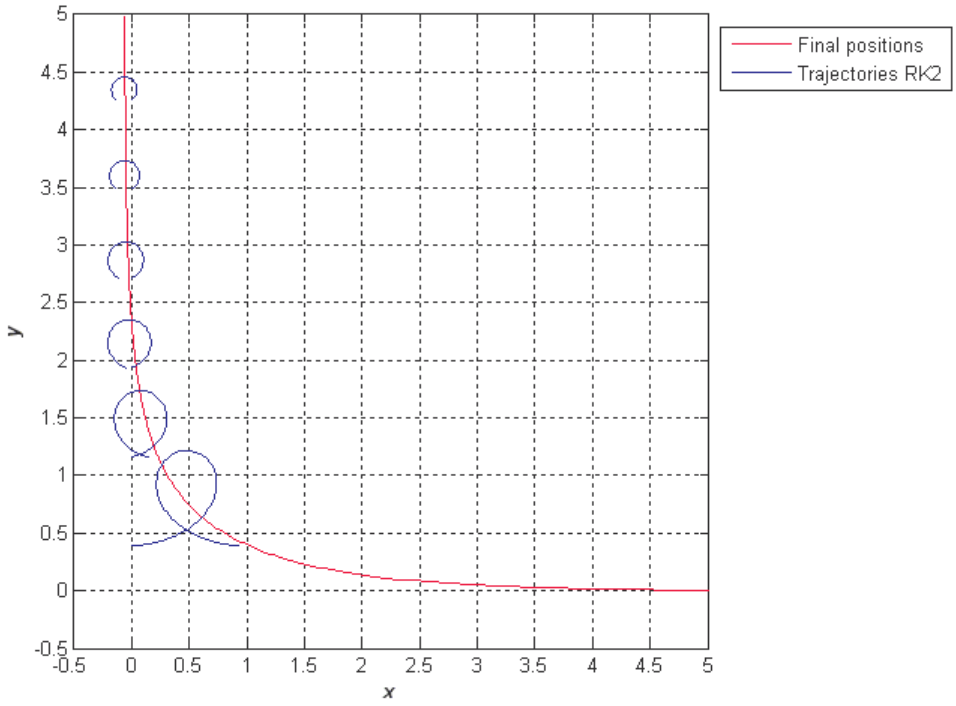

Figure 3.11: The particle trajectories induced by a circle moving at $1m/s$ and starting at $12m$ from the marked plane of particles

3.4.2 The effects of the time step on the trajectory computation

The common data used to compute the trajectories in this subsection are the overall elapsed time $t_{el} = 24s$, $U_\infty = 1m/s$ and $x_{t0} = 12m$, the red and the blue lines plotted into the figures of this subsection have the same meaning of those plotted in figure (3.11). Due to the symmetry of the problem the figures into this subsection should be seen as symmetrical to the x axis.

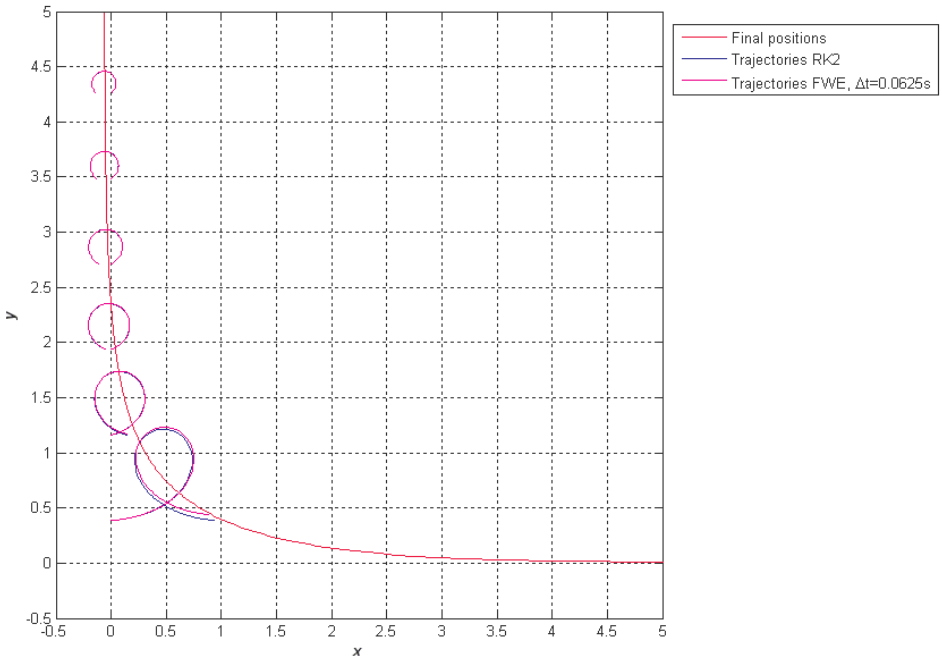

Figure 3.12: Comparison between the particle trajectories induced by a circle moving at $1m/s$ and starting at $12m$ from the marked plane of particles, with indicated time step

The first comparison is done in figure (3.12), the chosen timestep into

the FWE plot is $\Delta t = 0.0625s$. The confrontation between the trajectories computed with the RK2 scheme and and with the FWE scheme indicates that the numerical error of the external trajectories computation is negligible, the trajectory which is closest to the $x = 0$ line has a contained error. After all the time step $\Delta t = 0.0625s$ is very small, and unfortunately to keep reasonable the time required for the calculations in a 3D simulation it is needed to use larger time steps. The required calculation time, excluding the time required to create the graphical output, has been $t_{cpu} = 25.407s$ for the RK2 trajectory and $t_{cpu} = 11,453s$ for the FWE trajectory. The ratio between these calculation times is almost two because actually a RK2 scheme iterates twice a FWE scheme. As it could be expected there is a trade-off between solution accuracy and calculation time.

Repeating the required calculations to evaluate the particle trajectories induced by the moving circle with larger timesteps yields the figures (3.13) and the (3.14), where the time-step is respectively $\Delta t = 0.5s$ and $\Delta t = 1.5s$, and the calculation times are $t_{cpu} = 1.640s$ and $t_{cpu} = 0.765s$. Instead the RK2 plot still employs $\Delta t = 0.0625s$

Using the intermediate time step $\Delta t = 0.5s$ the error compared to the previous case is growing, as expected, but there are not further consequences, while using the coarsest time step $\Delta t = 1.5s$ has happened what has been anticipated in §3.2. In figure (3.14) some particles penetrated the body, therefore their trajectories become affected by an unacceptable numerical error. A first attempt to rectify this error is to verify, in the same way described in §3.2, if the particle is or not into the body, and if it is inside, the main time step is halved until the updated position is again outside the body, then it is restored the main timestep.

The results of such approach are shown in figure (3.14). The result is poor,

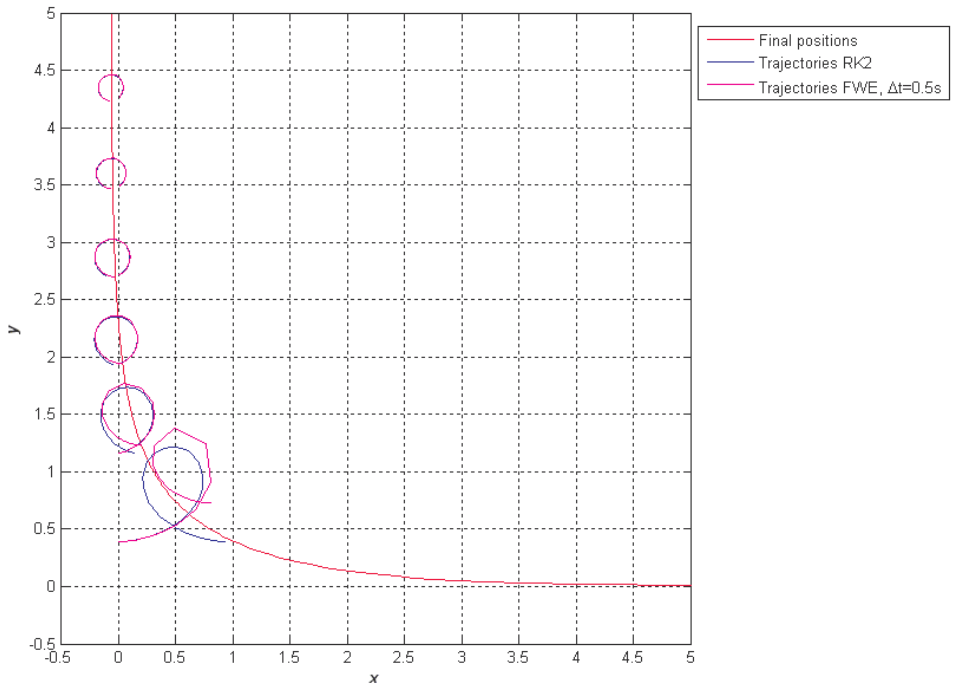

Figure 3.13: Comparison between the particle trajectories induced by a circle moving at $1m/s$ and starting at $12m$ from the marked plane of particles, with indicated time step

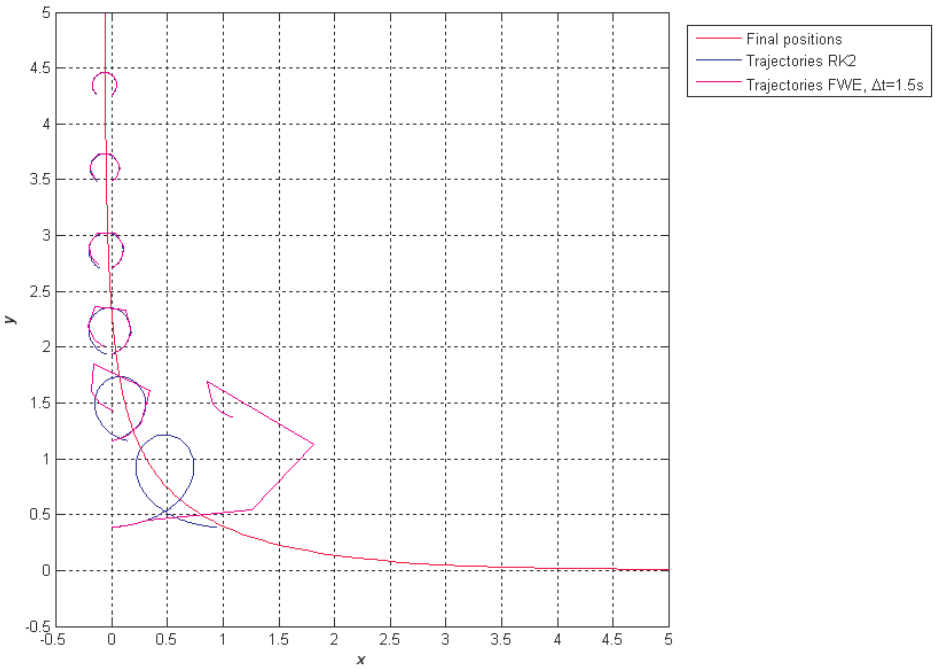

Figure 3.14: Comparison between the particle trajectories induced by a circle moving at $1m/s$ and starting at $12m$ from the marked plane of particles, with indicated time step

and does not justify the above described manipulation of the timestep.

The plots using the intermediate time step $\Delta t = 0.5s$ are interesting because there is a peculiar ratio between this time-step multiplied by the circle speed and the circle diameter, which can be seen as a chord. This ratio is equal to 4 and is typical of 3D uses of the panel methods. Therefore, if the particle is a vorton, it is still verified if the particle is inside or not the body, but the time step manipulation is substituted with a simple deletion of these particles. The reason of this is that the problem in how dealing with these vortons is still open, and the vorticity field of the wake is not altered too much until the deleted particles are few, as it has just been verified. Thus here it has just been chosen the simplest approximation. A forward euler scheme is of course more approximative compared to other schemes, but the use of more accurate schemes requires more calculation time, which is not the goal of a fast preliminary design tool.

Chapter 4

WAKE-BODY INTERACTIONS

The goal of this chapter is to analyze the interaction between the wake shed from an upstream body which flows over a downstream body. This analysis is done examining two test cases. The first one is a wake interaction between a pitching and heaving wing and a fixed downstream wing, the second one is a wake interaction between a propeller and a wing section. These numerical test cases have been run with an unsteady, three-dimensional, low-order and multi-body solver named PaMS (**Pa**nel **M**ethod **S**olver) which uses panels when modeling the bodies and a panel-vortons combination when modeling the wake. Another goal is also to understand if some of these particles, the vortons, penetrate or not the body and if this has remarkable effects over the results. As already shown in section §3.1 there are some causes which induce numerical error in particle path calculation. Since the effects have only been shown over passive particles now it is required to analyze the effects of these errors if the particles are active.

4.1 PaMS code description and recent changes

PaMS (**Pa**nel **M**ethod **S**olver) code is an open source software for the resolution of potential flow fields by means of the panel method technique. This code has been developed at DIAS in order to own a satisfactory analysis and design tool, focusing on a drastic reduction of the costs, in terms of overall time, resources and man power, by using unstructured grid with both quadrilateral and triangular panels, and by introducing a wide variety of boundary and closure conditions, including the existence of an air/water interface to perform a variety of aeronautical and naval fluid dynamic time-dependent computations. A feature of the PaMS is the capability to use a numerical representation of CAD designs, making unnecessary steps like the geometry treatment and paneling when an acceptable CAD model is available. This feature allows a greater simplicity and swiftness during the paneling without altering the result accuracy, and improves the quality of the body discretization since a CAD model is often far more accurate than the panel model useful for aeronautical purposes.

Another simplification arises from an option which consents to panel separately different parts of a same ensemble (for example the wing-fuselage group of an airplane) and to reposition these parts on the basis of specific needs. As an example, this option is useful for the treatment of eventual intersections between two or more bodies.

Another important characteristic is the computation of pressure loads directly in the grid points, through a reconstruction technique and derivation of the potential function. The availability of pressure values correctly computed in the grid points consents the coupling between a fluid dynamic solution with another solution obtained from structural analysis solvers using the same paneling. Moreover, due to some routines able to manage possible

deformation of the bodies in time, the PaMS code is simple to use also when computing unsteady fluid-structure interactions, in such cases as aeroelastic problems (like the sails).

The PaMS code is also able to interface itself with other commercial softwares, further improving its effectiveness. PaMS is capable of directly interfacing with some of the most diffuse commercial softwares like Gambit, Nastran, Hypermesh, Tecplot, allowing the best post-processing and putting the PaMS code in ideal conditions to increase its performances. This code has been used to solve a number of scientific and technical, steady and unsteady problems. It seems capable to perform complex simulations coupled to both structural and dynamics methods and/or by introducing deformations due to fluid dynamics loads [15].

As already written in the previous chapter there is a chance that vortons can penetrate bodies under some conditions, therefore the PaMS code has been changed introducing the check described in §3.3. Up to now it has not been explicitly exposed what is to be done once it is executed the check, now it is mandatory to decide what to do with these penetrating particles. A simple decision is to delete them (see figure (4.1a)). However, since a necessary condition to consider acceptable the deletion of wake vortons is that there are just a few of them which penetrate, it is needed to test first if there are unacceptable calculation errors. Another option is the following. Once executed the check, the penetrating vorton is replaced outside again. The normal direction belonging to the panel which is closest to the penetrating vorton is an information already available. Thus the vorton is replaced along this direction at a distance equal to 0.10 times the mean size of the reference panel (see figure (4.1b)). Since both options are going to be used it will explicitly be reported which one is currently used.

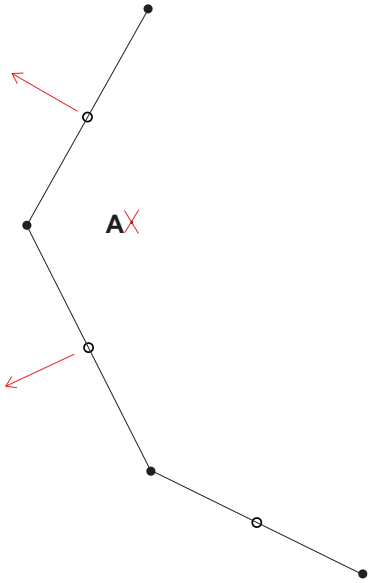

(a) Vorton deletion

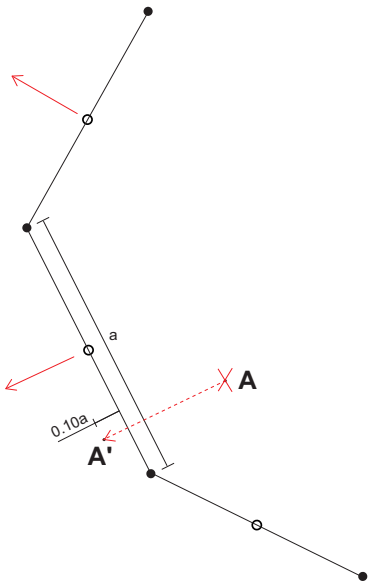

(b) Vorton replacement

Figure 4.1: The possible options for penetrating vortons treatment

4.2 Wake interaction between a pitching and heaving airfoil and a fixed downstream airfoil

The ideal flow theory allows to calculate the aerodynamic characteristics of wing sections, even though the simplifying assumptions limit its applicability. Moreover, T. Theodorsen developed a theory, valid if the flow field is linear and potential and the airfoil is thin, which computes the airfoil aerodynamic characteristics if an isolated 2D wing section is pitching and heaving [80]. Other references to be considered are [81] [82] [83] [84] [85] [86].

The airfoil examined in this section is the NACA 0012 and it is pictured in figure (4.2). Actually the flow model upon which are based panel methods is linear and potential and the NACA 0012 airfoil is thin, thus it is possible to analyze an isolated NACA 0012 airfoil using Theodorsen's theory. As already said above, PaMS is a 3D solver, thus, in order to gather 2D airfoil information from such codes, it is required to execute runs using large Aspect Ratio (AR) wings, in order to reduce 3D induced drag effects, and take these informations from the wing mid-section. This effort allows the comparison with 2D data or theories. If the comparing term is Theodorsen's theory, the wing must be isolated.

The pitching and heaving wing, whose aspect ratio is $AR = 24$ and its chord length is $1m$, is straight rectangular and is mounting a NACA 0012 airfoil. The 2D lift coefficient of this simulation is compared to the analytical results obtained using Theodorsen's theory for an analogous oscillating airfoil. In figure (4.3) it is evident the good agreement between these two results, thus it is shown the method accuracy in representing the unsteady

vorticity in the wake. The pitching and heaving equations are the following:

$$\beta(t) = \beta_a \sin(\omega_{PH} t + \phi_{PH}) = 10^\circ \sin(\omega_{PH} t - 90^\circ) \tag{4.1}$$

$$h(t) = h_a \sin(\omega_{PH} t) = 0.25 \sin(\omega_{PH} t)\ m \tag{4.2}$$

The pitching motion is about a point on the airfoil chord at a distance 1/4 of the chord from the leading edge, $\beta(t)$ is the instantaneous angle measured clockwise from the mean chord, β_a is the amplitude of pitching oscillation, ϕ_{PH} is the phase angle ahead of the pitching motion and $\omega_{PH} = 2U_\infty/ck$ is the frequency related to the so called reduced frequency k, the period related to this frequency is $16 secs$. The heaving motion is only vertical, $h(t)$ is the instantaneous vertical shift from the mean position, h_a is the amplitude of the heaving oscillation.

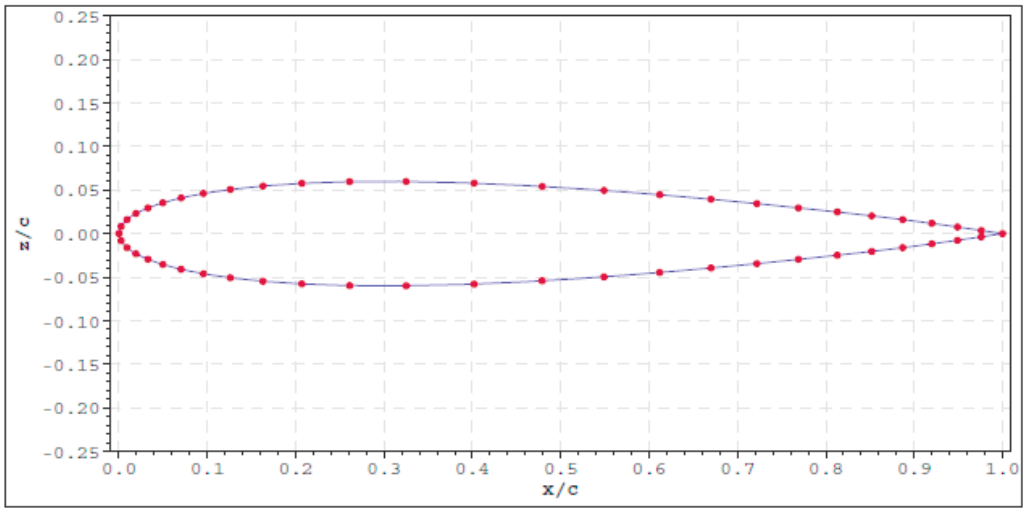

Figure 4.2: NACA 0012 airfoil geometry

The PaMS code with vorton wake has already been tested and resulted successful when it computes data for isolated bodies, thus are not required other tests on isolated bodies (see Bibl. [64]). Now the attention is focused on the behavior of the PaMS code with the DIAS vorton wake model when

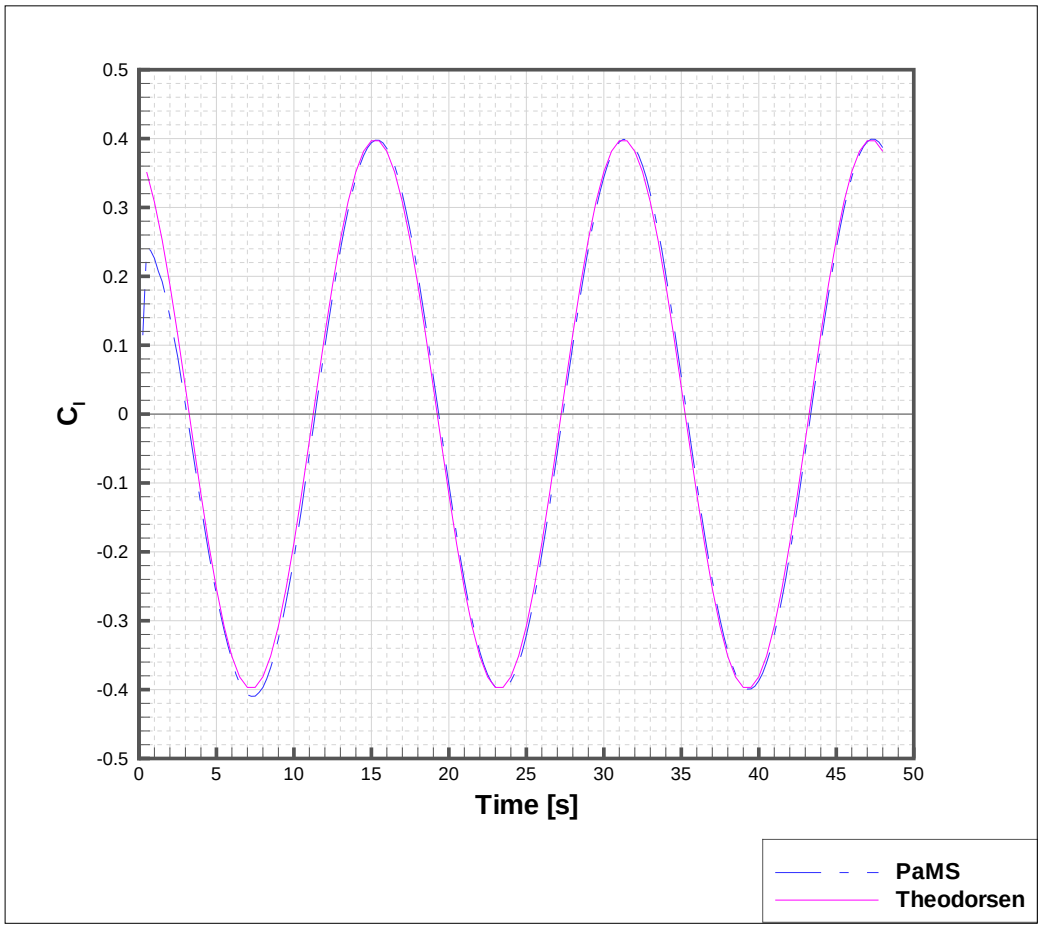

Figure 4.3: NACA 0012 airfoil - comparison between the lift coefficients resulting from the numerical analysis data and the Theodorsen's theory about the pitching and heaving motion

the wake of a pitch-heaving wing intersects with downstream fixed wing. The pitching and heaving wing is the same as before, the downstream body is a straight rectangular wing with the same aspect ratio and airfoil of the upstream oscillating wing. In order to analyze the effects due to the oscillating wing wake on the downstream wing, the lift coefficients resulting from this simulation are analyzed.

Figure (4.4) shows the lift coefficients for the upwind and downwind wing mid-sections. It is well known that a NACA 0012 airfoil is symmetrical, so, if an isolated airfoil is exposed at null angle of attack there is no net lifting force or pitching moment. Considering figure (4.4), as the wake approaches the downwind airfoil, the lift coefficient raises, and when the wake is gone beyond the airfoil the lift coefficient has became a periodic function which has the same frequency of the normal force oscillation of the upstream airfoil. The maximum value of the lifting coefficient on the non oscillating airfoil verifies when are approaching those vortons released from the upstream wing when its normal force value is maximum. Moreover, in figure (4.4), during the time interval between $t = 41.5secs$ and $t = 41.75secs$, there is a small but visible periodic irregularity. Observing a time period between $t = 41secs$ and $t = 41.75secs$, shown in figure (4.7) it is clear that the vorton deleting mechanism is working, and the irregularity happens when vortons are deleted. In chapter 4 it has already been shown that reducing the time step is a way to avoid particles penetrating, however reducing the time step in order to adjust a single or a few points in a graph is not very useful, better solutions would be or a proper post-processing or treating the penetrating vortons differently. Another periodic irregularity happens at $t = 33.5secs$, it shares the same nature with the previous one, thus it is no further discussed.

In section §4.1 have been shown two options if a vorton has penetrated

the body, deletion or replacement. Now if it is taken the second option, the replacement, there is no more the previous vorticity loss due to vorton deletion. Referring to the pitch-heaving airfoil, swapping between these two techniques is pointless, in figure (4.5) the graphs are superimposed. Instead in figure 4.6, where the attention is focused on the fixed airfoil, the graphs are almost superimposed, using the vorton replacement technique cancels the irregularities in the graph.

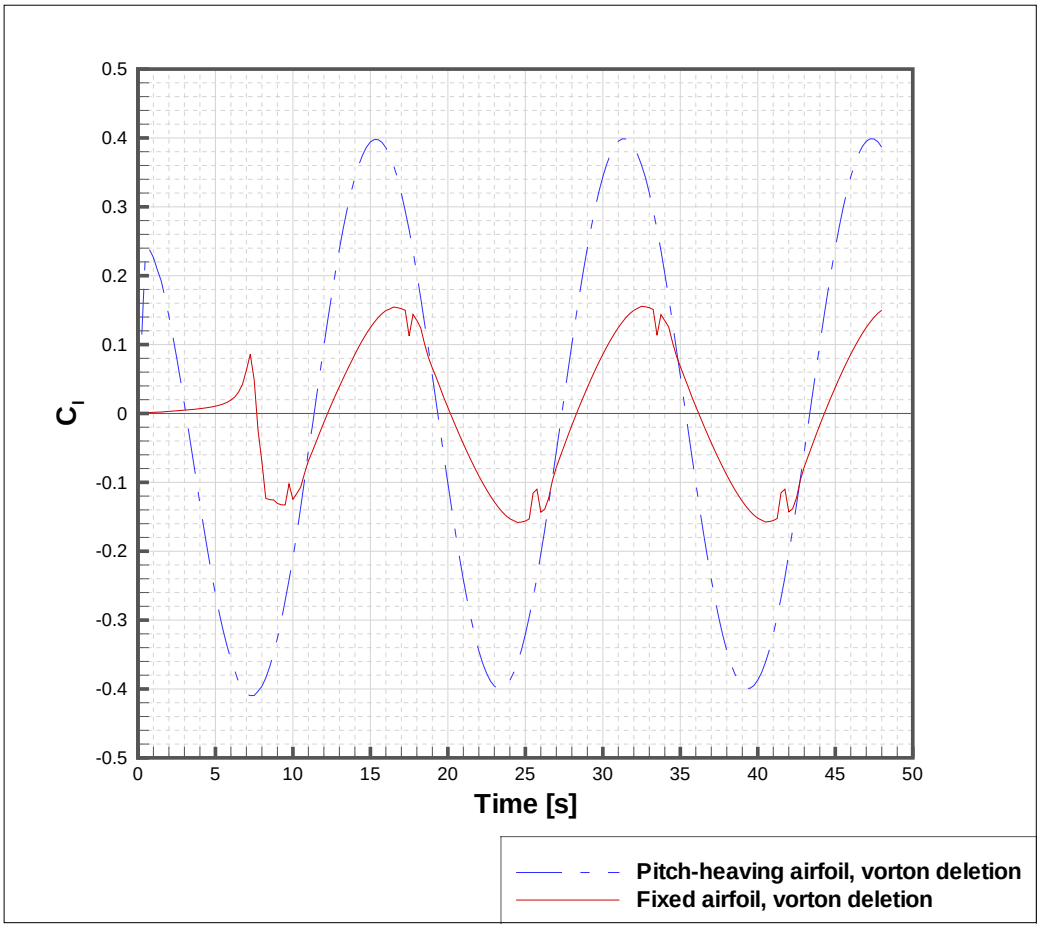

Figure 4.4: The lift coefficients of a pitching and heaving NACA 0012 airfoil and a downstream fixed NACA 0012 airfoil

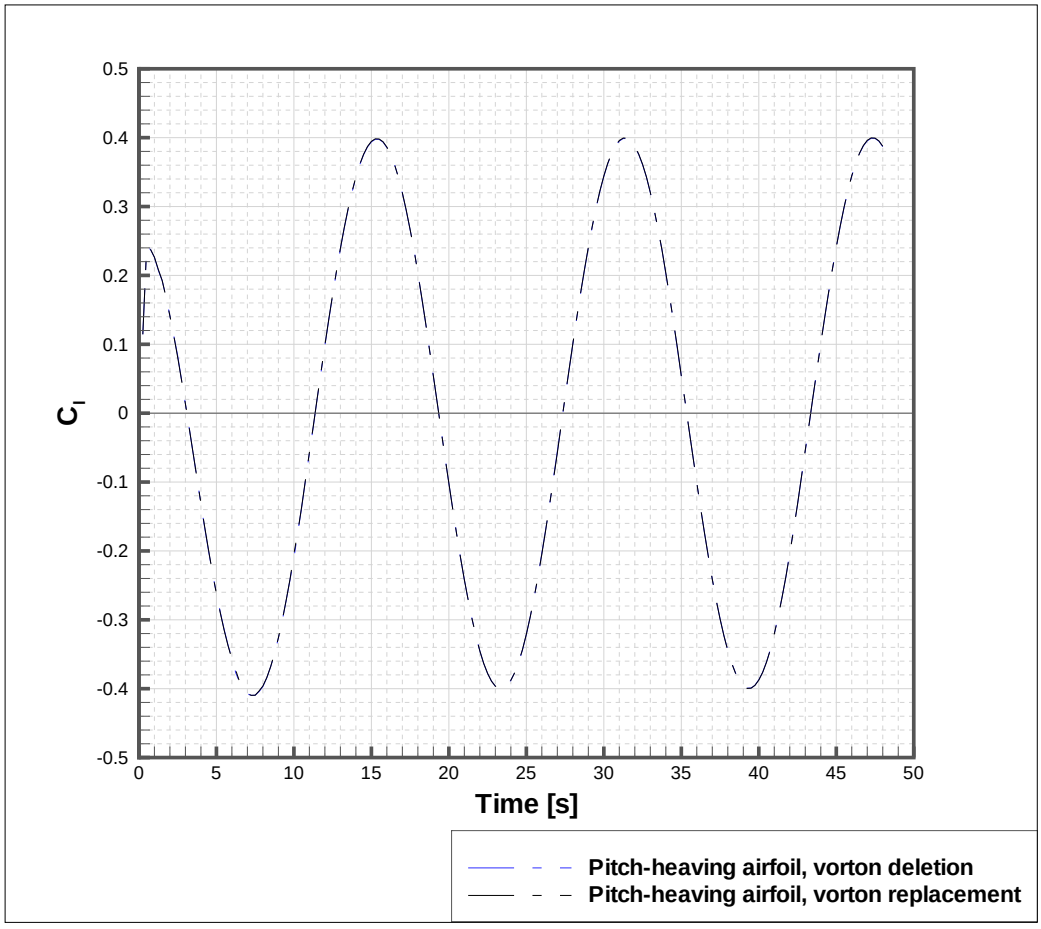

Figure 4.5: The lift coefficients of the pitching and heaving NACA 0012 airfoil, obtained using different vorton treatments

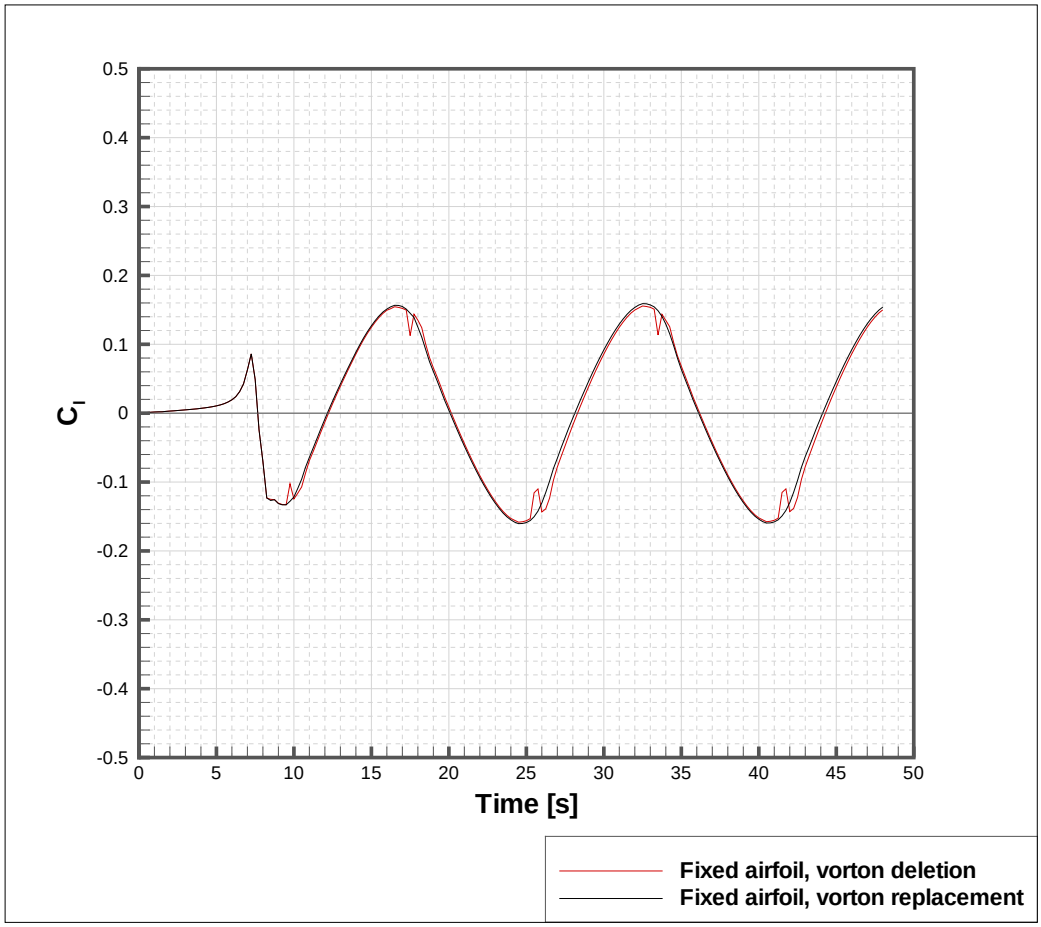

Figure 4.6: The lift coefficients of the fixed NACA 0012 airfoil, obtained using different vorton treatments

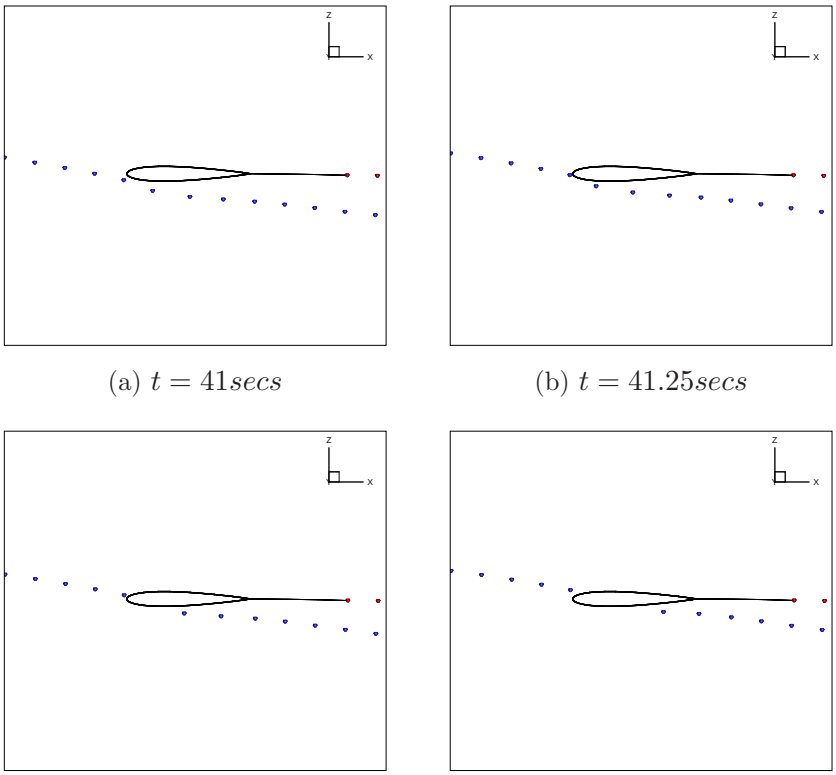

(a) $t = 41 secs$ (b) $t = 41.25 secs$

(c) $t = 41.50 secs$ (d) $t = 41.75 secs$

Figure 4.7: NACA 0012 airfoil - Example of vorton deletion

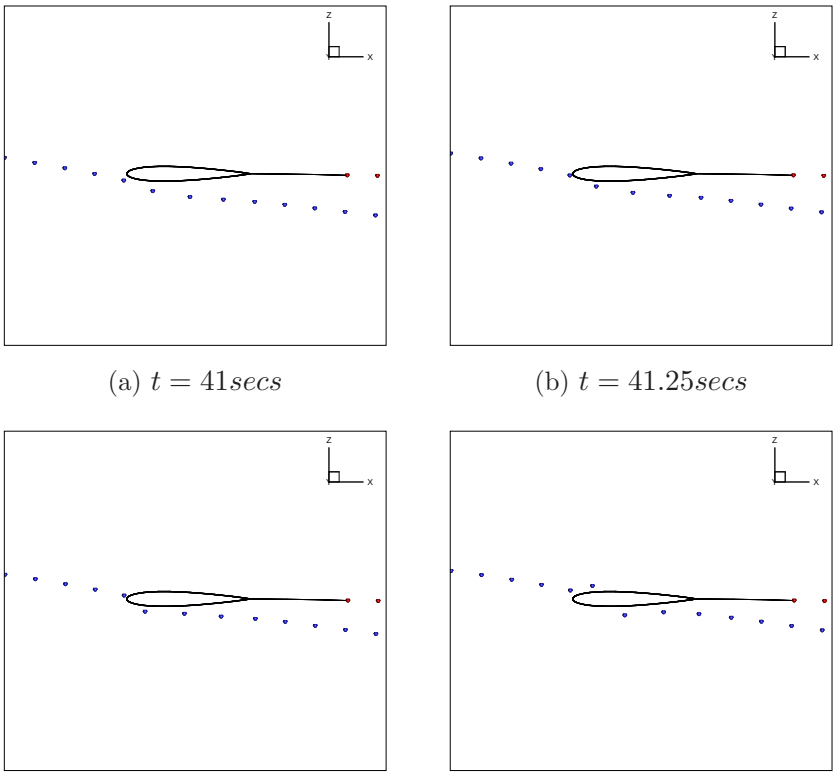

(a) $t = 41 secs$ (b) $t = 41.25 secs$

(c) $t = 41.50 secs$ (d) $t = 41.75 secs$

Figure 4.8: NACA 0012 airfoil - Example of vorton replacement

4.3 Wake interaction between a propfan and a wing section

The experimental data of this test case are taken from a set of tests conducted at the NASA Langley Research Center in its 16 Foot Transonic Tunnel, whose details are reported into the references [87] [88] [89] [90] [91] [92] [93] [94]. It is considered an underwing nacelle integrated into an unswept, untapered, supercritical wing model, mounted on the wind tunnel support structure, completed with a powered propfan. The airfoil mounted on the wing is the 10 percent-thick NASA supercritical airfoil 33, whose details are reported in [90]; it is publicly available and the interested reader can consult it. The wing chord is one foot in length, and it had approximately 350 pressure taps to measure static pressures, their chordwise locations are the same all the way across the wing, while the spanwise locations are symmetric about the centerline of the propfan. Figures (4.9) (4.10) and (4.11) show the geometrical details of the SR2-wing-nacelle model.

The SR-2 propfan is 12.5 inches in diameter (d), has eight blades and its rotation verse is clockwise as viewed from the rear. As stated in [94], there are doubts about the propeller blade shape, thus the numerical simulations run in PaMS use the data available in this report, labeled in table (4.1). The meanings of the symbols shown into label heading are reported in the "Symbols and Acronyms" section.

Now are exposed the input data of the numerical test run with the PaMS code. The stream angle of attack used into the numerical run is $AoA = 0°$, which agrees with the experimental setup of reference [87]. In reference [87] the flow is at a Mach number $M = 0.7$, instead the numerical test has been run using $V_\infty = 1m/s$, thus the output data referring to the wing need

r/R	τ	c/d	β	$C_{L,design}$	Airfoil
.235	.190	.1438	24.0	-.25	NACA 65
.250	.160	.1440	23.0	-.20	NACA 65
.300	.100	.1442	18.9	-.05	NACA 65
.350	.074	.1460	15.7	.04	Transition
.400	.059	.1480	12.5	.09	Transition
.450	.051	.1488	10.5	.13	Transition
.500	.044	.1500	8.6	.15	Transition
.550	.038	.1498	6.9	.16	NACA 16
.600	.033	.1485	5.0	.17	NACA 16
.650	.030	.1475	3.5	.16	NACA 16
.700	.026	.1460	2.0	.15	NACA 16
.750	.024	.1443	0.5	.13	NACA 16
.800	.023	.1420	-1.0	.10	NACA 16
.850	.022	.1360	-2.5	.08	NACA 16
.900	.021	.1280	-4.5	.06	NACA 16
.950	.020	.1120	-5.7	.03	NACA 16
.975	.020	.0940	-6.2	.015	NACA 16

Table 4.1: SR-2 propfan, geometrical data table.

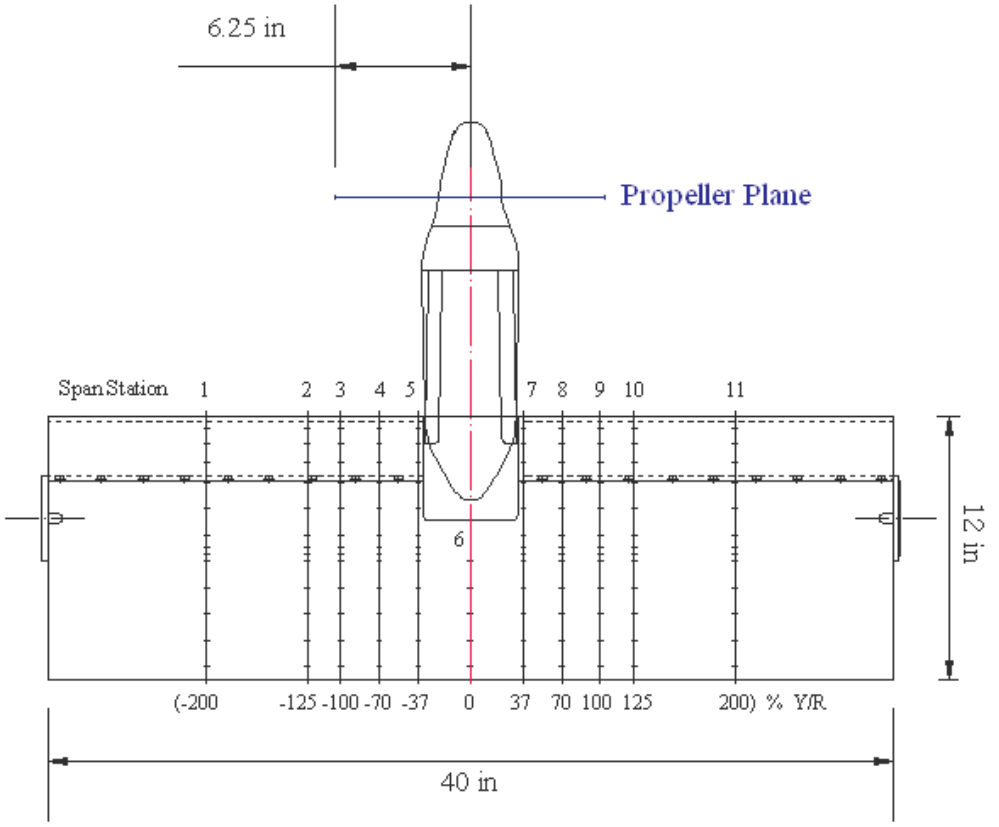

Figure 4.9: Planform of the SR2-wing-nacelle model

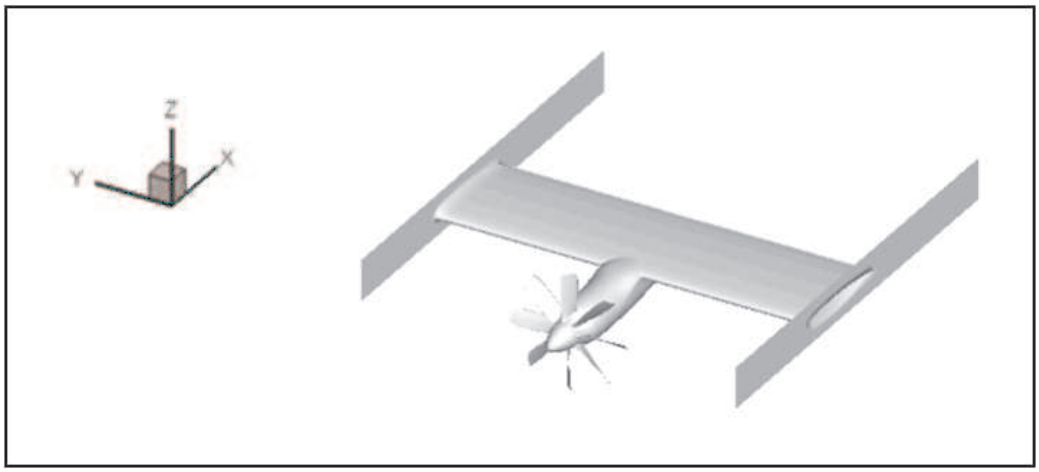

Figure 4.10: SR2 test case CAD model

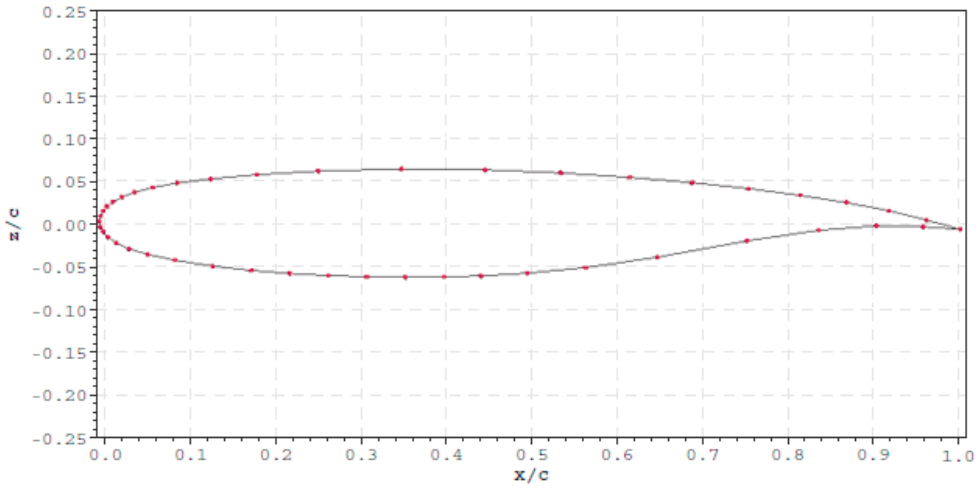

Figure 4.11: NASA 10 percent thick supercritical airfoil 33

post-processing, which will be explained later. The thrust coefficient, C_T, is defined as in equation (4.3), where T is the propeller thrust, d is the propeller diameter and n are the propeller revolutions per second, in reference [87] it is $C_T = 0.245$.

$$C_T = \frac{T}{\rho n^2 d^4} \tag{4.3}$$

In this reference are not clear the details about the propeller advance ratio $J = V_\infty/(nd)$ or the blade pitch angle β at a given station, thus it has been set $\beta = 52.5°$ and in order to achieve $C_T = 0.245$ it has been chosen $J = 2.423$ (corresponding to $1.3rps$). The employed advance ratio has no matches into the other bibliographical references, but the same C_T can be achieved using different combinations of advance ratio and blade pitch angle, thus in reference [87] and in this work it is considered more important to work at a given C_T. Since the flow used into the experiment described in [87] is at a Mach number $M = 0.7$ are expected compressibility effects over the propfan and the wing. Recalling a result about actuator disks [58], it is known that the compressibility correction alters sensibly the C_T only

if the blade loading is sufficiently high. Thus it has not been applied any compressibility correction to the local forces acting over the propeller blades, even if panel methods are based upon the incompressible fluid hypothesis, since the blade loading is small in this case. Instead the data related to the wing, obtained under the incompressible flow hypothesis, are corrected using Karman and Tsien's correction, since there is a global compressibility effect over the wing when the flow is coming at $M = 0.7$. The good agreement between numerical and experimental data shown in figures (4.13) and (4.14) justifies the following fact: the dominating flow conditions are given by C_T and M.

Figures (4.13) and (4.14) show the the C_P comparisons between the experimental data of reference [87] and the numerical output of the PaMS code. Since PaMS code is an unsteady solver, then its data output is also unsteady, therefore the plotted data have been first time-averaged. Moreover, the PaMS code is based upon the potential flow model, which assumes the incompressible fluid hypothesis, then it is needed a correction before comparing PaMS data with the available experimental data. This correction is given by the Karman-Tsien formula, reported in equation (4.4).

$$C_{P,comp} = \frac{C_{P,inc}}{\sqrt{1-M^2} + \frac{C_{P,inc}}{2}\left(\frac{M^2}{1+\sqrt{1-M^2}}\right)} \tag{4.4}$$

The propfan wake generates two main effects on the downstream wing, an upwash effect on the wing side of station 4 and a downwash effect on the wing side of station 8. During this run it has been used the vorton deleting option, and since there is a good agreement between the experimental and numerical data, the choices done about C_T and the vorton deleting option can be confirmed as good choices. At this flow Mach number the experimental data suggest that the wing is in a transonic flow state, thus it is not correct

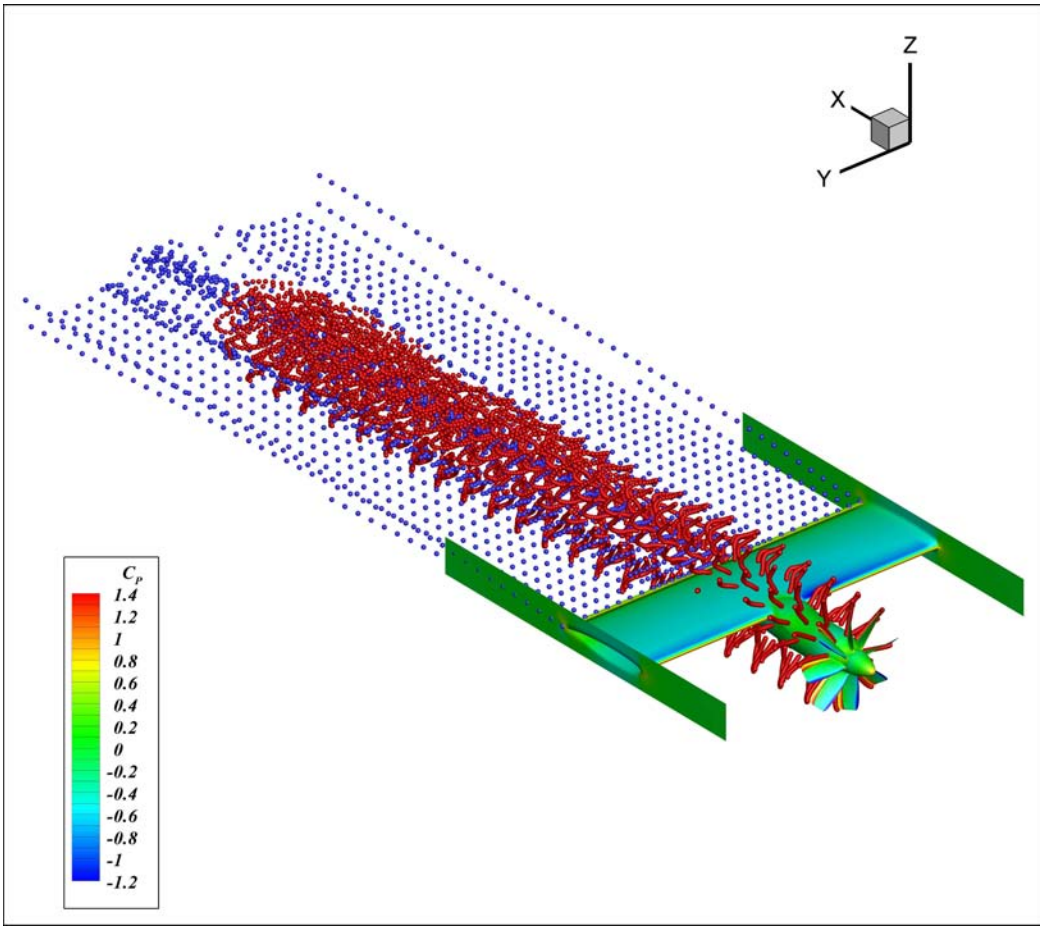

Figure 4.12: 3D view of the SR2-wing-nacelle model

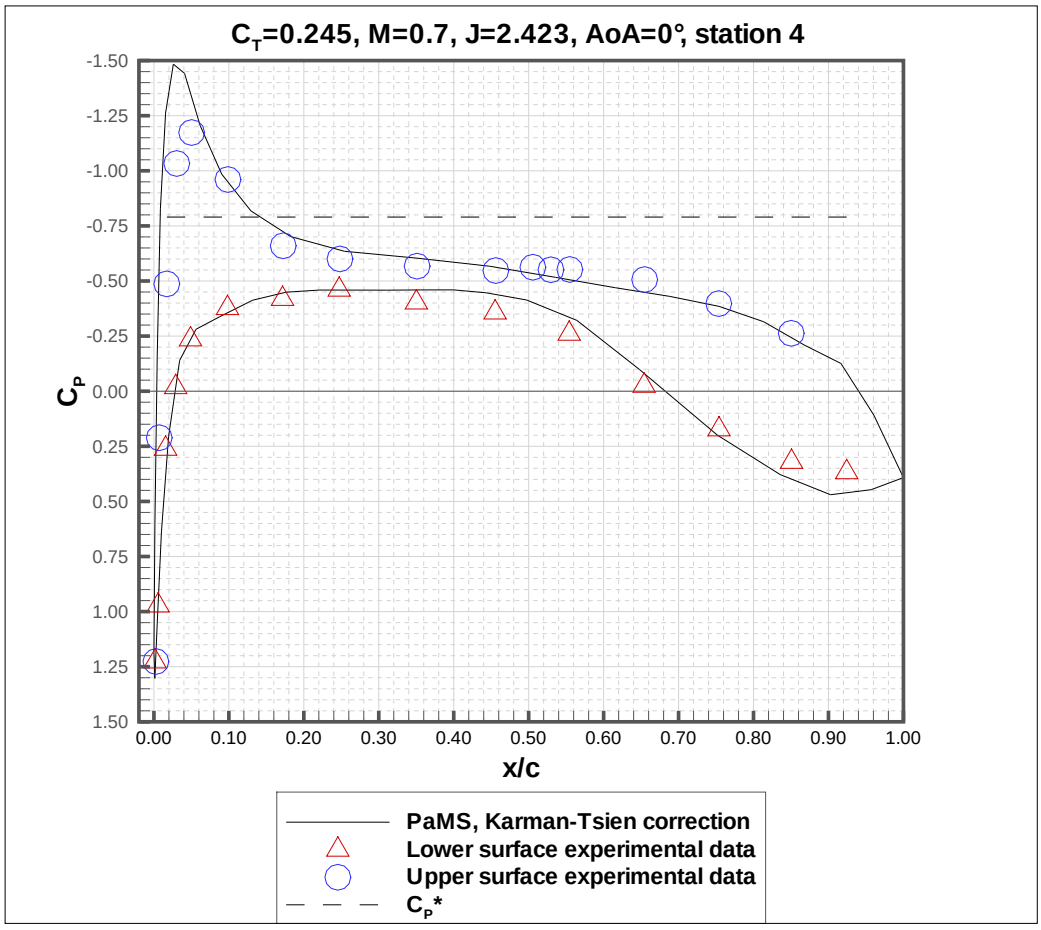

Figure 4.13: Comparison between PaMS output data and experimental data at station 4.

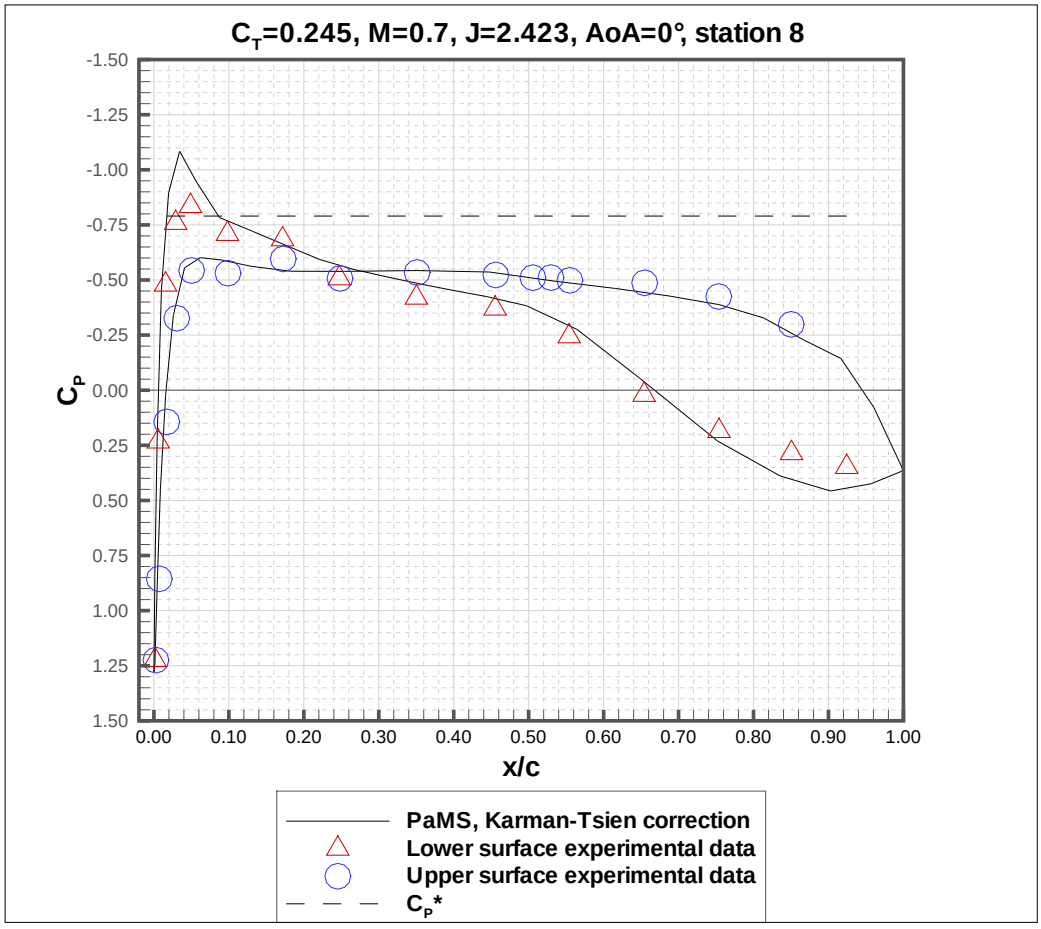

Figure 4.14: Comparison between PaMS output data and experimental data at station 8.

to use the Karman-Tsien correction in presence of shock waves. The sonic pressure coefficient C_P^*, given by equation (4.5), is about -0.78, this value is confirmed in [90].

$$C_P^* = \frac{2}{\gamma M^2}\left[\left(\frac{1+\frac{\gamma-1}{2}M^2}{\frac{\gamma+1}{2}}\right)^{\frac{\gamma}{\gamma-1}} - 1\right] \tag{4.5}$$

The experimental data indicate the presence of supercritical flow at the leading edge portions of the upper surface of the wing located in the upwash side of the propeller. However, in spite of the modeling, the C_P comparisons between the experimental and the numerical data show a good agreement. This agreement is remarkable because it allows to compute the lift coefficient using a code based upon the potential flow model. A similar supercritical flow can be found at the leading edge portions of the lower surface of the wing located in the downwash side of the propeller. These effects are mainly due to vorticity bound to the propfan wake. If the propfan is left rotating and the wake is cut off after a few time-steps (see figure (4.15)), the wake has no more effects over the wing, as it is shown in figure (4.16), where the difference in pressure distribution is infinitesimal and the C_P graphs are almost superimposed.

In conclusion, the interaction between the wing and the propeller wake is due to the high energy slipstream, thus even at subsonic conditions certain portions of the wing section immersed in the slipstream can attain supercritical Mach numbers. The validity of the subsonic panel methods can be extended using the Karman-Tsien compressibility correction, however this level of accuracy is tolerable only during the first stages of the airplane design process. For more accurate calculations it is better to use other options than corrected panel methods.

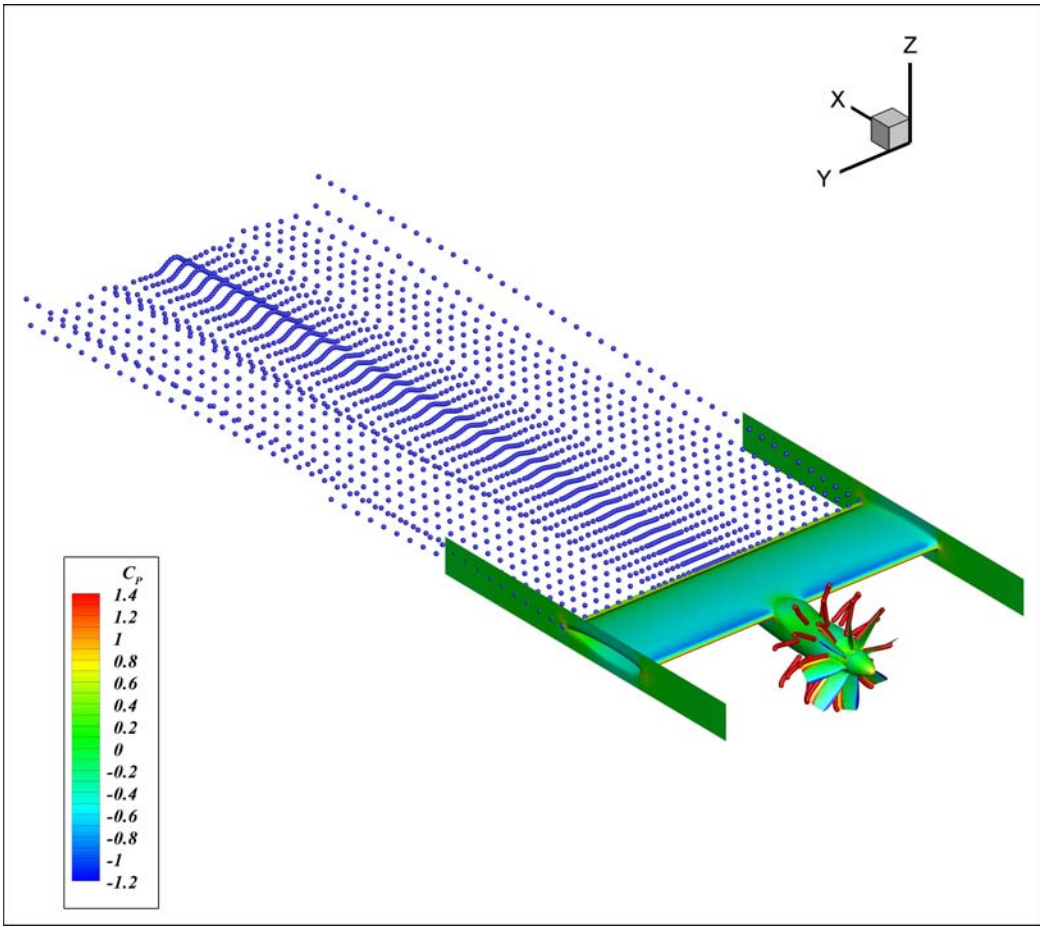

Figure 4.15: 3D view of the SR2-wing-nacelle model with a very short propfan wake.

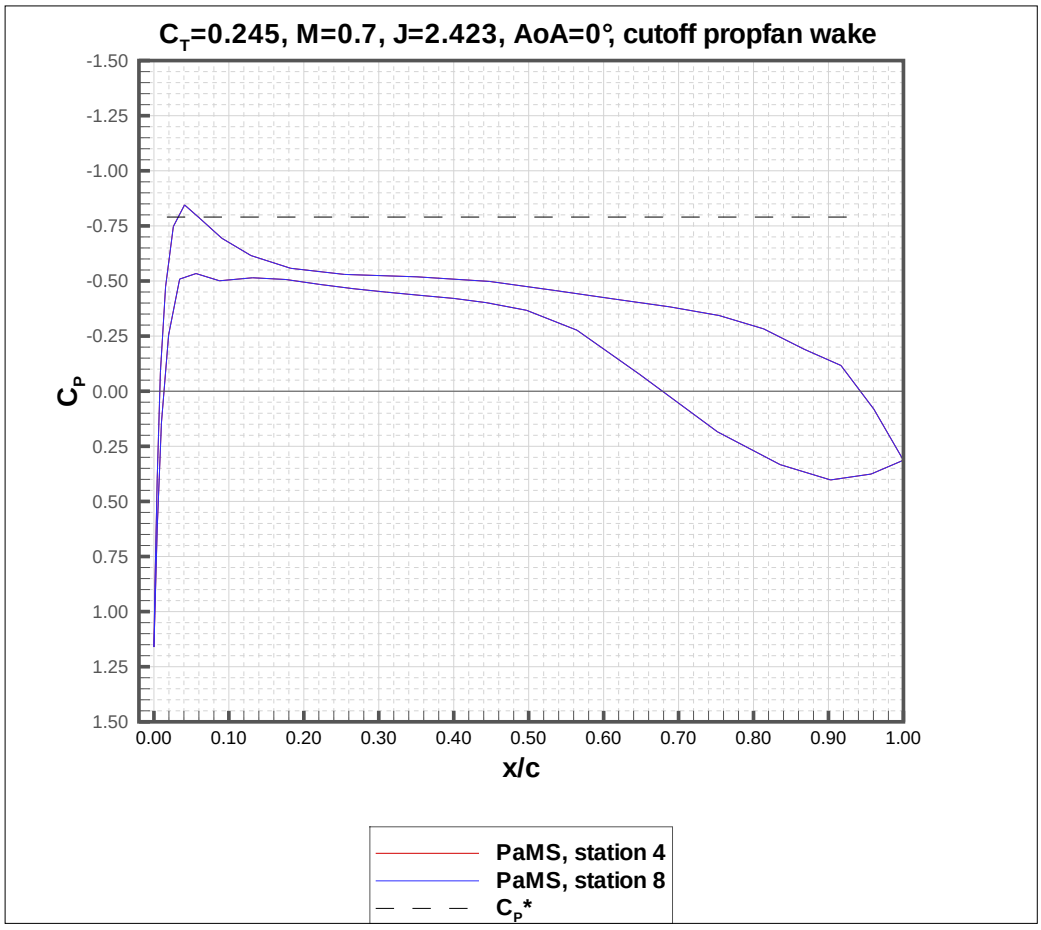

Figure 4.16: Comparison between PaMS output data at stations 4 and 8, after the wake removal.

Conclusions

A vorton wake model into panel methods is capable of modeling wake-body interaction, correctly estimating the forces acting over bodies: using the physical criterion that vortons cannot penetrate impermeable bodies it has been shown, with some examples given by the author, how to apply proper modifications in panel methods without significantly increasing the required computational time.

Adding interfacing capabilities in panel methods transform a vorton wake model into:

- an easy and effective pre- and post-processing design tool
- a fast wake-body interaction analysis tool
- low budget hardware and manpower requirements.

The shown test cases of wake-body interaction demonstrate that in some circumstances the wake-body interaction sensibly alters the forces acting over the bodies, thus it cannot be ignored even at early stages of the design process.

A vorton wake model can now analyze, for example, rolling motion for aircraft, rotor aerodynamics, multi-body problems and, aircrafts flying in close proximity. A vorton wake model, if interfaced with an aeroacustical

model, can estimate noise levels in cabin, completing this class of codes as useful tools during the pre-design stage of an airplane.

Appendix A

The solution of Poisson's equation

A.1 Derivation of the solution of Poisson's equation

There exist different ways to solve Poisson's equation for the potential which requires integration over a finite region of interest. For this work, Green's second identity which, as shown in chapter 2, is a consequence of the divergence theorem, allows to write a solution of Poisson's equation as well as the Green's function (defined in unbounded domain) that will be chosen so as to cause one of the terms in the surface integral to drop out. In this way, the solution of Poisson's equation will be composed by an integral over a finite volume and an integral over the bounding surface.

Consider a closed volume V bounded by a surface S. Let ϕ_1 and ϕ_2 be scalar fields defined on V and S. The Green's Second Identity states that

$$\int_V \left(\phi_1 \nabla^2 \phi_2 - \phi_2 \nabla^2 \phi_1\right) dV = \int_S \left(\phi_1 \frac{\partial \phi_2}{\partial n} - \phi_2 \frac{\partial \phi_1}{\partial n}\right) dS \qquad \text{(A.1)}$$

Let's use this theorem to write the solution of Poisson's equation. Particularly, let

$$\phi_1 = \underline{\Psi}(\underline{r}) \tag{A.2}$$

and

$$\phi_2 = G(\underline{r}, \underline{r}') = -\frac{1}{4\pi|\underline{r} - \underline{r}'|} \tag{A.3}$$

where $\underline{r}$ represents the coordinate of the field point and $\underline{r}'$ represents the coordinate of the source point. Let

$$\nabla^2 G(\underline{r}, \underline{r}') = \delta(\underline{r} - \underline{r}') \tag{A.4}$$

where $\delta(\underline{r} - \underline{r}')$ is a simple delta function. The Second Green's Identity becomes

$$\int_V \left(\underline{\Psi}(\underline{r})\nabla^2 G(\underline{r}, \underline{r}') - G(\underline{r}, \underline{r}')\nabla^2\underline{\Psi}(\underline{r})\right) dV =$$

$$= \int_S \left(\underline{\Psi}(\underline{r})\frac{\partial G(\underline{r}, \underline{r}')}{\partial n} - G(\underline{r}, \underline{r}')\frac{\partial\underline{\Psi}(\underline{r})}{\partial n}\right) dS \tag{A.5}$$

$$\int_V \left(\underline{\Psi}(\underline{r})\delta(\underline{r}, \underline{r}') + \frac{1}{4\pi|\underline{r} - \underline{r}'|}\nabla^2\underline{\Psi}(\underline{r})\right) dV =$$

$$= -\int_S \left(\underline{\Psi}(\underline{r})\frac{\partial}{\partial n}\left(\frac{1}{4\pi|\underline{r} - \underline{r}'|}\right) - \frac{1}{4\pi|\underline{r} - \underline{r}'|}\frac{\partial\underline{\Psi}(\underline{r})}{\partial n}\right) dS \tag{A.6}$$

If $\underline{r}'$ lies in the volume V, then

$$\underline{\Psi}(\underline{r}') = -\int_V \left(\frac{1}{4\pi|\underline{r} - \underline{r}'|}\nabla^2\underline{\Psi}\right) dV +$$

$$-\frac{1}{4\pi}\int_S \left(\underline{\Psi}(\underline{r})\frac{\partial}{\partial n}\left(\frac{1}{|\underline{r} - \underline{r}'|}\right) - \frac{1}{|\underline{r} - \underline{r}'|}\frac{\partial\underline{\Psi}(\underline{r})}{\partial n}\right) dS \tag{A.7}$$

By supposing to have Dirichlet boundary conditions on some surface, let that surface be S, so V will be the enclosed volume. Moreover, choose a

homogeneous solution to add to $G(\underline{r}, \underline{r}')$ so that it will be zero on the whole surface S. Thus, the surface integral term is always zero, and there is no need to know what the normal derivative of the potential is, therefore

$$\underline{\Psi}(\underline{r}') = -\int_V \frac{\nabla^2 \underline{\Psi}}{4\pi|\underline{r} - \underline{r}'|} dV \tag{A.8}$$

As regard the vector velocity potential, this is governed by the Poisson's equation. Furthermore, substituting $\nabla^2 \underline{\Psi} = -\underline{\omega}$ in the above relationship and considering the unsteady nature of the problem, the velocity vector potential due to vorticity in the domain results:

$$\underline{\Psi}(\underline{r}, t) = \frac{1}{4\pi} \int\int\int_V \frac{\underline{\omega}}{|\underline{r}|} dV' \tag{A.9}$$

The velocity induced by vorticity can be obtained by taking the curl of the above equation:

$$\underline{\nabla} \times \underline{\Psi}(\underline{r}, t) = \underline{\nabla} \times \frac{1}{4\pi} \int\int\int_V \frac{\underline{\omega}}{|\underline{r}|} dV' \tag{A.10}$$

Similarly, the gradient of the velocity term used for the vorticity stretching in the vorticity evolution equation is determined by taking the gradient of the above relationship:

$$\underline{\nabla} \left(\underline{\nabla} \times \underline{\Psi}(\underline{r}, t) \right) = \underline{\nabla} \left(\underline{\nabla} \times \frac{1}{4\pi} \int\int\int_V \frac{\underline{\omega}}{|\underline{r}|} dV' \right) \tag{A.11}$$

Appendix B

The Lagrangian Drift

In this chapter it is explained what is the lagrangian drift effect in inviscid flows. In his note (see Bibl. [73]) Darwin (1953) showed the following case. A non-lifting body of arbitrary shape moves at uniform speed in an unbounded, inviscid, incompressible fluid. Initially, the body is infinitely far upstream of an infinite plane of marked fluid, then, the body moves through and distorts the plane and, finally, the body is infinitely far downstream of the marked plane. Darwin suggested that the volume between the initial and final positions of the surface of marked fluid, the lagrangian drift volume, which shall be named as D_V, is equal to the "volume of fluid associated with the added-mass of the body".

Eames, Belcher and Hunt (1994) (see Bibl. [74]) re-examined Darwin's work and extended it introducing the concept of partial drift volume, which shall be named as D_P. It is the same as Darwin's D_V but it considers that x_{t0}, the initial separation between the center of the moving sphere and the plane of marked particles, is no more infinite but finite and this makes $D_P < D_V$, thus it was used the adjective "partial". Eames et al. substituted Darwin's arbitrary body with a sphere and introduced a second new lengthscale, R_{max},

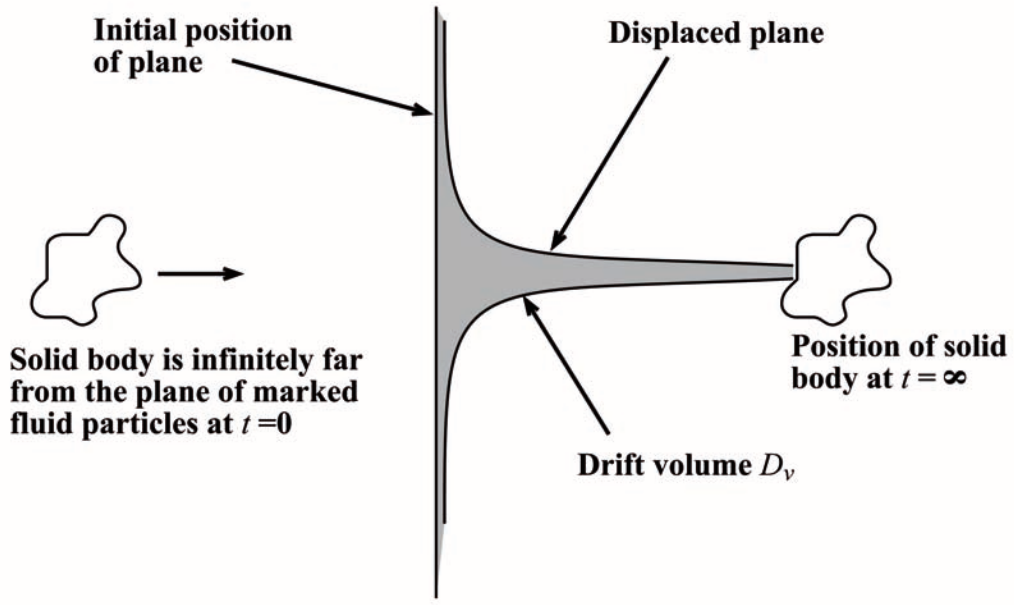

Figure B.1: A sketch of Darwin's drift volume.

the radius of a circular plane of marked particles. The starting y coordinate of a particle belonging to the marked plane is named y_{t0}. Depending on its initial position, the Lagrangian displacement of a fluid element can be either positive, a Lagrangian drift, or negative, a Lagrangian reflux, the displacement coordinates are named X and Y. Eames et al. have also found that it exists only a positive horizontal Lagrangian displacement in the case of infinite x_{t0}, this justifies the relationship $D_P < D_V$.

Similar results can be obtained if the sphere is substituted with a circle and the flow is supposed 2D. Showing again all the results similar to these in [74] in the case of a 2D circle is out of the targets of this work, anyway it is necessary to obtain the final position of a marked fluid particle in order to compare it to the result of the numerical trajectory computation done in chapter four.

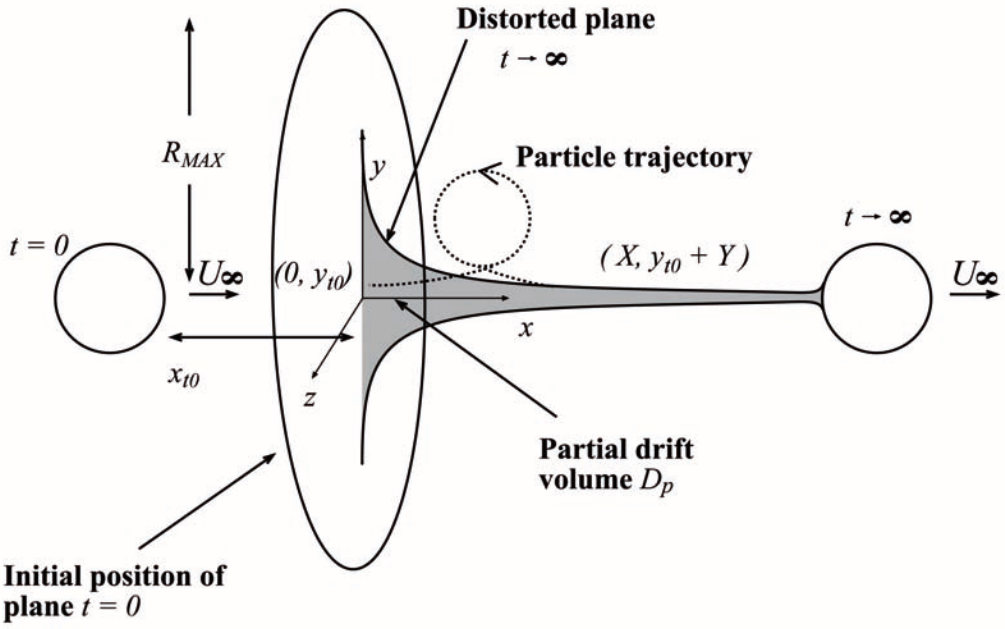

Figure B.2: A sketch of partial drift volume.

B.1 Existence of the lagrangian drift effect in inviscid flows

B.1.1 The particle at the coordinates $(0; 0)$

In this section it is analyzed the analytical flow induced by a non lifting circle, moving at uniform speed. In figure (B.3) it is shown a sketch of the flow induced by a circle moving with uniform speed. In this figure it is pointed out the circle velocity, U_∞, and its starting distance from the marked plane of particles, x_{t0}. These two data are considered assigned, together with the radius R

In order to calculate the final position of a marked fluid particle it is first necessary to observe the behavior of the particle at the coordinates $(0; 0)$ in

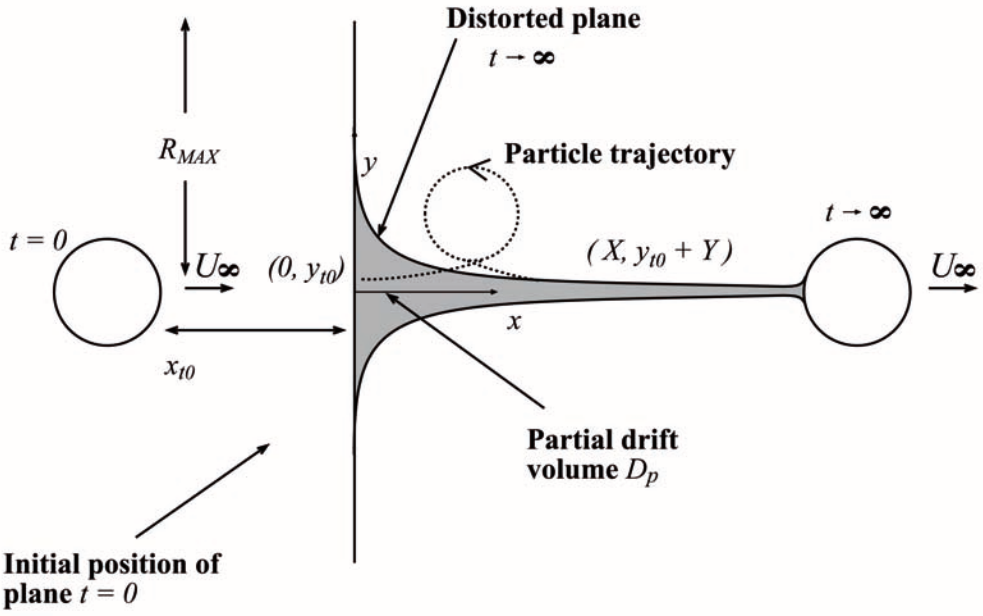

Figure B.3: A sketch of the flow induced by a non lifting circle, moving at uniform speed

figure (B.3). Observing the figures (B.1) and (B.3) it looks like this drift effect is created by particles which tend to follow the moving object, even if this is an inviscid case. To explain this it is necessary to stop the circle, which was moving from left to right, to impose to the flow a constant upstream velocity U_∞ oriented from right to left and then to consider how much time elapses when the generic particle starting at the point A of coordinates $(x_A > 1; 0)$ moves towards the point B of coordinates $(1 + \epsilon; 0)$, with ϵ approaching to zero (see figure B.4). Returning to a situation similar to that pictured in figure (B.3) it is being asked how much time elapses to reduce at ϵ the distance x_{t0} between the marked fluid particle of coordinates $(0; 0)$ and the front stagnation point of the circle. It will be shown that this time goes at infinity as ϵ approaches to zero.

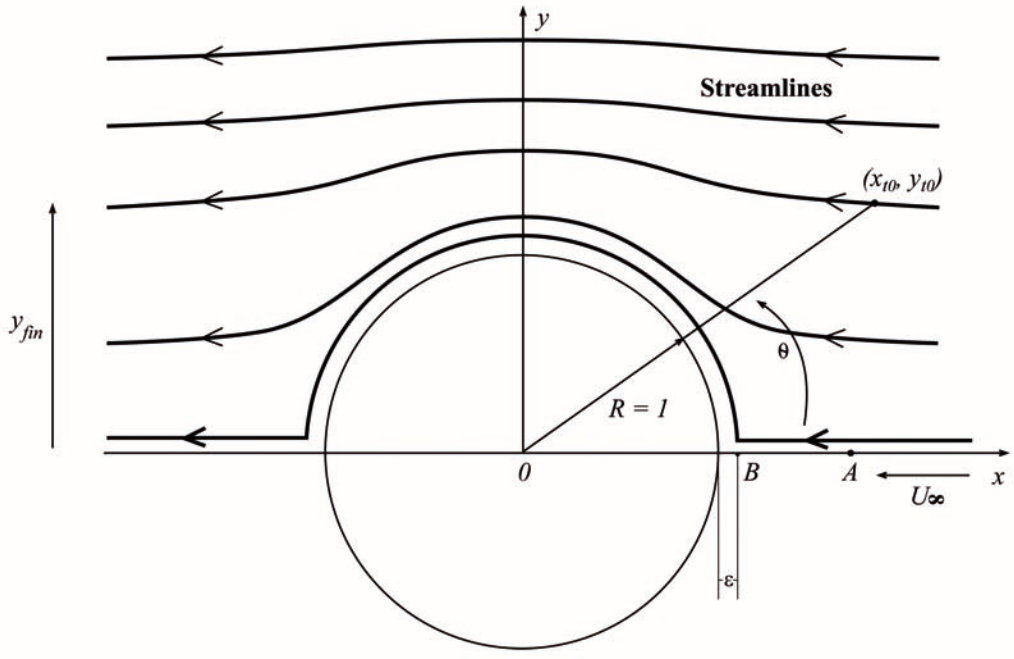

Figure B.4: Steady flow past a circle, with referencing to the symbols in §B.1.1

Returning to the situation in figure (B.4) now are done the required cal-

culations. The particle feels an induced velocity only along the x axis when moving from A towards B with the following law [1]:

$$\frac{dx}{dt} = -U_\infty \left(1 - \frac{1}{x^2}\right) = -U_\infty \left(\frac{x^2 - 1}{x^2}\right) \tag{B.1}$$

It is a well known analytical property that to fully invert a function, in this case the x coordinate in function of the elapsed time t, they must be biunivocal [77]. It is also well known that a necessary and sufficient condition for biunivocity is the equation (B.2), i.e. the derivative does never change its sign nor it reaches zero in any point of the interval [75]. This explains why it has been necessary to introduce the ϵ.

$$\frac{dx}{dt} > 0 \tag{B.2a}$$

$$\frac{dx}{dt} < 0 \tag{B.2b}$$

Thus equation (B.2) gives the opportunity to biunivocally express t as a function of x and vice versa and the derivatives of $t(x)$ and $x(t)$ are the inverse of each other. This also gives the freedom to shift freely the differentials into equation (B.1), giving the following result:

$$U_\infty dt = -dx - \frac{dx}{x^2 - 1} \tag{B.3}$$

The equation (B.3) can be integrated from point A to point B: in equation (B.4) t_{AB} is the elapsed time used by the particle to move from A to B, and it is evident that its boundedness is related to that of the integrals in dx. The first term in dx into this equation also is a finite quantity, only the last term is left to be analyzed.

$$U_\infty \int_A^B dt = U_\infty t_{AB} = -\int_{x_A}^{1+\epsilon} dx - \int_{x_A}^{1+\epsilon} \frac{dx}{x^2 - 1} \tag{B.4}$$

[1] The calculations here are developed assuming that the radius of the circle is unitary, however the equations shown below can be easily rearranged to include the constant R, which is the radius of the circle.

In equation (B.5) it is shown an indefinite integral, with the arbitrary constant omitted (see Bibl. [78]). This can be used to solve the last term into the equation (B.4), which yields equation (B.6). As ϵ approaches to zero the last term in (B.4) goes to infinity, as it can be seen in (B.6). Therefore, turning the attention back at the figure (B.3), the elapsed time to reduce at ϵ the distance x_{t0} between the marked fluid particle of coordinates $(x_{t0}; 0)$ and the front stagnation point of the circle goes to infinity as ϵ goes to zero.

$$\int \frac{dx}{x^2 - 1} \;=\; ln \left| \frac{1+x}{1-x} \right| \tag{B.5}$$

$$\int_{x_A}^{1+\epsilon} \frac{dx}{x^2 - 1} \;=\; ln \left| \frac{2+\epsilon}{\epsilon} \right| \;-\; ln \left| \frac{1+x}{1-x} \right| \tag{B.6}$$

B.1.2 The behavior of the particles starting in close proximity of the cylinder

Then a sort of "potential wake" behavior, using improper words, must be expected when dealing with particles, even if they are simple passive scalars in a steady 2D flow. Moreover this approaching to infinity elapsed time happens also to particles starting in close proximity of the circle.
Referring to the situation in figure (B.5), the particle is starting its motion over the front stagnation point but it is still very close to it. As limit of this situation it can be considered the particle moving along the circle at the same induced velocity which can be probed on its perimeter. It must be noted that physically at $R = 1$ there are no particles since those coordinates are occupied by physical object and since, as it has just been shown, the particles coming from far upstream are unable to pass the stagnation point.

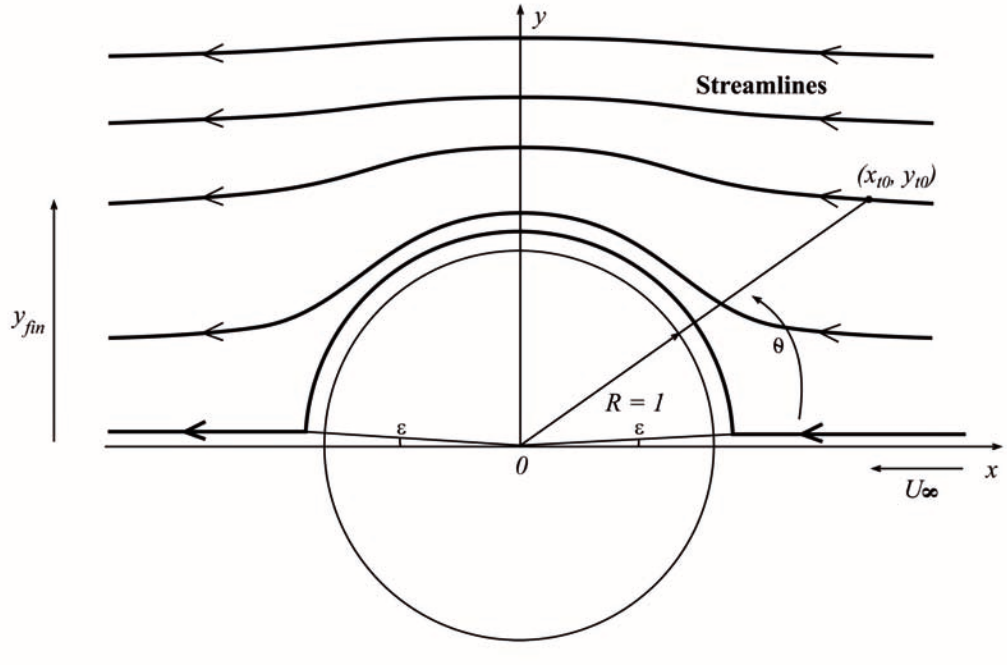

Figure B.5: Steady flow past a circle, with referencing to the symbols in §B.1.2

It is well known that the absolute value of the velocity distribution in polar coordinates upon a non-lifting 2D circle of radius R subject to a uniform velocity stream U_∞ is the following [58]:

$$|\underline{U}(R,\theta)| = 2U_\infty |sin(\theta)| \tag{B.7}$$

Then the formula (B.7) can be used to evaluate the elapsed time which a particle needs when it moves along a trajectory tending to the circle, starting from the proximity of a stagnation point and going towards the other one. Taking the upper part of this circle, noting that in this case the problem is independent from the constant R (which is unitary), it is well known that:

$$R\frac{d\theta}{dt} = 2U_\infty sin(\theta(t)) \tag{B.8}$$

Rearranging equation (B.8) yields the equation (B.9), anyway to do this operation it should be repeated the above discussion which accompanied

equation (B.2), but here it is only briefly said that an ϵ is necessary when integrating between the two stagnation points:

$$dt \;=\; \frac{R}{2U_\infty}\frac{d\theta}{sin(\theta)} \tag{B.9}$$

Integrating the equation (B.9) between the initial position angle ϵ and $\pi - \epsilon$ yields the time which the particle uses to move from a point to the other:

$$\int_0^{t_{el}} dt \;= t_{el} \;=\; \frac{R}{2U_\infty}\int_\epsilon^{\pi-\epsilon} \frac{d\theta}{sin(\theta)} \tag{B.10}$$

The following undefined integral solution (see Bibl. [78]) is useful to solve the finite integral (B.10) (the arbitrary constant is omitted):

$$\int \frac{d\theta}{sin(\theta)} \;=\; ln\left|tg\frac{\theta}{2}\right| = \; ln\,|csc(\theta) - ctg(\theta)| \tag{B.11}$$

Solving equations (B.10) using the (B.11) yields the (B.12), which goes to plus infinity when ϵ goes to zero. This means that a particle on the body starting very close to a stagnation point and going towards the other one takes a large amount of time to reach it. This also means that particles moving along particle paths passing close to the body will be greatly displaced compared to particles passing far away, as it is shown in chapter four.

$$t_{el} \;=\; \frac{R}{2U_\infty} ln \frac{|csc(\pi-\epsilon) - ctg(\pi-\epsilon)|}{|csc(\epsilon) - ctg(\epsilon)|} \tag{B.12}$$

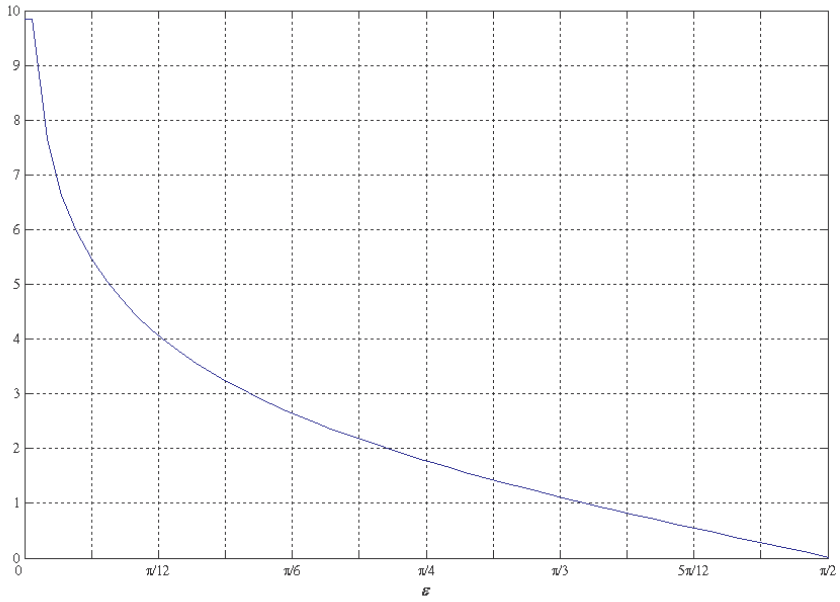

Figure B.6: Plot of function (B.12), with $R = 1m$ and $U_\infty = 0.5m/s$

B.2 Final displacement of particles

To calculate the final displacement of the particles when the body moves towards a marked plane of particles, as shown in figure (B.3), it is easier to stop the body as shown in figure (B.7). The symbols adopted in this paragraph are the same of Bibl. [74] except y_{fin} which is used instead of ρ_0, and R which is used again to denote the circle radius instead of a. Then as reference figures can be taken (B.3) and (B.7).

When time t goes towards infinity the final position of each point is $(-\infty; y_{fin})$, except the ones starting from $(x_0 > R; y_0 = 0)$ as shown in the above paragraph. Below are recalled the potential and streamline functions valid for a 2D circle, and deriving them properly it is possible to obtain the

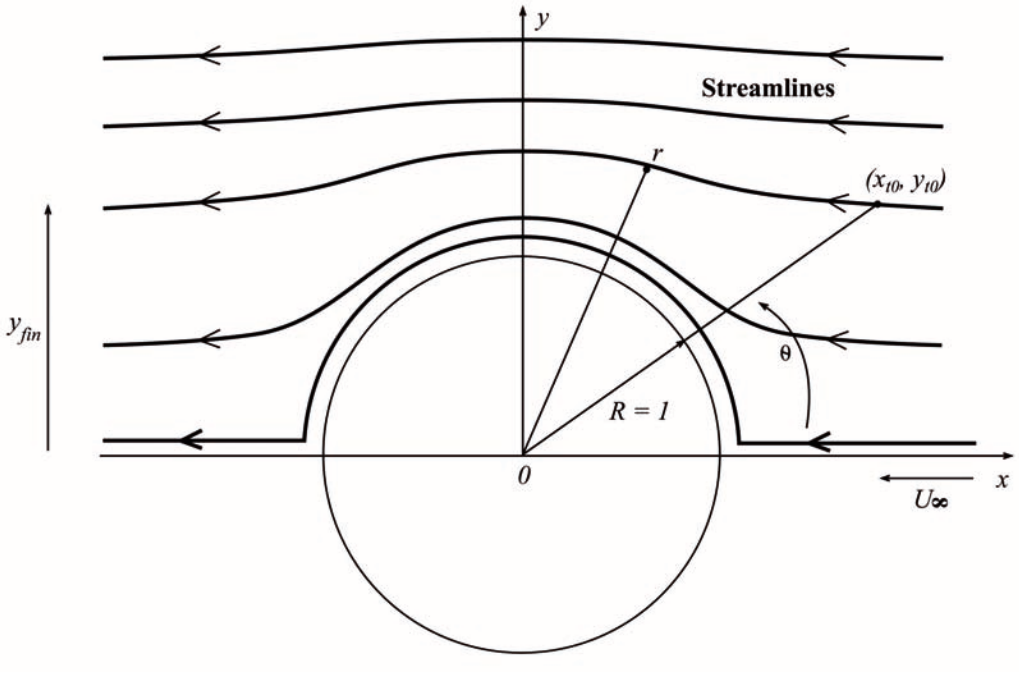

Figure B.7: Steady flow past a circle, with referencing to the symbols in §B.2

equations (B.14)

$$\phi = -U_\infty \left(r + \frac{R^2}{r} \right) cos\theta \tag{B.13a}$$

$$\psi = -U_\infty \left(r - \frac{R^2}{r} \right) sin\theta \tag{B.13b}$$

$$\frac{dr}{dt} = -U_\infty \left(1 - \frac{R^2}{r^2} \right) cos\theta \tag{B.14a}$$

$$\frac{d\theta}{dt} = U_\infty \frac{sin\theta}{r^3} \left(r^2 + R^2 \right) \tag{B.14b}$$

Using the equation (B.13b), i.e. exploiting the fact that in this case the particle traces its path line over the streamline, it is possible to create the equation (B.15), which binds the actual particle position to its final y

coordinate y_{fin}.

$$y_{fin} \;=\; y\left(1-\frac{R^2}{r^2}\right) \tag{B.15}$$

Reworking the equation (B.15) yields the equation (B.16), which resolved in r gives the equation (B.17) from which is ignored the solution which subtracts the square root term since it would mean a $r<0$, which is not acceptable.

$$r^2-\frac{y_{fin}}{sin\theta}r-R^2 \;=\; 0 \tag{B.16}$$

$$r \;=\; \frac{y_{fin}}{2sin\theta}+\sqrt{\frac{y_{fin}^2}{4sin^2\theta}+R^2} \tag{B.17}$$

The formula of Lagrangian drift of the particle X is obtainable integrating the following integral in the time, remembering that, returning to the moving circle case, the velocity of the particles is the integrand in (B.18).

$$X \;=\; \int_0^\infty (U_\infty+\phi_x)dt \;=\int_0^\infty U_\infty\left[1-\left(1-\frac{R^2}{r^2}cos(2\theta)\right)\right]dt \Rightarrow \tag{B.18}$$

$$\Rightarrow X \;=\; \int_0^\infty U_\infty\frac{R^2\left(cos^2\theta-sin^2\theta\right)}{r^2} \tag{B.19}$$

Using the equation (B.14b) in order to change the integration variable from dt to $d\theta$ and using the equation (B.16) in order to make disappear the term in r^2, it is possible to reshape the equation (B.19) into the equation (B.20). It has to be noted that in this last equation the variable r is actually a function of θ. It has also to be noted that due to the symmetry of the problem it is possible to use the (B.20) with particles starting at $(x_{t0}, y_{t0}<0)$, provided the use of absolute values of the variables θ and y_{fin}.

$$X \;=\; \int_{\theta_0}^{\pi}\frac{R^2(1-2sin^2\theta)r}{R^2sin\theta+ry_{fin}}d\theta \tag{B.20}$$

$$D_p = \int_{-\infty}^{\infty} X\,dy \tag{B.21}$$

The equation (B.20) has been used to calculate the final position of a marked plane of fluid discretized into a finite number of points. Then known these final positions obtained via a numerical integration it has been done the numerical integration of the (B.21), in order to witness the fact that if a body of arbitrary shape moving from far upstream passes a marked plane of fluid when it has arrived far downstream the drift volume is equal to the volume corresponding to the added mass of the body, in this case it is the area of a unitary radius circle [79]. In chapter four it is shown that some particles have a negative displacement when x_{t0} is not infinite, however this negative displacement reduces as when x_{t0} grows up. Since the integration (B.21) accounts for the sign these particles give a negative contribution to the drift volume. This is the reason which led Eames et al. to look for the causes of this partial drift. However since here the interest is only towards the drift volume and the final positions, then it is not written more about this. The interested reader can see Bibl. [73].

Thus in figure (B.8) are reported the trends of the Lagrangian drift areas subtended by a variable number of particles. Those particles are initially placed on the y axis, and they span between $y = -12m$ and $y = 12m$, equally distributed. Each curve has been built varying the starting distance of the circle, labeled into the legend. In abscissa are reported the used number of particles, while in ordinate it is reported the drift area in m^2. In figure (B.8) it is possible to witness that the drift area approaches to $3.14m^2$ when the starting position tends to infinity. This is due to the fact that when the starting position tends to infinity there are no more particles with negative displacements, or also the greater is the starting distance between the circle

and the particles the lesser shall be the negative displacement.

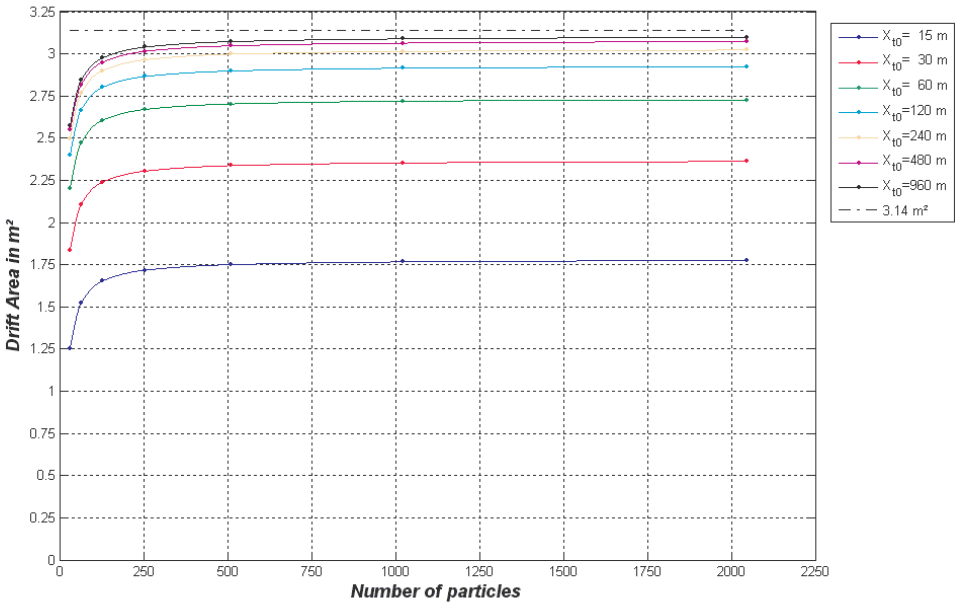

Figure B.8: Trends of the Lagrangian drift areas

Bibliography

[1] Abbott I.H., Von Doenhoff A.E.:
"Theory of wing sections"
Dover, 1959.

[2] Aksman M.J., Novikov E.A., Orszag S.A.:
"Vorton method in three-dimensional hydrodynamics"
Massachusetts Institute of Technology, 1984.

[3] Alkemade F., Nieuwstadt F.T.M., Van Groesen E.:
"The vorton method"
Delft University of Technology and University of Twente, 1993.

[4] Alonso J.J., Sheffer S.G., Martinelli L., Jameson A.:
"Parallel unsteady simulation of the flow through a helicopter rotor in hover including aeroelastic effects"
Princeton University, 1996.

[5] Anderson, J.D.Jr.:
"Fundamentals of Aerodynamics"
McGraw-Hill Book Company, 1982.

[6] Anderson, J.D.Jr.:
"Introduction to Flight"
McGraw-Hill Book Company, Sixth edition ,2008.

[7] Roskam, J:
"Airplane Design: Preliminary Sizing of Airplanes"
DARcorporation, Third edition, 2003.

[8] Ashby D.L.:
"Potential Flow Theory and Operation Guide for the Panel Code PMARC 14"
NASA/TM, 1999.

[9] Ashby D.L., Dudley M., Iguchi S.K.:
"Development and Validation of an Advanced Low-Order Panel Method"
NASA, 1988.

[10] Ashby D.L., Dudley M.R., Iguchi S.K., Browne L., Katz J.:
"Potential Flow Theory and Operation Guide for the Panel Code PMARC"
NASA, 1991.

[11] Ashley H., Landahl M.:
"Aerodynamics of wings and bodies"
Addison-Wesley Publishing Company, Inc., 1958.

[12] Beale J.T., Majda A.:
"Vortex methods I: convergence in three dimensions"
Math. Comput. 29(159) 1-27, 1982.

[13] Browne L.E., Ashby D.L.:
"Study of the Integration of Wind Tunnel and Computational Methods for Aerodynamic Configurations"
NASA, 1989.

[14] Caccavale P.:
"Un moderno metodo a potenziale per analisi fluidodinamiche"
DIAS, University of Naples "Federico II", 2006.

[15] Caccavale P., de Nicola C.:
"A new panel method for unsteady flows"
DIAS, University of Naples "Federico II", 2007.

[16] Calcagno G., Salvatore F., Greco L., Moroso A., Eriksson H.:
"An Experimental Investigation and a Theoretical and Computational Methodology to Study an Innovative Technology for Marine Current Exploitation: the Kobold Turbine"
Bollettino della Comunitá Scientifica in Australasia, 2006.

[17] Caradonna F.X., Tung C.:
"Experimental and analytical studies of a model helicopter rotor in hover"
NASA Technical Memorandum 81232, 1981.

[18] Cebeci T., RShao J., Kafyeke F., Laurendeau E.:
"Computational Fluid Dynamics for Engineers"
Springer, 2005.

[19] Charles C.:
"Numerical Computation of Internal and External Flows"
Butterworth-Heinemann, second edition, 2007.

[20] Chatelain P., Curioni A., Bergdorf M., Rossinelli D., Andreoni W., Koumoutsakos P.:
"Billion vortex particle direct numerical simulations of aircraft wakes"
Comput. Methods Appl. Mech. Engrg. 197 12961304, 2008.

[21] Chatelain P., Leonard A.:
"Face-centered cubic lattices and particle redistribution in vortex methods"
California Institute of Technology, 2002.

[22] Chorin A., Marsden J.E.:
"A mathematical introduction to fluid mechanics"
Springer-Verlag Publishing Company, Inc, 2000.

[23] Cottet G-H., Koumoutsakos P.D.:
"Vortex Methods: Theory and Practice"
Cambridge University Press, 2000.

[24] Cuzol A., Mémin E.:
"Vortex and source particles for fluid motion estimation"
IRISA, Universit de Rennes, 2003.

[25] de Nicola C.:
"Aerodinamica degli aeromobili"
DIAS, University of Naples "Federico II", Italy, 2005.

[26] Deriaz E., Perrier V.:
"Orthogonal Helmholtz decomposition in arbitrary dimension using divergence-free and curl-free wavelets"
Polish Academy of Sciences and Université de Grenoble, 2008.

[27] Doerffer P., Szulc O.:
"Numerical simulation of model helicopter rotor in hover"
Institute of Fluid-Flow Machinery PAS, 2008.

[28] Eldredge J.D.:
"Efficient tools for the simulation of flapping wing flows"
University of California, 2005.

[29] Gui Y.F. and Dou W.B.:
"A rigorous and completed statement on Helmholtz theorem"
Southeast University, 2007.

[30] Hess J.L.:
"Panel methods in computational fluid dynamics"
Annu. Rev, Fluid Mech, 1990.

[31] Hess J.L., Smith A.M.O:

"Calculation of potential flow about arbitrary bodies"

Progress in Aeronautical Sciences, Vol. 8, pp 1-138 1967.

[32] Hoffmann K.A. and Chiang S.T.:

"Computational fluid dynamics - Volume I"

Engineering, 2000.

[33] Johnson F.T., Tinico E.N., Jong Yu N.:

"Thirty years of development and application of CFD at Boeing Commercial Airplains, Seattle"

Boeing Commercial Airplanes, Seattle, 2003.

[34] Katz J., Plotkin A.:

"Low-speed Aerodynamics from wing theory to panel methods"

McGraw-Hill, 1991.

[35] Lebental S.:

"Optimization of the aerodynamics of small-scale flapping aircraft in hover"

Duke University, 2008.

[36] Liu P., B. Eng.B., Eng.M., Eng.P.:

"A time-domain panel method for oscillating propulsors with both chordwise and spanwise flexibility"

Memorial University of Newfoundland, 1997.

[37] McCroskey W.J.:

"The phenomenon of dynamic stall"

NASA Technical Memorandum 81264, 1981.

[38] McCroskey W.J. et al.:

"An experimental study of dynamic stall on advanced airfoil sections"

NASA Technical Memorandum 84245, 1982.

[39] McDonald K.T.:

"The Helmholtz Decomposition and the Coulomb Gauge"

Princeton University, 2008.

[40] Marzouk:

"Vorticity structure and evolution in a transverse jet with new algorithms for scalable particle simulation"

Massachusetts Institute of Technology, 2004.

[41] Maskew B.:

"Program VSAERO Theory Document"

NASA Contractor Report 4023, 1987.

[42] Milne-Thomson L.M.:

"Theoretical Aerodynamics"

Dover Publications, Inc., fourth edition, 1962.

[43] Milne-Thomson L.M.:

"Theoretical Hydrodynamics"

London MacMillan and CO LTD, fourth edition, 1962.

[44] Morgenthal G.:

"Comparison of numerical methods for bridge-deck aerodynamics"

University of Cambridge, 2000.

[45] Morino L., Lou C.C.:

"Subsonic potential aerodynamics for complex configurations. A general theory"

AIAA J., 12:191-97.

[46] Newman J.N.:

"Distributions of sources and normal dipoles over a quadrilateral panel"

Massachusetts Institute of Technology, 1985.

[47] Oler J.W., Strickland J.H., Im B.J., Graham G.H.:
"Dynamic Stall Regulation of the Darrieus Turbine"
Texas Tech University, 1983.

[48] Opoku D.G., Triantos D.G., Nitzsche F., Voutsinas S.G.:
"Rotorcraft aerodynamic and aeroacoustic modeling using vortex particle methods"
Carleton University, National Technical University of Athens, 2002.

[49] Park S.I., Kim M.J.:
"Vortex Fluid for Gaseous Phenomena"
Carnegie Mellon University, Ewha Womans University, 2005.

[50] Pozzi A.:
"Lezioni di Gasdinamica"
DIAS, University of Naples "Federico II", a.a. 2002-2003.

[51] Ramsey W., Milgram J.:
"Computation method for forces on aircraft in close proximity"
Massachusetts Institute of Technology, 1997.

[52] Rosenhead L.:
"The formation of vorticies from a surface of discontinuity"
Proc. Roy. Soc. London Ser. A 134, 170-192, 1931.

[53] Spalart P.R.:
"Vortex methods for separated flows"
NASA Technical Memorandum 100068, 1988.

[54] Stock M.J.:
"Summary of Vortex Methods Literature (A living document rife with opinion)"
2007.

[55] Strickland J.H., Baty R.S.:

"A three-dimensional fast solver for arbitrary vorton distributions"

Sandia National Laboratories, 1994.

[56] Strickland J.H., Homicz G.F., Porter V.L., Gossler A.A.:

"A 3-D vortex code for parachute flow predictions: VIPAR version 1.0"

Sandia National Laboratories, 2002.

[57] Tabak E.G.:

"Vortex stretching in incompressible and compressible fluids"

Spring, 2002.

[58] Tognaccini R.:

"Lezioni di Aerodinamica"

DIAS, University of Naples "Federico II", a.a. 2009-2010.

[59] Voutsinas S.G., Belesais M.A., Rados K.G.:

"Investigation of the Yawed Operation of Wind Turbines by means of a Vortex Particle Method"

National Technical University of Athens, 1994.

[60] Willis D.J.:

"An unsteady, accelerated, high order panel method with vortex particle wakes"

Massachusetts Institute of Technology, 2006.

[61] Willis D.J., Paraire J., White J.K.:

"A combined pfft-multipole tree code, unsteady panel method with vortex particle wakes"

Massachusetts Institute of Technology, 2006.

[62] Winckelmans G.S., Leonard A.:

"Contributions to vortex particle methods for the computation of three-dimensional incompressible unsteady flows"

California Institute of Technology, 1993.

[63] Anderson John D. Jr:

"Ludwig Prandtl's Boundary Layer"

AIP, Physics Today, December 2005.

[64] Nola N.:

"A vorton wake model for panel methods"

DIAS, University of Naples "Federico II", 2009.

[65] Carlomagno G.M.:

"Fluidodinamica"

Liguori Editore, first edition, 2001.

[66] Monti R., Savino R.:

"Aerodinamica, parte I"

Liguori Editore, second edition, 2001.

[67] Monti R., Savino R.:

"Aerodinamica, parte II"

Liguori Editore, second edition, 2001.

[68] Blazek J.:

"Computational Fluid Dynamics: Principles and Applications"

Elsevier, first edition, 2001.

[69] Meola C., De Felice G.:

"Fondamenti lineari per la fluidodinamica numerica"

Edizioni L'Ateneo s.a.s. Napoli, first edition, 1996.

[70] Quarteroni A., Sacco R., Saleri F.:

"Numerical Mathematics"

Springer, 2000.

[71] Darmofal D. L., Haimes R.:
"An Analysis of 3D Particle Path Integration Algorithms"
Journal of Computational Physics, vol. 123 (1996).

[72] Strikwerda J. C.:
"Finite difference schemes and partial differential equations"
Society for Industrial and Applied Mathematics, 2004.

[73] Darwin C.:
"Note on hydrodynamics"
Mathematical Proceedings of the Cambridge Philosophical Society, vol. 49 (1953).

[74] Eames I., Belcher S.E., Hunt J.C.R.:
"Drift, partial drift and Darwins proposition"
Cambridge University Press, Journal of Fluid Mechanics, vol. 275 (1994).

[75] Biscari P., Ruggeri T., Saccomandi G., Vianello M. :
"Meccanica Razionale per lingegneria"
Monduzzi Editore, second edition, 2007.

[76] Lamberti L., Mereu L., Nanni A. :
"Corso di Matematica 1"
ETAS Libri, second edition, 1998.

[77] Lamberti L., Mereu L., Nanni A. :
"Corso di Matematica 2"
ETAS Libri, second edition, 1998.

[78] Lamberti L., Mereu L., Nanni A. :
"Corso di Matematica 3"
ETAS Libri, second edition, 1998.

[79] Brennen C.E.:

"A rewiew of added mass and fluid inertial forces"

Naval civil engineering laboratory, Port Hueneme, California, January 1982.

[80] Theodorsen T.:

"General theory of aerodynamic instability and the mechanism of flutter"

NACA report 496, 1934.

[81] Garrick I. E.:

"Propulsion of a flapping and oscillating airfoil"

NACA report 567, 1936

[82] Yang S., Luo S., Liu F., Tsai H.:

"Optimization of Unstalled Pitching and Plunging Motion of an Airfoil"

AIAA 2006-1055.

[83] McCroskey W.J.:

"The phenomenon of dynamic stall"

NASA Technical Memorandum 81264, 1981.

[84] McCroskey W.J. et al.:

"An experimental study of dynamic stall on advanced airfoil sections"

NASA Technical Memorandum 84245, 1982.

[85] Piziali R.A.:

"2-D and 3-D oscillating wing aerodynamics for a range of angles of attack including stall"

NASA Technical Memorandum 4632, 1994.

[86] Srinivasan G.R., Ekaterinaris J.A., McCroskey W.J.:

"Evaluation of turbulence models for unsteady flows of an oscillating airfoil"

NASA Technical Memorandum 111942, 1994.

[87] Chandrasekaran B.:

"Method for the Prediction of the Installation Aerodynamics of a Propfan at Subsonic Speeds"

NASA Contractor Report 3887, Vigyan Research Associates Inc., Hampton, Virginia, April 1985.

[88] Bartlett G.:

"An Experimental Investigation of Propfan Installation on an Unswept Supercritical Wing"

Masters Thesis, George Washington University, August 1983.

[89] Bartlett D. W. and Patterson, J. C. Jr.:

"NASA Supercritical-Wing Technology"

NASA Langley Research Center, Hampton, Virginia, July 1978.

[90] Harris C. D.:

"Aerodynamic characteristics of the 10-percent-thick NASA supercritical airfoil 33 designed for a normal-force coefficient of 0.7"

NASA Langley Research Center, Hampton, Virginia, January 1975.

[91] Harris C. D.:

"Aerodynamic Characteristics of a 14-Percent-Thick NASA Supercritical Airfoil Designed for a Normal-Force Coefficient of 0.7"

NASA Langley Research Center, Hampton, Virginia, July 1975.

[92] Massa F.:

"Modello d'elica per campi a potenziale ed interazione elica-velivolo"

DIAS, University of Naples "Federico II", 2006.

[93] Losito V.:

"Calcolo dei Campi di Velocit Indotte da Eliche e delle Interazioni Eliche-Velivolo in Regime Comprimibile Subcritico"

Aeronautical Academy of Pozzuoli.

[94] Losito V.:

"Elica SR2"

Aeronautical Academy of Pozzuoli.

[95] Conway J. T., Su J.:

"PMAL Flow Calculations for the Aurora Aircraft Using Non-axisymmetric Propeller Actuator Disks"

Journal of Canadian Aeronautics and Space Institute, vol. 49, No. 1, March 2003.

Ringraziamenti

Sento il dovere di ringraziare tutti coloro che mi hanno aiutato a raggiungere questo traguardo nel percorso di studi universitari.

Ringrazio la mia famiglia, senza il suo sostegno materiale e affettivo non so se sarei stato capace di laurearmi. Soprattutto la ringrazio per la pazienza con cui ha sopportato il mio carattere, che in talune occasioni diventa veramente poco accomodante. Desidero ringraziare anche Michele Grazioso che ha contribuito in tal senso come gli altri miei familiari, e che ormai considero come un fratello acquisito.

Ringrazio gli amici, con i quali ho condiviso sia un percorso di studi, che un percorso di vita, con la speranza che la distanza fisica che mi separa da alcuni di loro non recida questo legame.

Grazie a tutti,

Pasquale